

**Spin Valve Effect In Monolayer Transition-Metal Dichalcogenides**

BY

BO HSU

B.Sc., Feng Chia University, 2009

THESIS

Submitted as partial fulfillment of the requirements  
for the degree of Doctor of Philosophy in Electrical and Computer Engineering  
in the Graduate College of the  
University of Illinois at Chicago, 2018

Chicago, Illinois

Defense Committee:

Zheng Yang, Chair and Advisor

Mitra Dutta

Michael Strosio

Vitali Metlushko

Vikas Berry, Chemical Engineering

*This dissertation is dedicated to my loving parents, Chi-Hsin Hsu and I-Chun Wang.*

## ACKNOWLEDGEMENTS

I would like to express my gratitude to my advisor, Zheng Yang, for his guidance and patience throughout my research. His vast knowledge on materials research has taught me valuable lessons on various research methodology. This dissertation would not have been possible without his assistance and guidance. He will always have my appreciation for investing of countless valuable hours in me. Thank you!

I would like to thank my committee members Prof. Vikas Berry, Prof. Mitra Dutta, Prof. Vitali Metlushko, and Prof. Michael Stroscio for their guidance and suggestions.

I would like to also thank various undergraduate students who volunteer to conduct research in our laboratory. Their collective efforts have saved me hundreds of hours of time.

Lastly, I would like to thank my parents for their full support during my pursuit of Ph.D. degree. I have finally achieved something that meets their standards!

BH

## TABLE OF CONTENTS

<b>CHAPTER</b>	<b>PAGE</b>
<b>1. INTRODUCTION .....</b>	<b>1</b>
1.1 Spintronics.....	1
1.1.1 Spintronics Overview .....	1
1.1.2 Magnetism .....	2
1.1.3 Giant Magnetoresistance and Tunneling Magnetoresistance.....	6
1.1.4 Spin Valve .....	12
1.1.5 Spin Valve Review .....	14
1.2 Two-Dimensional Materials .....	23
1.2.1 Graphene .....	23
1.2.2 Transition-Metal Dichalcogenides .....	24
1.2.3 Two-Dimensional Materials Spin Valves Review .....	28
<b>2 GROWTH OF MONOLAYER TRANSITION-METAL DICHALCOGENIDES.....</b>	<b>36</b>
2.1 Introduction to MX <sub>2</sub> (M = Mo, W; X = S, Se) Growth .....	36
2.2 Growth Setup .....	40
2.3 Growth Method .....	41
2.4 Optimization of MX <sub>2</sub> Growth Parameters .....	46
2.5 Effect of Vapor Pressure.....	62
2.5.1 Experiment .....	67
2.5.2 Results and Discussion .....	69
2.6 Summary .....	73
<b>3 CHARACTERIZATION OF TRANSITION-METAL DICHALCOGENIDES.....</b>	<b>76</b>
3.1 Imaging of MX <sub>2</sub> .....	76
3.1.1 Optical Microscopy of MX <sub>2</sub> .....	76
3.1.2 Scanning Electron Microscopy of MX <sub>2</sub> .....	77
3.1.3 Atomic Force Microscopy of MX <sub>2</sub> .....	79
3.2 Optical Characterization of MX <sub>2</sub> .....	80
3.2.1 Raman Spectroscopy of MX <sub>2</sub> .....	80
3.2.2 Photoluminescence of MX <sub>2</sub> .....	87
3.3 Electrical Characterization of MX <sub>2</sub> .....	94

## TABLE OF CONTENTS (continued)

<b><u>CHAPTER</u></b>	<b><u>PAGE</u></b>
3.3.1 Experiments.....	95
3.3.2 Contact Resistance .....	99
3.3.3 MX <sub>2</sub> Field Effect Transistors.....	103
3.3.4 Hall Effect of Monolayer MX <sub>2</sub> .....	107
3.4 Summary .....	112
<b>4 SPIN VALVES BASED ON TRANSITION-METAL DICHALCOGENIDES.....</b>	<b>113</b>
4.1 Introduction.....	113
4.2 Experiment.....	114
4.3 Results and Discussion.....	119
4.3.1 Characterization.....	119
4.3.2 TMR of Monolayer MX <sub>2</sub> Spin Valves .....	121
4.3.3 Annealing Effect in MX <sub>2</sub> Spin Valves .....	137
4.3.4 Layer Dependent TMR of MX <sub>2</sub> Spin Valves.....	141
4.3.5 Antiferromagnetic Layer Pinned MX <sub>2</sub> Spin Valves.....	144
4.3.6 Anisotropy of MX <sub>2</sub> Spin Valves.....	148
4.3.7 Life-Time of MX <sub>2</sub> Spin Valves.....	151
4.4 Summary .....	153
<b>5 FLEXIBLE SPIN VALVE BASED ON MONOLAYER TRANSITION-METAL DICHALCOGENIDES.....</b>	<b>154</b>
5.1 Introduction.....	154
5.2 Experiment.....	156
5.3 Results and Discussion.....	161
5.4 Summary and Perspective.....	169
<b>6 CONCLUSIONS.....</b>	<b>171</b>
<b>7 CITED LITERATURE.....</b>	<b>174</b>
<b>8 VITA.....</b>	<b>195</b>

## LIST OF TABLES

<u>TABLE</u>		<u>PAGE</u>
I.	TOP-DOWN SYNTHESIS METHOD FOR MONOLAYER $\text{MX}_2$ .....	38
II.	HALL MOBILITY AND CARRIER CONCENTRATION IN MONOLAYER $\text{MOS}_2$ AND $\text{WSe}_2$ .....	111
III.	LIST OF MEASURED MONOLAYER TMDC SPIN VALVES.....	126
IV.	LIST OF ANNEALED TMDC SPIN VALVES.....	140
V.	LIST OF MUTLI-LAYERED TMDC SPIN VALVES.....	144
VI.	BIAS DEPENDENT MEASUREMENT OF TMDC SPIN VALVES.....	148

## LIST OF FIGURES

<u>FIGURE</u>	<u>PAGE</u>
1.1. Ordering of spins in paramagnetic, ferromagnetic, antiferromagnetic, and ferrimagnetic materials.....	4
1.2. Hysteresis loop of ferromagnetic materials.....	5
1.3. Density of states vs energy for 3d and 4s band for paramagnetic and ferromagnetic metals.....	8
1.4. Two-current model for spin up and spin down electrons.....	8
1.5. Density of states of spin-up ( $\uparrow$ ) electrons and spin-down ( $\downarrow$ ) electrons in magnetic layers.....	11
1.6. Operation of spin valve.....	14
1.7. Operation of antiferromagnetic-pinned spin valve.....	18
1.8. Development of MTJ from 1995 to 2008 for MgO and Al-O junctions.....	22
1.9. Crystal structure of MoS <sub>2</sub> .....	26
1.10. Development of 2D material spin valve.....	35
2.1. Digital camera image for home-built CVD growth system for MX <sub>2</sub> growth.....	40
2.2. Synthesis of monolayer MoS <sub>2</sub> and MoSe <sub>2</sub> .....	44
2.3. Synthesis of monolayer WS <sub>2</sub> and WSe <sub>2</sub> .....	46
2.4. Sulfurization of WO <sub>3</sub> powders.....	48
2.5. Optical Images of S and Se temperature effect on growth morphology.....	51

**LIST OF FIGURES (continued)**

<b><u>FIGURE</u></b>	<b><u>PAGE</u></b>
2.6. Optical microscope of monolayer MoS <sub>2</sub> crystal grown at different S temperature.....	52
2.7. Optical Images of S and Se temperature effect on growth morphology in WS <sub>2</sub> and WSe <sub>2</sub> growths.....	53
2.8. Optical microscope of monolayer MoS <sub>2</sub> crystal grown at different substrate and MoO <sub>3</sub> source temperature.....	55
2.9. OM images of WS <sub>2</sub> grown at different temperature.....	56
2.10. OM images of WSe <sub>2</sub> grown at different temperature.....	58
2.11. OM images of MoS <sub>2</sub> monolayers grown at different flow rates.....	60
2.12. Effect of Ar:H <sub>2</sub> on WSe <sub>2</sub> growths.....	62
2.13. Schematic of MoS <sub>2</sub> growth setup for local vapor pressure study.....	69
2.14. Morphology of as-grown MoS <sub>2</sub> under various local pressure.....	71
2.15. Effect of source to substrate distance in MoS <sub>2</sub> growths.....	73
2.16. Largest single crystal MX <sub>2</sub> monolayers grown after growth optimization.....	75
3.1. Optical microscope image of CVD-grown WS <sub>2</sub> .....	77
3.2. Scanning electron microscope images of MX <sub>2</sub> .....	79
3.3. Atomic force microscopy of MoS <sub>2</sub> .....	80
3.4. Raman spectra of MoS <sub>2</sub> .....	83

**LIST OF FIGURES (continued)**

<b><u>FIGURE</u></b>	<b><u>PAGE</u></b>
3.5. Raman spectra of MoSe <sub>2</sub> .....	84
3.6. Raman spectra of WS <sub>2</sub> .....	86
3.7. Raman spectra of monolayer WSe <sub>2</sub> .....	87
3.8. Photoluminescence spectra of CVD-MoS <sub>2</sub> .....	89
3.9. Photoluminescence spectra of CVD-MoSe <sub>2</sub> .....	91
3.10. Photoluminescence spectra of CVD-WS <sub>2</sub> .....	93
3.11. Photoluminescence spectra of CVD grown WSe <sub>2</sub> .....	94
3.12. Fabrication process of MX <sub>2</sub> FET/Hall-Bar devices.....	97
3.13. Electrical measurement of MX <sub>2</sub> FET and Hall effect.....	99
3.14. Optimazation of MoS <sub>2</sub> FET fabrication.....	102
3.15. Estimation of MoS <sub>2</sub> contact resistance using transfer-length method.....	103
3.16. I <sub>ds</sub> -V <sub>ds</sub> curves of a monolayer MoS <sub>2</sub> field effect transistor at different gate voltage bias.....	105
3.16. Gating effect in MoSe <sub>2</sub> , WS <sub>2</sub> , and WSe <sub>2</sub> FETs.....	107
3.17. Hall Effect of monolayer MX <sub>2</sub> .....	110
4.1. Fabrication process for MX <sub>2</sub> spin valves.....	117

**LIST OF FIGURES (continued)**

<b><u>FIGURE</u></b>	<b><u>PAGE</u></b>
4.2. Characterizations of as-grown MoS <sub>2</sub> , WS <sub>2</sub> , MoSe <sub>2</sub> , and WSe <sub>2</sub> monolayer by chemical vapor deposition.....	121
4.3. Device Structure of the MX <sub>2</sub> spin valves.....	125
4.4. Magnetoresistance of reference devices without MX <sub>2</sub> insulating layer.....	130
4.5. Junction <i>I-V</i> characteristics for MX <sub>2</sub> spin valves.....	131
4.6. Temperature dependent magnetoresistance of MX <sub>2</sub> spin valves.....	133
4.7. Temperature dependence tunneling magnetoresistance of MX <sub>2</sub> spin valves....	135
4.8. Summary of tunneling magnetoresistance of all MX <sub>2</sub> spin valves.....	136
4.9. Annealing effect on MX <sub>2</sub> spin valves.....	139
4.10. Multilayer MX <sub>2</sub> spin valves.....	143
4.11. Exchange biased pinned WS <sub>2</sub> spin valve.....	146
4.12. Bias dependent tunneling magnetoresistance.....	147
4.13. Anisotropy of WS <sub>2</sub> spin valve.....	150
4.14. Aging effect of MX <sub>2</sub> spin valves.....	152
5.1. Fabrication of flexible MX <sub>2</sub> spin valve.....	158
5.2. Measurement of flexible MX <sub>2</sub> spin valve.....	160
5.3. Device structure of flexible MX <sub>2</sub> spin valve.....	162

**LIST OF FIGURES (continued)**

<b><u>FIGURE</u></b>	<b><u>PAGE</u></b>
5.4. Magnetoresistance of flexible MoS <sub>2</sub> spin valve at different bending radii.....	163
5.5. Magnetoresistance of monolayer MoS <sub>2</sub> flexible spin valves at different bending radius or curvature.....	165
5.6. Magnetoresistance of WS <sub>2</sub> spin valves under various bending radii.....	167
5.7. Magnetoresistance versus bend radius of WS <sub>2</sub> spin valve.....	169

## LIST OF ABBREVIATIONS

FET	Field-Effect Transistor
FM	Ferromagnetic Metal
NM	Non-Magnetic
GMR	Giant Magnetoresistance
TMR	Tunneling Magnetoresistance
MTJ	Magnetic Tunneling Junctions
MRAM	Magnetic Random-Access Memory
RAM	Random-Access Memory
TMDC	Transition-Metal Dichalcogenide
CVD	Chemical Vapor Deposition
PL	Photoluminescence
CIP	Current-In-Plane
CPP	Current-Perpendicular-to-Plane
RT	Room Temperature
LT	Low Temperature
IPA	Isopropyl Alcohol
DI	De-Ionized
OM	Optical Microscope
SEM	Scanning Electronic Microscope

## SUMMARY

Spintronics uses the spin orientation of carriers to represent “0” and “1” state, whereas electronics use charge to control low and high voltages for the states. Spin valves consist of a thin nonmagnetic layer sandwiched in between two thin ferromagnetic layers. The spin valve resistance is determined by the magnetization alignment of the two thin ferromagnetic layers, which can be controlled by an external magnetic field. Transition-metal dichalcogenides (TMDC) monolayers are novel two-dimensional (2D) semiconductors which are promising candidates for advanced devices in a variety of areas such as electronics, photonics, and spintronics due to their extraordinary properties such as 2D nature with a single molecular thickness, flexibility, direct bandgap covering from infrared to red in the spectrum, and decent mobility comparable to Si etc.

This dissertation reports the experimental work on the fabrication and characterization of spin valves with single-crystalline TMDC  $\text{MX}_2$  ( $\text{M}=\text{Mo}, \text{W}$ ,  $\text{X}=\text{S}, \text{Se}$ ; four types of materials in total) monolayers as spacer layers and Co and NiFe as top and bottom ferromagnetic layers. The single-crystalline TMDC  $\text{MX}_2$  monolayers were grown using a home-built chemical vapor deposition (CVD) system. The ferromagnetic layers were deposited using physical vapor deposition. The spin valves were fabricated using photolithography. The tunnel magnetoresistance of the fabricated spin valves were

## SUMMARY (continued)

characterized under different magnetic fields and at various temperatures.

In Chapter 1, an introduction to spintronics and 2D materials is given, in particular, the physics of spin valves, background of 2D TMDC  $\text{MX}_2$ , and an historical view of the development of classical spin valves with magnetic tunneling junctions based on MgO and Al-O spacer layers were discussed. Finally, a brief literature review section of the most recently reported spin valves with 2D materials as spacer layers was given

In Chapter 2, the growth of large-area single-crystalline monolayer  $\text{MX}_2$  (M=Mo,W, X=S,Se; four type materials in total) on  $\text{SiO}_2$ -coated Si substrates using a home-built CVD system is discussed. The growth of  $\text{MX}_2$  is optimized by tuning the growth temperature, carrier gas composition and flow rate, precursor ratios, the local vapor pressure near the substrates, and growth time. The optimization process is based on the growth of over 2000 samples. The largest monolayers  $\text{MX}_2$  achieved are  $\sim 190 \mu\text{m}$ ,  $\sim 450 \mu\text{m}$ ,  $\sim 80 \mu\text{m}$ , and  $\sim 180 \mu\text{m}$  for  $\text{MoS}_2$ ,  $\text{WS}_2$ ,  $\text{MoSe}_2$ , and  $\text{WSe}_2$  respectively.

In Chapter 3, the structural, optical, and electrical characterizations of  $\text{MX}_2$  are reported and discussed including optical microscopy, scanning electron microscopy, atomic force microscopy, Raman scattering, photoluminescence (PL) spectroscopy, field-effect transistor transport measurements, and Hall effect measurements. The distance between the

## SUMMARY (continued)

characteristic peaks in Raman spectra of  $\text{MX}_2$  is used to identify  $\text{MX}_2$  monolayers. PL spectra of  $\text{MX}_2$  confirms the high crystallinity and monolayer nature. Monolayer  $\text{MX}_2$  field effect transistors were fabricated using wet transfer approach and photolithography. Electrical characterizations show the field effect mobilities of monolayer  $\text{MX}_2$  are up to  $6.7 \pm 0.2 \text{ cm}^2\text{V}^{-1}\text{s}^{-1}$ ,  $82 \pm 18 \text{ cm}^2\text{V}^{-1}\text{s}^{-1}$ ,  $297 \pm 45 \text{ cm}^2\text{V}^{-1}\text{s}^{-1}$ ,  $12 \pm 3 \text{ cm}^2\text{V}^{-1}\text{s}^{-1}$  for  $\text{MoS}_2$ ,  $\text{WS}_2$ ,  $\text{MoSe}_2$ , and  $\text{WSe}_2$  respectively. Furthermore, Hall Effect measurements reveals  $\text{MoS}_2$  and  $\text{WSe}_2$  have mobilities up to  $118 \pm 4 \text{ cm}^2\text{V}^{-1}\text{s}^{-1}$  and  $28 \pm 2 \text{ cm}^2\text{V}^{-1}\text{s}^{-1}$  respectively.

In Chapter 4, vertical spin valves with  $\text{MX}_2$  (M=Mo,W, X=S,Se; four types of materials in total) monolayers as spacer layers and Co and NiFe as top and bottom ferromagnetic layers were fabricated on  $\text{SiO}_2$ -coated Si substrates using wet-transfer approach and photolithography. Tunneling magnetoresistance (TMR) of  $\text{MX}_2$  spin valves were measured from 15 K to room temperature. In  $\text{MoS}_2$  spin valves, TMR ratios are up to 0.60% at room temperature and up to 0.83% at 16K. The TMR ratios of  $\text{WS}_2$  spin valves are up to 0.72% at room temperature and up to 1.42% at 16K. The TMR ratios of  $\text{MoSe}_2$  spin valves are up to 0.30% at room temperature and up to 0.38% at 16K. The TMR ratios of  $\text{WSe}_2$  spin valves are up to 0.19% at room temperature and up to 0.40% at 16K. Additionally, various properties of  $\text{MX}_2$  spin valves, including annealing effect,

## SUMMARY (continued)

exchanged-bias effect, thickness dependence, magnetic anisotropy, and “aging effect” were also carefully studied systematically on a large number of devices. Hundreds of spin valve devices were fabricated for this study.

In Chapter 5, flexible spin valves with  $MS_2$  (M=Mo and W; two types of materials in total) monolayer as spacer layer and Co and NiFe as top and bottom ferromagnetic layers were fabricated on flexible polyimide substrate using wet transfer and photolithography processes. The devices show superior performance with small TMR degradation over a large range of bending of the substrate. The room-temperature TMR ratios for the first  $MoS_2$  flexible spin valve were  $0.20 \pm 0.01 \%$  without bending, and  $0.15 \pm 0.01 \%$  at 1 cm bending radius. In the second  $MoS_2$  flexible spin valve, TMR ratio of  $0.27 \pm 0.03 \%$  and  $0.14 \pm 0.01 \%$  were observed at no bending and at 1 cm bend radius, respectively. The room-temperature TMR of  $WS_2$  flexible spin valve were  $0.37 \pm 0.01 \%$  without bending and  $0.32 \pm 0.02 \%$  at 1 cm bending radius.

## CHAPTER 1

### INTRODUCTION

#### 1.1.1 Spintronics

#### 1.1.2 Spintronics Overview

Two fundamental properties are tied with electrons, they are charge and spin. In contrast to electronics which uses electronic charge to represent “0” and “1” state, spintronics revolve around the manipulation of spin direction of electrons (or other carriers) in solid state devices. In spintronics, the states are represented by electron’s spin “up” and “down”, and therefore rely heavily on their abilities to generate, detect and switch spins of electrons. The field of spintronics has gained substantial attention through recent advances in nano-technology. With the scaling-down of solid-state devices, traditional electronics such as MOSFETs suffers from short channel effects and various problems; spintronics, however benefit at sub micrometer scale when the device dimension is similar or smaller than the spin diffusion length. A common method to generate and control spin direction of electrons is to apply an external magnetic field across a ferromagnetic material. When electrons are injected from ferromagnetic electrodes, electrons retain their spin polarization for a certain amount of time and travel a certain amount of distance. Such time and distance

are called spin-relaxation time and spin diffusion length, and they are tied to fundamental properties of materials. Today, spintronic devices such as spin-field-effect-transistor (spin-FET)<sup>1</sup> and spin valves are connected to many fields of research, including magnetism, semiconductor physics, superconductivity and optics, and the materials studied ranging from traditional materials such as III-V semiconductors, organic semiconductors, and ferromagnets to novel materials including carbon nanotubes and two-dimension materials.

### **1.1.3 Magnetism**

Materials can generally be categorized into five major magnetic types, which are diamagnetism, paramagnetism, ferromagnetism, anti-ferromagnetism, and ferrimagnetism. Diamagnetic materials, such as Si and Au, have small and negative magnetic susceptibility. The magnetization direction of diamagnetic materials is opposite of the applied magnetic field. In paramagnetic materials, under the influence of an external magnetic field, electron spins can weakly align and induce a small magnetization. However, electron spins are orientated in random directions without the presence of an external magnetic field due to thermal agitation, therefore total magnetization becomes zero as shown in Figure 1.1. In ferromagnetic materials, not only they behave similarly to paramagnetic materials in the sense that they align under an external magnetic field, but

also the spins of electrons tend to align with each other to maintain a lower energy state, thus forming a magnetic domain, and retaining a net magnetization even without external magnetic field as shown in Figure 1.1. This phenomenon is called spontaneous magnetization, which is a result of net magnetic moment from partially filled electrons shells. However, when the temperature of ferromagnets are above Curie temperature, the materials lose their magnetic properties. Above the Curie temperature, the spins become randomly orientated and material becomes paramagnetic. In antiferromagnet, the spins tend to align antiparallely with zero net moment at temperatures below Néel temperature. In ferrimagnetic materials, a nearby dipoles point in opposite directions similar to antiferromagnetic materials, but the moments do not cancel out each other, and there is a finite net magnetization.

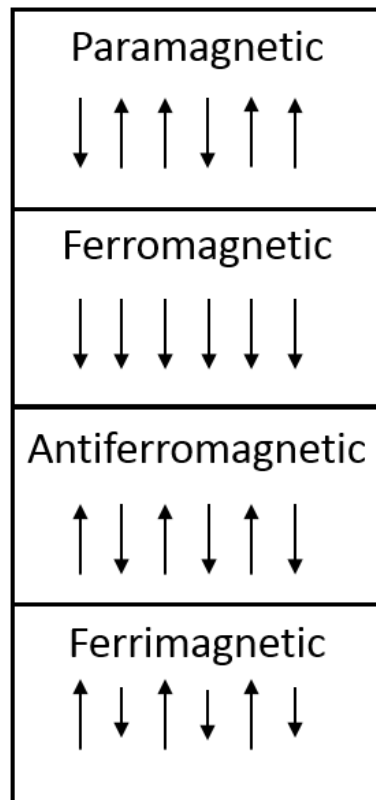


**Figure 1.1.** Ordering of spins in paramagnetic, ferromagnetic, antiferromagnetic, and ferrimagnetic materials. (Kittel, 2005)

When a ferromagnetic material is placed under an increasing magnetic field  $\mathbf{H}$ , its magnetization will gradually increase, starting from origin, until the magnetization reaches saturation. If the field,  $\mathbf{H}$ , is decreased, magnetization  $\mathbf{M}$  does not go back to the initial magnetization curve but decreases more slowly. Once  $\mathbf{H}$  has decreased to zero,  $\mathbf{M}$  is still having a non-zero value, which is called *retentivity*. When the reverse magnetic field

applied is sufficiently large,  $\mathbf{M}$  passes through zero. This reverse magnetic field required to bring the total magnetization to zero is called the *coercivity* or coercive force. With further increase of the applied reversing magnetic field,  $\mathbf{M}$  also increases with respectively in the same direction. Once  $\mathbf{M}$  reaches the saturation, a loop known as hysteresis loop is formed as shown in Figure 1.2.

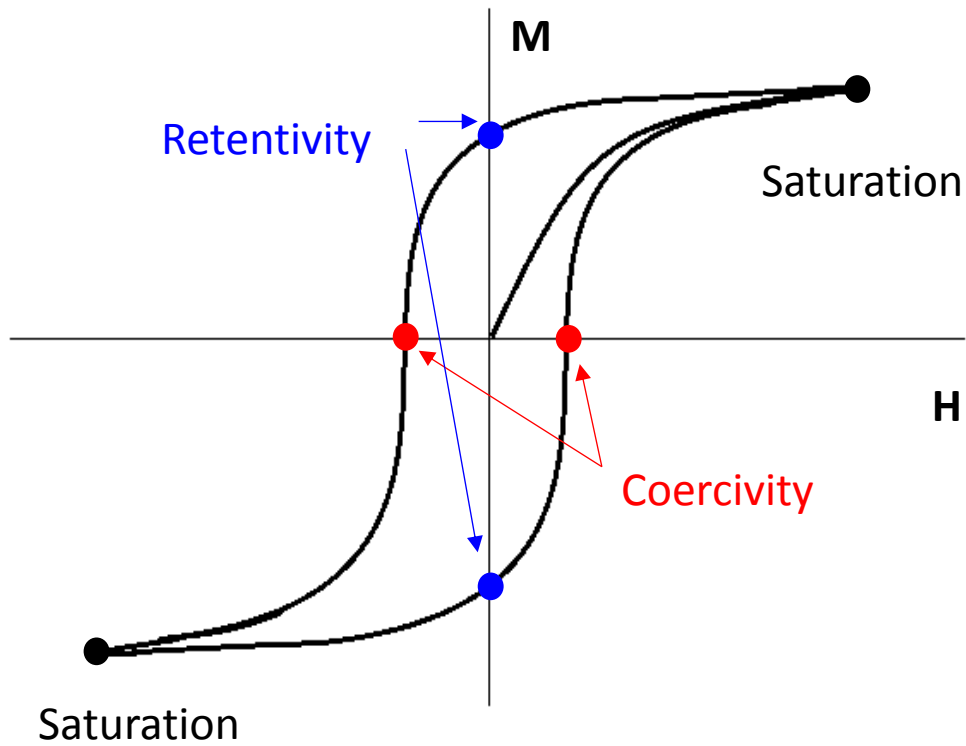


**Figure 1.2.** Hysteresis loop of ferromagnetic materials

#### **1.1.4 Giant Magnetoresistance Effect and Tunneling Magnetoresistance**

##### **Effect**

Giant magnetoresistance effect, or GMR effect, was discovered by Albert Fert<sup>3</sup> and Peter Grunberg<sup>4</sup> in late 1980s in Fe/Cr super-lattice and Fe/Cr/Fe films respectively and won the Nobel Prize together in physics in 2007<sup>5-6</sup>. When a non-ferromagnetic metal (NM) is adjacent to a ferromagnetic metal (FM), the electrical resistance across the structure has two states depending on the magnetization of the ferromagnetic metal. In ferromagnetic metals (Ni, Fe, and Co), the density of states of electrons is different for the spin-up and spin-down electrons, which leads to d band splitting as shown in Figure 1.3. This phenomenon also suggests that the scattering rates of spin-up and spin-down electrons are different. Electrons which experiences higher scattering rates leads to lower mobility and thus higher resistance i.e. 4s band electrons can be scattered to less mobile 3d states. When an electron leaves the first FM layer and enters the NM layer there will be additional scattering processes which leads to extra resistance. The resistance increase is originated from not only within the FM layers, but also at the FM/NM interface due to the different spins, which is a result of different density of states at the Fermi level. The same process also occurs when electrons leaves NM layer and enters

second FM layer. The resistance differences of parallel and antiparallel aligned systems can be explained using a two-current model as shown in Figure 1.4. The total current is composed of both spin-up and spin-down current, which are associated with spin-up and spin-down electrons. The electrons experience different resistance  $\rho_{\uparrow}$  and  $\rho_{\downarrow}$  depending on the spin orientation. When both FM layers are aligned, the spin-up electrons will experience low resistance and spin-down electrons will experience high resistance. In the parallel connection, the larger resistance will be shunted by the smaller resistance, and the total resistance of the system will be small. In the case of antiparallel alignment, both spin-up and spin-down electrons experiences moderate amount of resistance, and therefore the total resistance of the system will be high.

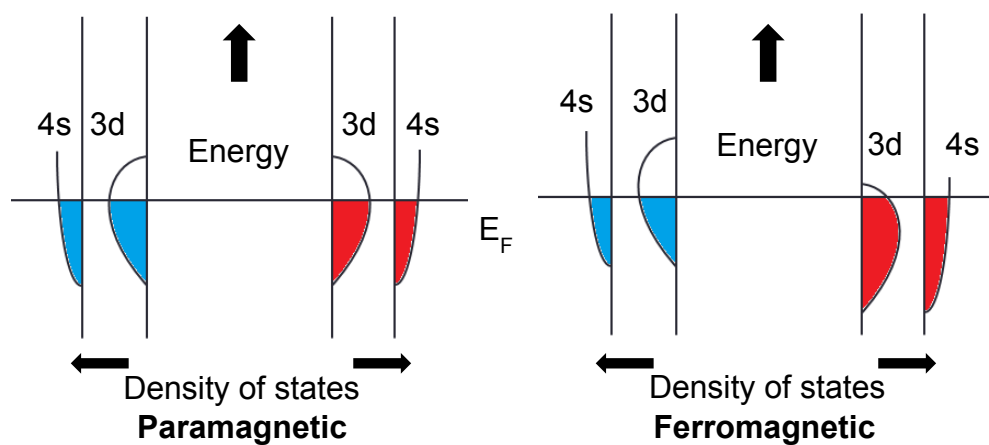


**Figure 1.3.** Density of states vs energy for 3d and 4s band for paramagnetic and ferromagnetic metals. (Day, 2007)

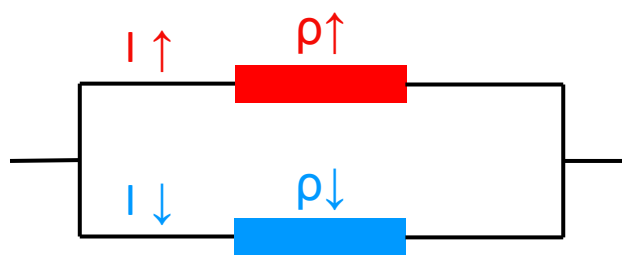


**Figure 1.4.** Two-current model for spin up and spin down electrons. (Fert, 2008)

Similar to GMR effect's FM/NM/FM structure, tunneling magnetoresistance (TMR) effect is a magnetoresistive effect of two ferromagnetic layers separated by a thin insulating layer (I). With sufficiently thin insulating layer, electrons can tunnel from one FM layer to the other. TMR is a consequence of spin-dependent tunneling. TMR is first described by Julliere<sup>8</sup>. In his model, tunneling of spin-up and spin-down electrons are two distinct processes, occurring in the two different spin channels. Julliere also assumed that the conductance is proportional to the effective density of states of the two FM for a particular spin orientation. The TMR process is shown in Figure 1.5. In parallel state, one of the spin-up or spin-down electrons has a large chance of tunneling through the barrier as shown in Figure 1.5a. However, in the antiparallel state, both spin-up or spin-down electrons have moderate chance of tunneling as shown in Figure 1.5b. Using the two-current model as described earlier, parallel alignment will lead to smaller resistance  $R_P$ , whereas the resistance of antiparallel alignment  $R_{AP}$  will be larger. According to these assumptions, the TMR can be written as follows

$$\text{TMR} = \frac{2P_1P_2}{(1 - P_1P_2)}$$

where  $P_1$  and  $P_2$  are spin polarization of ferromagnetic electrodes. In Julliere's theory on FM/NM junctions, the spin polarization is proposed as an intrinsic property of

ferromagnetic metal.  $P$  is zero when the electrode is non-magnetic;  $|P|$  is 1 when the density of state of the FM material is 100% spin-polarized at the Fermi level.

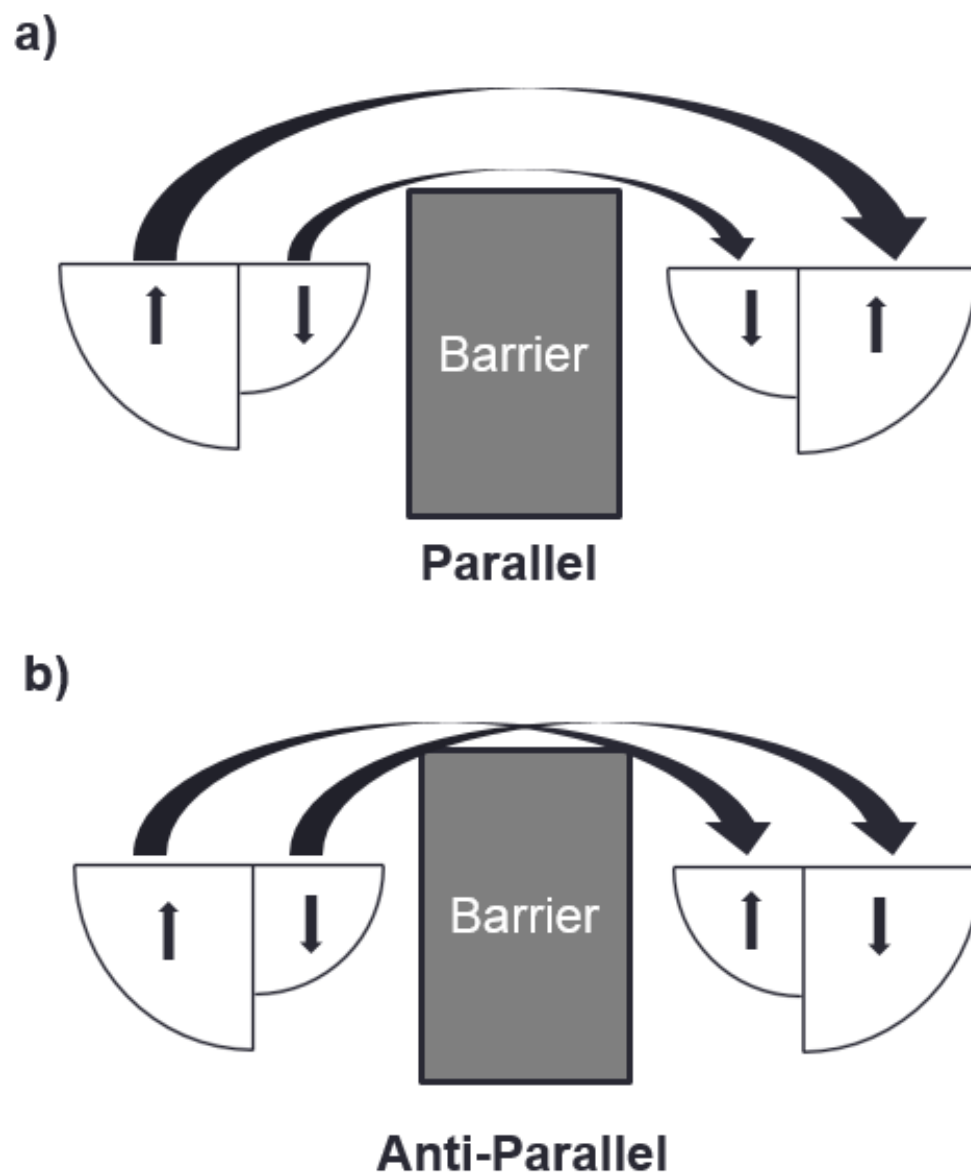


**Figure 1.5.** Density of states of spin-up ( $\uparrow$ ) electrons and spin-down ( $\downarrow$ ) electrons in a) parallel state and b) antiparallel state in magnetic layers. (Moodera *et al*, 2010)

### 1.1.5 Spin Valve

Spin valves are among one of the mostly studied spintronics devices for their application in memory device applications. Utilizing GMR or TMR effect, we can construct spin valves by sandwich a non-ferromagnetic metal such as Cr and Cu or insulating barrier such as MgO and Al<sub>2</sub>O<sub>3</sub> in between ferromagnetic metals with different coercivities. Spin valves are devices consisting of two ferromagnetic metals (FM) separated by a non-magnetic spacer layer (NM), and the electrical resistance across the junction has two states depending on alignments of the electron spins in the two ferromagnetic layers, which can be controlled by an external magnetic field. The high and low resistance state of the spin valves is analogous to “1” and “0” states of electronics. Spin valve devices were first implemented with GMR effect, discovered by Fert and Grunberg independently<sup>3-4</sup>. Later, spin valves were designed using tunneling TMR effect. Today, spin valves are widely implemented in a variety of solid-state devices including hard drives (non-solid-state drives), magnetic random-access memories (MRAM), and magnetic sensors.

The operation of a spin valve is shown in Figure 1.6. Assuming a FM1/NM/FM2 structure, the M-B hysteresis loop of FM1 is described in the blue curve, and the M-B loop

of FM2 is shown as the red curve in Figure 1.6. The coercivity of FM1 is  $C_{1a}$  and  $C_{1b}$ , and the coercivity of FM2 is  $C_{2a}$  and  $C_{2b}$ . If a large negative magnetic field is applied, both FM1 and FM2 will be aligned, giving a low resistance state. When the magnetic field increases to just below  $C_{1a}$ , FM1 and FM2 will be in an anti-parallel state, which has high resistance. If the magnetic field is decreased furthermore past  $C_{2a}$ , alignment of FM1 and FM2 will both be parallel aligned again, leading to small junction resistance, as shown in the green curve in Figure 1.6. Similarly, when we apply a large decreasing positive magnetic field, the curve can be traced by the purple dotted curve shown in Figure 1.6.

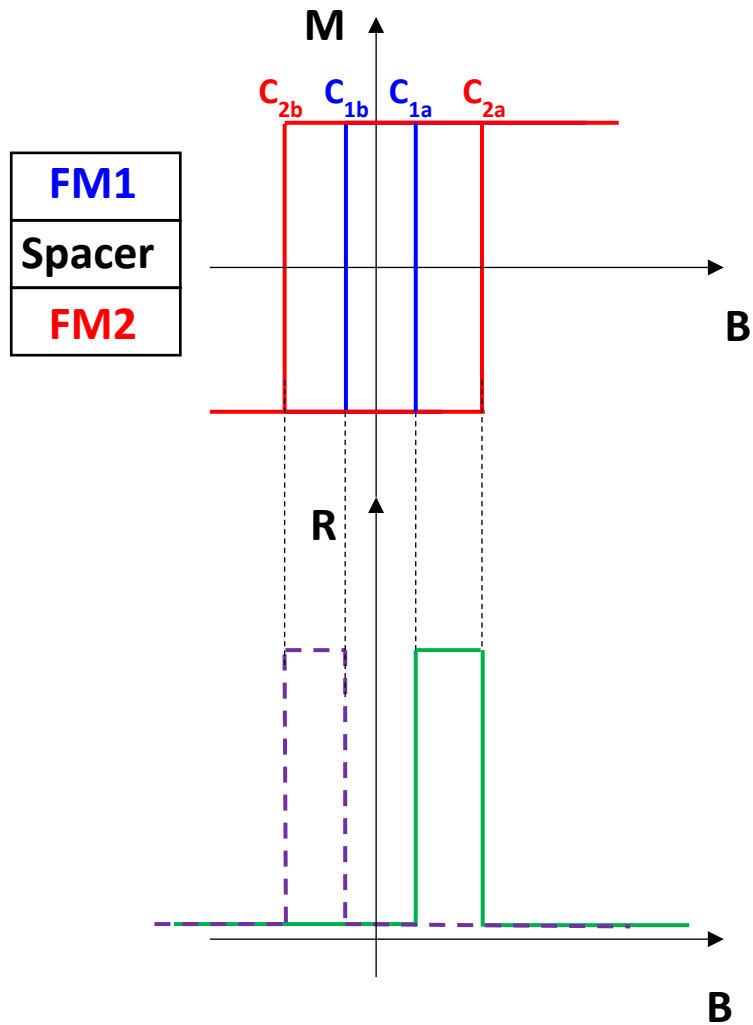


**Figure 1.6.** Operation of spin valve.

### 1.1.6 Spin Valve Review

In 1975, Julliere measured the properties of Fe/Ge/Co junctions, and

observed TMR of 14% at low temperatures<sup>8</sup>; however Julliere's result was not able to be reproduced until 1982 by Maekawa and Gafvert, which showed 2% TMR in a Ni/NiO/Co junction at 4.2K.<sup>9</sup> In the subsequent decade, many experiments were attempted to achieve large TMR at room temperature. Most of these results have low TMR ratio < 1 % at low temperatures, until Miyazaki *et al* and Moodera *et al* demonstrated large room temperature TMR > 10 % with amorphous Al-O as spacer layer independently<sup>10-11</sup>. In 1995, Miyazaki *et al* reported room temperature TMR up to 18% in Fe/Al<sub>2</sub>O<sub>3</sub>/Fe junctions, and 30% at 4.2K. The Al-O layer was prepared by oxidation in air for 24 h<sup>11</sup>. However, Miyazaki was not able to reproduce his result as the other Magnetic tunneling junctions (MTJs) fabricated in a similar condition only exhibits TMR ratio of 1 – 6 % at room temperature. Moodera also used Al-O as tunneling barriers but using oxygen plasma to oxidize aluminum. The CoFe/Al<sub>2</sub>O<sub>3</sub>/Co junctions had TMR ~10% and the results were reproducible.<sup>10</sup> Furthermore, the junctions have TMR ratio up to 24% at 4.2K. The TMR ratio reported by Miyazaki *et al* and Moodera *et al* were one magnitude higher than any other MTJs fabricated before. Two major reasons were attributed to the success of Al-O barriers. First, aluminum when oxidized, expands nearly ~27% which produces a nearly pin-hole free barrier. Secondly, the development of

thin film deposition techniques and vacuum technology dramatically improved from 1970s to 1990s. These experiments reveal that the quality of the barrier layer as well as junction interface plays a significant role in MTJ fabrication.

A variety of techniques were explored to improve the performance of Al-O MTJs, such as electrode materials and shapes<sup>12-17</sup> as well as post fabrication annealing<sup>13, 18-19</sup>. Different electrodes were tested including using an antiferromagnetic (AF) layer to pin one of the electrodes to by exchange bias. An exchange bias AF layer was introduced to achieve stable states at zero magnetic field, which was a well-practiced technique with GMR junctions. Exchange biased electrodes allowed the MTJs to be made more suitable for memory applications. The operation of AF-pinned MTJ are shown in Figure 1.7. Assuming a FM1/NM/FM2/AFM structure, the M-B hysteresis loop of FM1 is described in the blue curve, and the M-B loop of FM2/AFM is shown as the red curve in Figure 1.7. The coercivity of FM2/AFM layers are shifted due to the extra field needed to be overcome the torque in ferromagnetic and antiferromagnetic interface. The coercivity of FM1 is  $C_{1a}$  and  $C_{1b}$ , and the coercivity of FM2 is  $C_{2a}$  and  $C_{2b}$ . If a large positive magnetic field is applied, both FM1 and FM2 will be aligned, giving a low resistance state. When the magnetic field decreases to just below  $C_{2b}$ , FM1 and FM2 will be in an anti-parallel state, which has high

resistance. If the magnetic field is decreased furthermore past  $C_{1b}$ , alignment of FM1 and FM2 will both be parallel aligned again, leading to small junction resistance, as shown in the purple curve in Figure 1.7. Similarly, when we apply a large increasing negative magnetic field, the curve can be traced by the green curve shown in Figure. However, due to the shift in coercivity of the FM2/AFM, the shape of the “bump” of the green curve will be much wider than purple curve, which can simplify device operation and improve device performance.

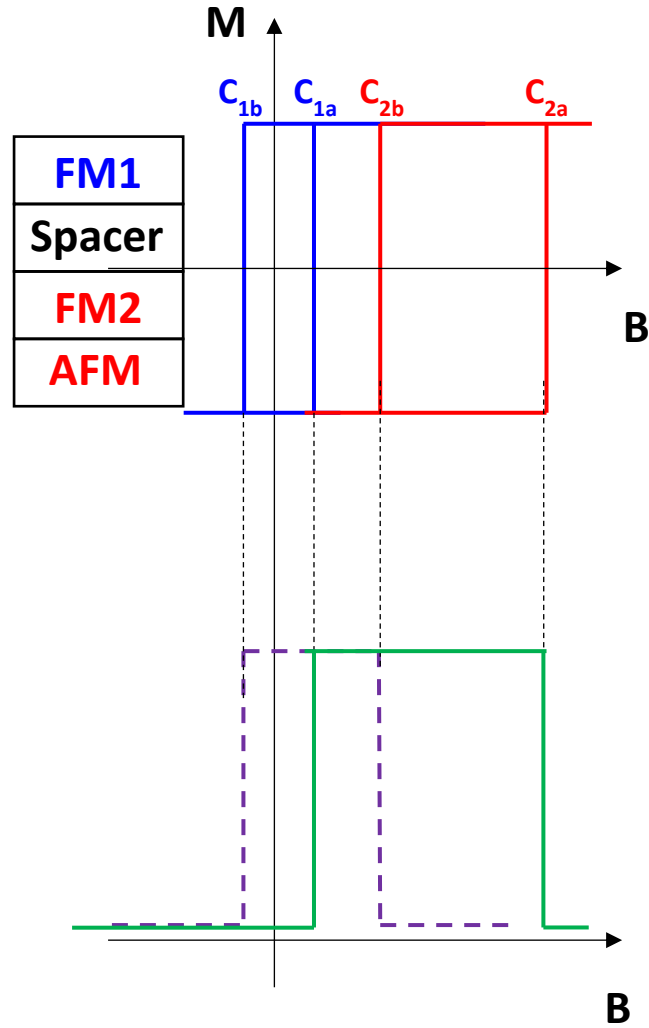


**Figure 1.7.** Operation of antiferromagnetic-pinned spin valve.

Sousa *et al* studied the thermal anneal process of MTJ and found TMR ratio increase from 22% to 36%. when the annealing temperature was less than 240°C<sup>18</sup>. When annealing

temperature exceeds 240°C, the inter-diffusion of MnRh AF layer caused barrier height and TMR value decrease. Later, AF layer capable of sustaining at higher temperature such as FeMn and IrMn were studied<sup>13</sup>. Parkin and his group at IBM also explored mass production capabilities by using e-beam lithography for the fabrication of MTJs<sup>20</sup>, which allows mass-scale fabrication of MTJ based devices. The highest TMR ratio for Al-O tunnel junctions at room temperature was 80% reported by Wei *et al* in Ta/Cu/Ta/IrMn/CoFe/Ru/CoFeB/Al-O/CoFeB/Ta/Ru structure.<sup>21</sup>

Through optimization of deposition condition, Al-O MTJs has nearly reached its theoretical performance by 2005. While other suitable materials are being explored by scientists<sup>22-24</sup>, first principle calculation predicts that single crystal MgO (001) as tunneling barrier would exceed 1000% TMR due to coherent tunneling.<sup>25-26</sup> MgO as tunneling barrier were fabricated before year 2000 but showed low TMR ratio due to poor crystal quality and deposition techniques. Bowen *et al* found that epitaxial grown single crystal Fe (001) / MgO / Fe (001) deposited by sputtering and laser ablation showed large improvement of MgO MTJ TMR value.<sup>16</sup> 27% TMR at room temperature and 60% TMR at 30K were reported by Bowen *et al*. This experiment gives proof that TMR value also depends on actual electronic structure of entire barrier/electrodes and not just on the spin polarization

of the surface states of FM electrodes. Later, epitaxial MgO MTJs were improved by increasing the barrier thickness by Faure-Vincent *et al*<sup>27</sup>, and obtained 67% room temperature TMR and 100% TMR at 80K.

In 2004, Parkin *et al* fabricated highly epitaxial CoFe/MgO/CoFe MTJs using ion beam and radio frequency (RF) magnetron sputtering.<sup>28</sup> As deposited MgO MTJs exhibits modest TMR ratio ~20 – 30%. Parkin found that thermal annealing < 400°C improves the MTJ quality and TMR ratio up to 220% at room temperature and over 300% at 4K. Also in 2004, Yuasa improved the epitaxial MgO MTJs by improving the growth condition of molecular beam epitaxy (MBE).<sup>29</sup> MgO (001) was first deposited as a seed layer for Fe (001) deposition. 100 nm of Fe (001) were then deposited and annealed at 350°C in ultra high vacuum. MgO source were then deposited at a slow rate of 0.01nm/s to prevent iron oxidation from the MgO source. Subsequently, Fe(001) were deposited on MgO (001) / Fe (001) at 300°C to prevent dislocation. The technique dramatically enhanced TMR ratio at room temperature to 180%. Later, Yuasa *et al* fabricated fully epitaxial Co(001)/MgO/Fe(001) and Co(001)/MgO/Co(001)MTJs by MBE and obtained 271%<sup>30</sup> and 410%<sup>30</sup> TMR respectively at room temperature. In 2006, Hayakawa *et al* reported MgO TMR value of 472% at room temperature and 804% at 5K by RF magnetron sputtering of

CoFeB/MgO/CoFeB layers. Hayakawa *et al* studied and compared the effects of high temperature annealing on AF pinned MTJs and MTJs without the AF pinning layer, and found that high temperature annealing over 450°C lowers the TMR value due to Mn and Ru inter-diffusion in to MgO barrier.<sup>31</sup> Ikeda *et al* demonstrated Ta diffusion may also lower TMR value when annealing temperature is above 500°C.<sup>32</sup> Ikeda *et al* showed the suppression of Ta diffusion by increasing the adjacent CoFeB electrode thickness lead to 604% TMR at room temperature (1100% at 5K).

The development of MTJs timeline is summarized in Figure 1.8. The red circle represents the development of Al-O MTJs, and the blue circle represents the development of MgO MTJs. The development of MTJs took nearly two decades to reach their theoretical limit of TMR ratios. Today TMR based devices are frequently used in HDD read heads. The junction resistance of MTJs can be easily tuned by the insulator area and thickness, which makes impedance matching easily achievable, and allows recording densities up to about 1 Tbit/inch<sup>2</sup>. Although, nowadays the performance of computer hard disks based on TMR effect has been outperformed by solid-state drives. That does not mean MTJ devices will be gradually fall into disuse. On the contrary, TMR based applications such as MRAM and even spin-RAM devices are still being widely researched for utilization in emerging

field such as nano-electronics and flexible electronics which requires low energy consumption and high-density devices. In conventional MRAM, the writing is done by magnetic field generated by currents, which becomes more difficult as devices downscale. However, in spin-RAM, the writing process uses the magnetization switching induced by spin-transfer torque, which is more suitable for high-density MRAM. Therefore, it is crucial that MTJs with other material systems should be studied to meet these requirements.

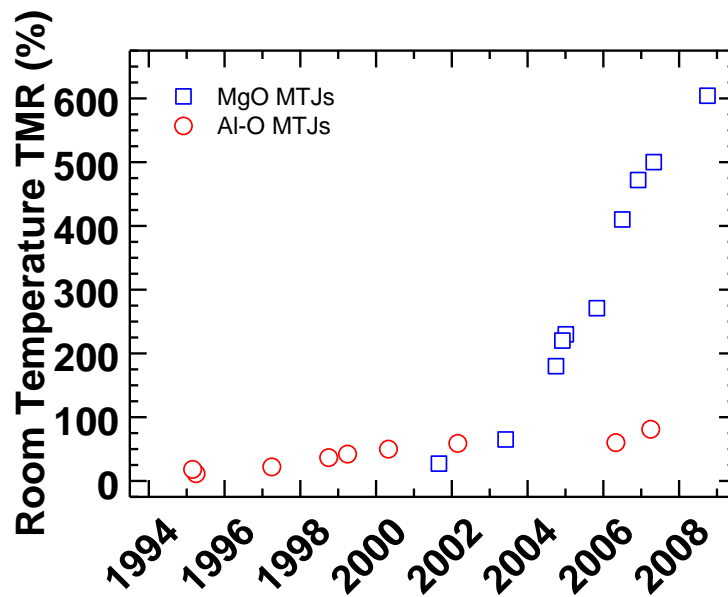


**Figure 1.8.** Development of tunnel magnetoresistance in magnetic tunnel junction from 1995 to 2008 for MgO<sup>16, 27-35</sup> and Al-O<sup>10-12, 15, 17-18, 21, 36-37</sup> junctions.

## 1.2 Two-Dimensional Materials

### 1.2.1 Graphene

Zero dimensional (0D) nano-particles and fullerenes, one dimensional (1D) nanowires and carbon nanotubes, and two-dimensional (2D) superlattice and nano-sheets have been widely studied in recent years. These nano-materials often possess different properties from their bulk crystal counterparts. 2D material such as graphene, monolayer hexagonal boron nitride (h-BN), and monolayer transitional metal dichalcogenides (TMDCs) have hexagonal in-plane crystal structures. In their bulk crystals, the multilayers layers stack together vertically with weak van der Waals bonding among the layers. Graphene is the first 2D material to be studied after two physicists, A.K. Geim and K. S. Novoslov reported the first-time experimental separation of atomically thin graphite<sup>38</sup>, or graphene, and the transport studies. Their work was later awarded the Nobel Prize in Physics in 2010<sup>39-40</sup>. Graphene is a flat monolayer layer of carbon atoms which has a honeycomb-shaped hexagonal lattice. It can be wrapped up into fullerenes and carbon nanotubes and stacked into graphite. The crystal symmetry and 2D nature of graphene leads to extraordinary electrical, mechanical and thermal properties. The chirality of graphene wave functions near the Dirac point suppresses scattering and makes graphene a zero-

bandgap material. Suspended graphene transistors have been demonstrated to have field mobility over  $230,000 \text{ cm}^2\text{V}^{-1}\text{s}^{-1}$  which are much higher than conventional semiconductors like Si ( $\sim 1500 \text{ cm}^2\text{V}^{-1}\text{s}^{-1}$ ). On the other hand, the strong covalence  $\sigma$ -bonds between the neighboring two carbon atoms brings graphene an exceptional large Young's modulus, which makes graphene one of the strongest material on earth. Graphene also exhibits high thermal conductivity and a negative thermal expansion. Although graphene is a promising material in many fields of application such as ultrafast photodetectors, chemical sensors, touch screen panels, and flexible electronics. However, graphene's drawback is its lack of a bandgap. Transistors fabricated using graphene channels suffer from low on-off ratio, and the devices cannot be "turned off". Many efforts have been put into graphene research in attempting to open a bandgap by quantum confinement techniques such as strain engineering<sup>41-42</sup>, creating wrinkles<sup>43</sup>, and patterning into nano-ribbons<sup>44-47</sup>, but researchers have limited success to create a bandgap suitable for device application.

### **1.2.2 Transition-Metal Dichalcogenides**

Transition-metal dichalcogenides are a family of layered materials that has regained attention since discovery of graphene in 2004. These materials include

semiconductors such as MoS<sub>2</sub> and WS<sub>2</sub>, semi-metals (WTe<sub>2</sub>, TiSe<sub>2</sub>), metals (NbS<sub>2</sub>, VSe<sub>2</sub>), and superconductors (NbSe<sub>2</sub>, TaS<sub>2</sub>). Especially MoS<sub>2</sub>, MoSe<sub>2</sub>, WS<sub>2</sub>, and WSe<sub>2</sub> are emerging group of materials with properties that make them highly attractive for fundamental studies in semiconductors and interface physics and for applications including electronics and photonics. Bulk MX<sub>2</sub> (M = Mo, W; X = S, Se) are indirect bandgap semiconductors, which are commonly used as dry lubricants in industries; however, monolayer MX<sub>2</sub> becomes direct bandgap semiconductor due to quantum confinement. Two common structural phases found in MX<sub>2</sub> are trigonal prismatic (2H) or octahedral (1T). In the 2H phases, MX<sub>2</sub> has lattices similar to graphene's honeycomb crystal structure. The metal and chalcogens forms an A-B-A stacking order in which the chalcogen atoms in different MX<sub>2</sub> layers are on top of each other in the direction perpendicular to the plane and occupy the same position A. The lattice structure, side view and top view of MX<sub>2</sub> crystal are shown in Figure 1.9a. 1T phases however, are stacked in an A-B-C order shown in Figure 1.9b. Depending on the ordering of transition metal (Mo or W) and chalcogen elements (S or Se), either 2H or 1T phase can be thermodynamically stable. For example, 2H MoS<sub>2</sub> and 1T MoTe<sub>2</sub> are stable, but 1T MoS<sub>2</sub> and 2H MoTe<sub>2</sub> are metastable. 2H MoS<sub>2</sub> can be converted into 1T MoS<sub>2</sub> by intercalating Li or K<sup>48-49</sup>, but it is thermodynamically

unstable and gradually converts back to the semiconducting 2H MoS<sub>2</sub> at room temperature. In addition, MoS<sub>2</sub> also has a rhombohedral 3R phase which has an ABCD stacking order as shown in Figure 1.9c. In thermal stable 2H phase, MX<sub>2</sub> (M = Mo, W; X = S, Se) are semiconductors. First principle calculation using density function theory reveals that the peak of the valance band changes its position with decreasing thickness of MX<sub>2</sub> layers, turning an indirect semiconductor at bulk into a direct semiconductor at monolayer thickness which gives rise to photoluminescence. 1T phase MX<sub>2</sub>, however, are metallic and have been used to effectively reduce the contact resistance in MX<sub>2</sub> materials<sup>50-52</sup> or as electrodes in hydrogen evolution<sup>53-54</sup>.

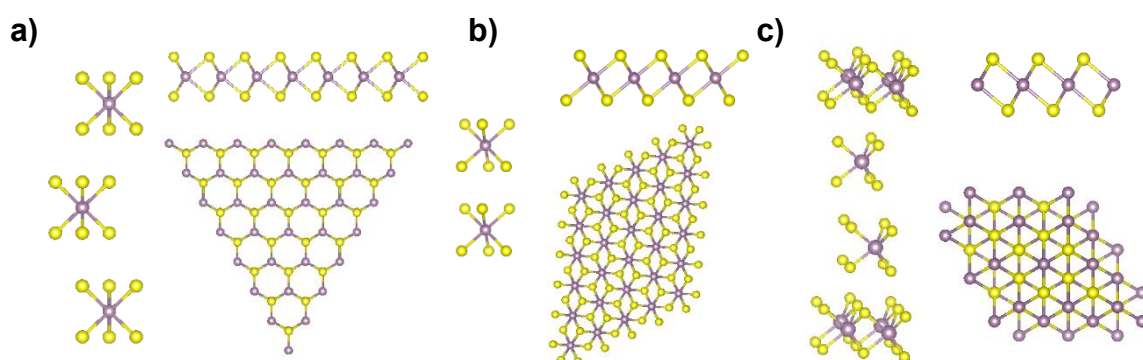


**Figure 1.9.** Crystal structure of MoS<sub>2</sub>. a) 2H-MoS<sub>2</sub>, b) 1T-MoS<sub>2</sub>, and c) 3R-MoS<sub>2</sub>.

Unique optical, electrical, mechanical, and chemical are interesting properties emerged from the single and few layered MX<sub>2</sub>. As mentioned previously, the layer thickness dependent indirect band gap at multilayer to direct band gap at monolayer transitions can be characterized by PL, which shows strong emission for monolayer MX<sub>2</sub>. Photodetectors<sup>55-56</sup>, light emitting diodes<sup>57-62</sup>, and photovoltaic<sup>63-64</sup> devices are all potential optical applications for MX<sub>2</sub> and have been demonstrated by various research groups in recent years. Theoretical calculations for monolayer MoS<sub>2</sub> predict a room-temperature electron mobility up to 1000 cm<sup>2</sup> V<sup>-1</sup> s<sup>-1</sup> and low-temperature values exceeding 10<sup>5</sup> cm<sup>2</sup> V<sup>-1</sup> s<sup>-1</sup>. The first demonstration of a high performance top-gated monolayer MoS<sub>2</sub> FET was reported by Kis *et al* with *n*-type channel, excellent on/off current ratio of ~10<sup>8</sup>, room-temperature field-effect mobility of ~ 200 cm<sup>2</sup> V<sup>-1</sup> s<sup>-1</sup>, and subthreshold slope of 74 mV per decade.<sup>65</sup> Also, monolayer and few-layered MX<sub>2</sub> have huge potential in flexible electronics. Mechanical measurements performed on single-layer MoS<sub>2</sub> show that it is stronger than steel and can sustain deformation up to 11%<sup>66</sup>, which implies MoS<sub>2</sub> is one of the strongest semiconducting materials, and can be integrated on to flexible substrates in various wearable electronics applications. First flexible TMDC transistors have been

demonstrated<sup>67-68</sup> using atomically thin MoS<sub>2</sub>, soon followed by full 2D transistors on flexible substrates using semiconducting 2D TMDCs, combined with metallic graphene and insulating BN.<sup>69-70</sup>

Besides electrical and optical properties, another important aspect of monolayer 2H TMDCs lies in electron band structure and their lack of inversion symmetry. The valence band maximum and the conduction band minimum are located at K and K'. Due to the broken inversion symmetry, the valence band splits 160 meV in the valence bands up to for MoS<sub>2</sub> and 460 meV for WSe<sub>2</sub> from spin-orbit interactions.<sup>71</sup> This enables the observation of valley-dependent physical phenomena and potential valley-tronics applications.<sup>72-73</sup>

### **1.2.3 Two-Dimension Materials Spin Valves Review**

2D materials such as graphene and TMDCs are promising candidate materials as spacer layers due to the sub-nanometer thickness, sharp interface, and its flexibility nature. Combined with the unique mechanical properties of 2D materials, 2D MTJs can be fabricated into flexible and higher density memory devices with low power consumption. The first demonstration of 2D spin valve was reported by Hill *et al* in 2006<sup>74</sup> using graphene

in a current-in-plane (CIP) geometry spin valve. In general, CIP spin valves performs better than current-perpendicular-to-plan (CPP) geometry spin valves and more suitable for academic studies due to simpler fabrication process; however, CIP geometry is not practical in devices due to large area requirements. In CIP structured spin valves, only one deposition process is required as all the electrodes can be deposited on spacer material at the same time. The coercivity can be tuned by varying the dimension of the electrodes. However, in CPP spin valves, three or more depositions are required for the two FM electrodes as well as the spacer layer. In 2007, Karpan *et al* explored the potential of graphene layers for vertical MTJ junctions.<sup>75</sup> Theoretical calculations were performed on FM / graphene / FM junctions and predicted near 100% spin filtering. This result implies that TMR ratio of graphene MTJs could exceed hundreds of%. The first demonstration of CPP graphene spin valve was reported in 2008 by Mohiuddin *et al*<sup>76</sup>. The graphene MTJ were fabricated on SiO<sub>2</sub>(100nm)/Si substrate on permalloy (Py, NiFe) electrode arrays. Mechanical exfoliated graphene was then transferred to patterned Py electrodes on Si substrate. The SiO<sub>2</sub> thickness was chosen such that enough optical contrast will be provided to be able to identify graphene layers on the surface of SiO<sub>2</sub>/Si substrates. Top Py electrode were subsequently fabricated using e-beam lithography. The TMR of Py/graphene/Py was 0.4%.

Due to oxidation of Py electrodes, the authors deposited Au layer on top of Py electrode and increased TMR ratio to ~5%.

In 2012, Cobas *et al* proposed another fabrication method for graphene MTJs<sup>77</sup>. First, SiN with circular aperture were deposited on Py electrodes, followed by wet transfer of CVD grown graphene. Bottom electrodes were formed at the exposed area of graphene i.e. area not covered by SiN layer. 5 nm of SiO<sub>2</sub> were subsequently deposited and with openings on top of graphene to form exposed area for top electrode contact. Finally, top electrode is formed by depositing 20 nm of Co. With this systematic approach of fabrication, Cobas *et al* reported TMR of > 2% at low temperatures<sup>77</sup>. Many studies on graphene MTJs were soon reported soon after with TMR ~ 1%.<sup>78-81</sup> In 2014, Park *et al* reported 4.6% TMR at 4.2K using 'flip-transfer' process to prevent bottom Py electrode from oxidation.<sup>82</sup> With similar idea to prevent electrode oxidation, Li *et al* fabricated graphene MTJs by first suspending graphene membrane on etched SiN window followed by depositing ferromagnetic metals on both sides of to form Py/graphene/Co MTJs<sup>83</sup>. TMR ratio up to 3.4% was reported by Li *et al*. In 2016, a major increase of TMR in graphene MTJ was reported by Cobas *et al*. 5% and 12% magnetoresistance at room temperature and 15 K were found in NiFe/graphene/Fe junctions.<sup>84</sup> The increase in TMR ratio is attributed by

directly growing graphene on NiFe/Al<sub>2</sub>O<sub>3</sub> substrates which eliminates the transfer process.

These studies reveal the importance of junction quality affected by fabrication.

Besides graphene, other 2D materials were also studied as spacer layer for MTJs. Dankert *et al* reported h-BN based spin valve<sup>85</sup>. h-BN was wet-transferred to Py electrodes and Co electrodes were subsequently deposited. The TMR of Co/h-BN/Py spin valves showed TMR ratio of 0.5% corresponding to spin polarizations of  $P = 0.25\%$ . Similar studies in 2016 reported h-BN/graphene spin valves had TMR ratio of 0.85% at room temperature and 1.88% at 4.2K<sup>86</sup>. A major increase of TMR in BN junctions were observed when Piquemal-Banci *et al* directly deposited h-BN on Fe electrodes. Monolayer BN was grown on Fe thin films using borazine catalysts. Co metals were subsequently deposited forming top contact. ~6% TMR was reported at low temperature and the spin-polarization of FM/h-BN was 17%. Novel 2D material such as black phosphorous (BP) were also investigated as insulating layer. Xu *et al* first synthesized BP bulk crystal by heating red phosphorus in high pressure at 1000°C. Few-layered BP layers were subsequently exfoliated to Py electrodes using scotch tape. Xu *et al* reported 0.57% MR at 4K and 0.23% at room temperature.<sup>87</sup>

In contrast to graphene and h-BN, TMDCs are semiconductors which can be doped

with dopants to tune their bandgaps and electrical properties. Low contact resistance has been achieved in  $\text{MX}_2$  FET using Chloride doped  $\text{MX}_2$  as electrical contacts.<sup>88</sup> Furthermore, doping with a small amount of magnetic elements such as Mn can turn  $\text{MX}_2$  into 2D ferromagnetic material, known as diluted magnetic semiconductor<sup>89</sup>, which has been a major research area in spintronic in the past two decades due to the possible functionality of manipulation the freedom of both charge and spin therein

Recently, a few studies of 2D TMDC spin valves have been reported. Wang *et al* fabricated a  $\text{MoS}_2$  spin valve by using CVD grown monolayer  $\text{MoS}_2$  as junction spacer layer, and observed  $\text{MoS}_2$  spin valve TMR ratio of 0.4% at 20K, but did not observe room temperature TMR<sup>90</sup>. Wang and coworkers subsequently inserted Au layer on top of Py electrodes to prevent oxidation during fabrication process and observed TMR increase to 0.73% at 10K, corresponding to 6% of spin polarization at FM/ $\text{MoS}_2$  interface. In 2017, Dankert *et al* fabricated Co/multilayered  $\text{MoS}_2/\text{Al-O}/\text{Py}$  spin valve.<sup>91</sup> The thin layer of Al-O is introduced to prevent oxidation of bottom FM electrodes. The  $\text{MoS}_2/\text{Al-O}$  spin valve showed TMR of  $\sim 0.5\%$  at 300K and  $\sim 2\%$  at 75K. Since Al-O is a commonly used material in MTJs, the motives of Dankert *et al*'s were unclear. However, in DFT cautions performed by Dankert and coworkers also pointed out in an ideal junction, the maximum spin

polarization between MoS<sub>2</sub> and FM is 26%, or TMR ratio of 7%. Other TMDC spin valves were also studied. Iqbal *et al* used mechanical exfoliated WS<sub>2</sub> as junction spacer layer and fabricated spin valve with room temperature TMR ratio of 0.15%<sup>86</sup>. Zhao *et al* reported 0.21% TMR at 300K in Py/WSe<sub>2</sub>/Py junctions, where the WSe<sub>2</sub> were exfoliated multi-layers (n ~ 9).<sup>92</sup>

The development of 2D material spin valves is summarized in Figure 1.10. Figure 1.10a summarizes the development of graphene, h-BN, and BP spin valves, and the progress in MX<sub>2</sub> spin valves are summarized in Figure 1.10b. Most studies are reported after 2012 and TMR values are typically below 1% due to contamination at FM/I interface from fabrication process. However, with direct growth on FM metals, TMR values for graphene and b-BN MTJs were able to perform much better. Although the TMR ratios for 2D material spin valves are low compared to MgO junctions, 2D spin valves have potential to become next generation spintronics devices for the following reasons. First, 2D materials have uniform surface, pinhole free, and no dangling bonds, which makes them perfect material for MTJs. Traditional tunnel barrier materials such as Al-O and MgO have out-of-plane bonds, and difficult to control quality and uniformity. The durability of 2D materials is also superior to traditional materials. Graphene, b-BN, and MX<sub>2</sub> are all highly thermal

durable, and makes them ideal for diffusion barriers. The flexible nature of 2D materials also makes them top candidates for flexible memory devices. Finally, novel 2D materials and merging 2D material such as black phosphorus (BP) and MXenes all have unique properties. Stacking these 2D materials could lead to customized spin valves with high TMR ratio. The semiconducting  $\text{MX}_2$  also allows layered diluted magnetic semiconductors to be implemented as top and bottom electrodes of spin valves and realize full 2D spin valves.

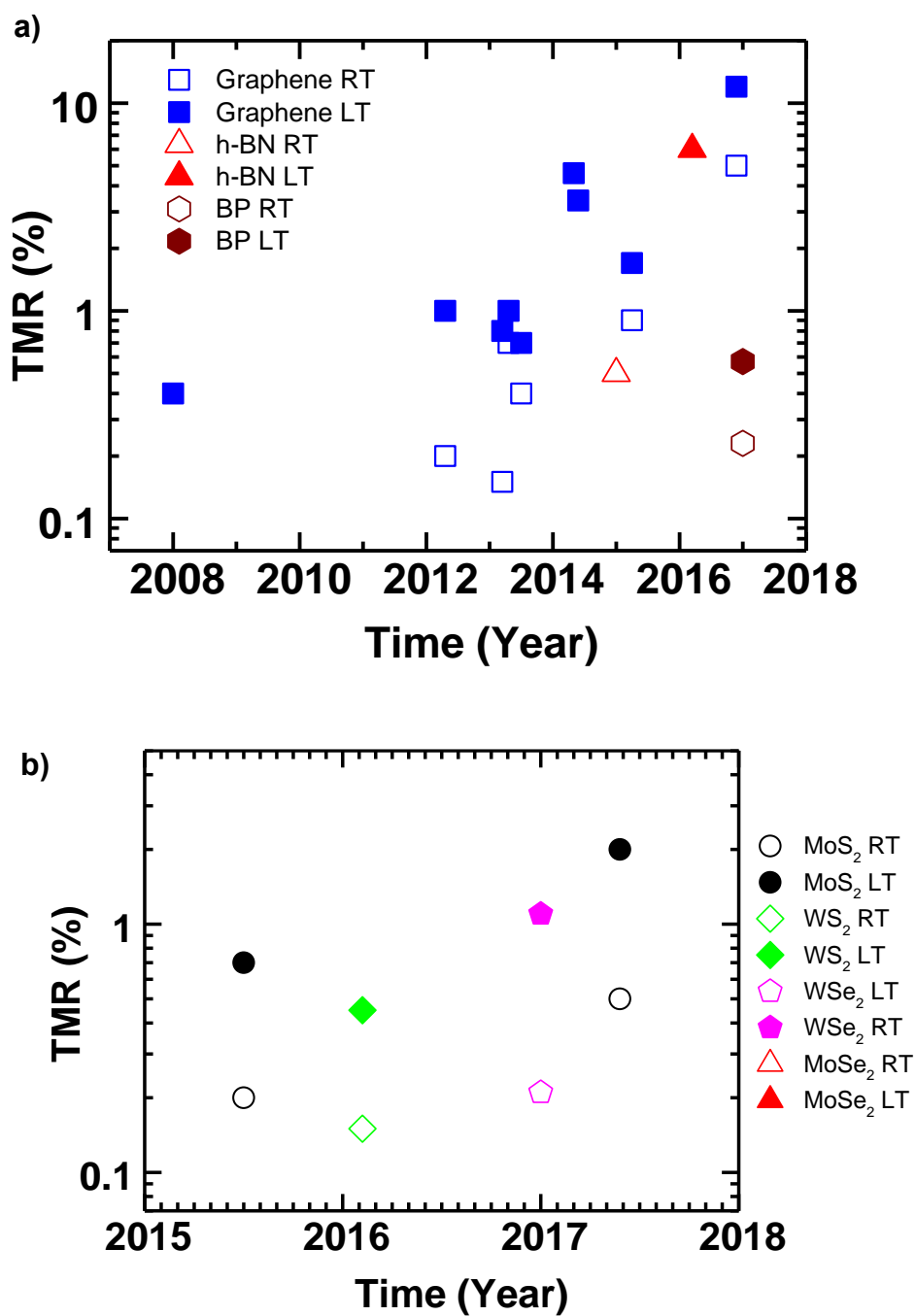


**Figure 1.10.** Development of 2D material spin valve. a) Development of graphene, h-BN, and block phosphorous spin valves from 2008 to 2017. b) Summary of MoS<sub>2</sub>, WS<sub>2</sub> and WSe<sub>2</sub> spin valves from 2015 to 2017.

## CHAPTER 2

### GROWTH OF MONOLAYER TRANSITION-METAL DICHALCOGENIDES

#### 2.1 Introduction to MX<sub>2</sub> (M = Mo, W; X = S, Se) Growth

During the early stages of MX<sub>2</sub> material research, the recipe for high quality and large area growth of MX<sub>2</sub> was not yet developed. Researchers relied on top-down synthesis method such as mechanical and liquid exfoliation, as well as laser thinning to produce few-layered MX<sub>2</sub>. Mechanical exfoliation was by far the most popular approach due to its simplicity and extremely cheap cost.<sup>38</sup> The weak van der Waals force between the layers allows MX<sub>2</sub> layers to be separated by scotch tape repeatedly until a few layers of MX<sub>2</sub> remains. Although mechanical exfoliation of MX<sub>2</sub> produces pristine quality MX<sub>2</sub> nanosheets, the method ultimately lacks control of the size and uniformity of layers in the exfoliated nanosheets. Typically, only a few exfoliated MX<sub>2</sub> crystals on the substrate are thin ( $n < 10$ ) and only a few microns in size. Furthermore, the thickness of the exfoliated nanosheets cannot be determined unless lengthy measurements are performed. The majority of the exfoliated MX<sub>2</sub> crystals are still bulk ( $n > 10$ ). On the contrary, liquid exfoliation and ion intercalation produces large yield of mono to few layered MX<sub>2</sub> compared to mechanical exfoliation. Coleman *et al* sonicated bulk MoS<sub>2</sub> crystals in solvent

with different surface tensions such as N-Methyl-2-pyrrolidone (NMP) and isopropyl alcohol (IPA), then centrifuged to obtain few layered MoS<sub>2</sub>, and other 2D materials.<sup>93</sup> Coleman and coworker's studies also indicated that the structure of MoS<sub>2</sub> may be damaged as the field mobilities of the flakes are  $\sim 0.01 \text{ cm}^2\text{V}^{-1}\text{S}^{-1}$ . Interestingly however, Li intercalation of MoS<sub>2</sub> triggers the 1T' phase change, which transforms semiconducting 2H-MoS<sub>2</sub> to metallic 1T'-MoS<sub>2</sub><sup>94</sup>. Finally, laser thinning was another technique to produce mono- to few layered MX<sub>2</sub>. Castellanos-Gomez *et al* uses argon ion laser ( $\lambda = 514\text{nm}$ ) to thin down a mechanical exfoliated multi-layer MoS<sub>2</sub> to mono-layer and characterized by optical microscopy, atomic force microscopy (AFM), and Raman spectroscopy<sup>95</sup>. Field mobility of laser thinned MoS<sub>2</sub> were  $0.04 - 0.49 \text{ cm}^2\text{V}^{-1}\text{s}^{-1}$ , comparable to pristine exfoliated monolayer MoS<sub>2</sub> crystals. The top-down approach of synthesizing monolayer MX<sub>2</sub> is summarized in Table I. Despite many efforts done by researchers, top-down synthesis suffers from a variety of problems such as size, shape, and uniformity of the exfoliated nanosheets.

**Table I.** Top-down synthesis method for monolayer MX<sub>2</sub>

<b>Method</b>	<b>Advantage</b>	<b>Disadvantage</b>
Mechanical exfoliation	High quality	Cannot control of size Non-Uniformity of layer Low yield Lacks capability of large scale production
Liquid exfoliation	Large yield Converts to 1T MoS <sub>2</sub>	Contamination Size & uniformity problem Lacks capability of large scale production
Laser thinning	High quality	Low Yield Limited by laser spot size Requires exfoliated flakes to begin with. Lacks capability of large scale production

The growths for 2D TMDs have made tremendous advances in recent years. MoS<sub>2</sub> was the first MX<sub>2</sub> nanosheets to be synthesized, soon followed by MoSe<sub>2</sub>, WS<sub>2</sub>, and WSe<sub>2</sub>. Different methods were explored to develop a recipe for high quality MX<sub>2</sub> growth, such as sulfurization and selenization of thin transitional metal films<sup>96</sup>, vapor-solid growth from direct evaporation of MoS<sub>2</sub> source power<sup>97</sup>, and chemical vapor deposition (CVD) using transition metal oxides and chalcogenides as precursors<sup>98-99</sup>. One of the first successful

demonstration of large area synthesis of polycrystalline MoS<sub>2</sub> nanosheets was conducted by Liu *et al* by dip coating insulating substrates in (NH<sub>4</sub>)<sub>2</sub>MoS<sub>4</sub> followed by annealing with Ar at 500°C.<sup>100</sup> The hydro-thermal reaction synthesized MoS<sub>2</sub> have low crystallinity and must be further annealed at a higher temperature at 1000°C with Ar and S vapor to improve its crystallinity. Liu *et al* also observed that the S annealing process improved MoS<sub>2</sub> transistor device mobility by two orders and device on-off ratio by three orders.

Although other methods such as sulfurization of Mo<sup>96</sup>, MoCl<sub>5</sub><sup>101</sup>, or MoO<sub>2</sub><sup>102</sup> have been studied, the most popular MoS<sub>2</sub> growth nowadays is CVD using MoO<sub>3</sub> and S as precursors. Lee *et al* studied MoS<sub>2</sub> growth using MoO<sub>3</sub> and S as CVD precursors.<sup>98</sup> Triangular and star shaped MoS<sub>2</sub> single crystals monolayers were grown on rGO (reduced graphene oxide), PTAS (perylene-3,4,9,10-tetracarboxylic acid tetrapotassium salt) treated SiO<sub>2</sub>/Si substrates. The synthesized MoS<sub>2</sub> nanosheets were confirmed to be monolayers by AFM, Raman, and PL spectroscopy. Later, Ling *et al* further studied the effects of various seeding promoters and found optimized concentration of seed molecules and increased the nucleation of MoS<sub>2</sub> nanosheets.<sup>103</sup> Using PTAS as a seeding agent allows large monolayer MoS<sub>2</sub> single crystals to be synthesized at relatively low growth temperature at 650°C. However, most of the seed molecules were organics and great caution must be taken to

minimized sample contamination. The growth of MoSe<sub>2</sub>, WS<sub>2</sub>, and WSe<sub>2</sub> on the other hand, were successfully grown at a later time due to more complex growth parameters<sup>104-109</sup>. In this chapter, the growth mechanism and optimization process of MX<sub>2</sub> is discussed.

## 2.2 Growth Setup

Large area single crystal MX<sub>2</sub> monolayers were synthesized using MoO<sub>3</sub>/WO<sub>3</sub> and S/Se as precursors. The CVD process is carried out in a home-built growth system shown in Figure 2.1.

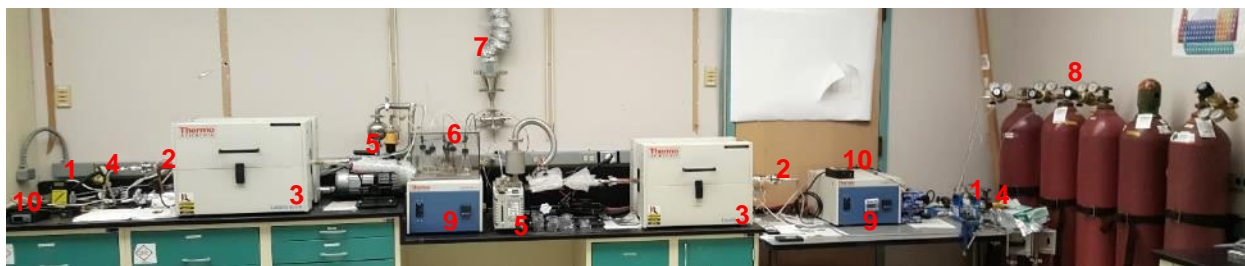


**Figure 2.1.** Digital camera image for home-built CVD growth system for MX<sub>2</sub> growth.

The components of the home-built CVD system and its function are listed below:

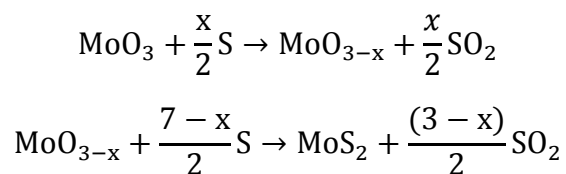
1. Mass flow controllers: Control flow rates of carrier gas Ar and H<sub>2</sub>.
2. Heating tape: A secondary heating source to evaporate S or Se.
3. Tube furnace: Primary heating source to elevate temperature of transition-metal tri-oxides source powder and substrates.
4. Vacuum gauge: Conventional vacuum gauge to monitor chamber pressure.
5. Mechanical pump: A rotary oil pump to perform low pressure growth if required.
6. Exhaust system: A three-flask system allows deposition of unwanted vapors and monitors gas flow.
7. Exhaust pipeline: Connects waste gas from exhaust system to building's exhaust line.
8. Gas cylinders: Ar, and H<sub>2</sub>.
9. Furnace console: Controls furnace temperature as well as other parameters.
10. Heating tape controller: Controls the output temperature of heating tapes.

### **2.3. Growth Method**

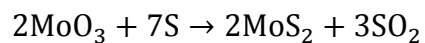
CVD growth of MoS<sub>2</sub> and MoSe<sub>2</sub>

Heating tapes were wrapped around the upper end of the quartz tube to create a separate heating zone. Sulfur or selenium sources are heated upstream by heating tape while  $\text{MoO}_3$  source powder and substrates are placed in the center of the furnace as shown in the growth setup schematic in Figure 2.2a.  $\text{SiO}_2/\text{Si}$  and Si substrates were cleaned with acetone, IPA, and DI (de-ionized) water.  $\sim 1$  mg of  $\text{MoO}_3$  powders were evenly spread across the Si substrate, which serves the purpose of a quartz boat, to ensure the  $\text{SiO}_2/\text{Si}$  substrate to source powder distance were kept uniformly as shown in Figure 2.2b.  $\text{SiO}_2/\text{Si}$  substrate was subsequently placed facing down on top of the Si substrate and  $\text{MoO}_3$  powders, forming a sandwich structure. The substrates and  $\text{MoO}_3$  powders sandwich were then placed inside a quartz tube at the center of the heating zone of a tube furnace. The furnace was first heated to  $550 - 575^\circ\text{C}$  rapidly at a rate of  $30^\circ\text{C}/\text{s}$ , then further heated to  $875^\circ\text{C}$  for  $\text{MoS}_2$  growths and  $800^\circ\text{C}$  for  $\text{MoSe}_2$  growths at a slower rate of  $\sim 10^\circ\text{C}/\text{s}$  as the S/Se was being evaporated at  $115^\circ\text{C}/300^\circ\text{C}$  by the heating tape. The temperature of furnace was kept at  $875^\circ\text{C}/800^\circ\text{C}$  for 10 mins before the furnace is shut off and cooled down naturally. The temperature profile of the growth is shown in Figure 2.2c. The growth is carried out in vacuum with pressure  $\sim 5$  Torr. 50 sccm Ar was used for  $\text{MoS}_2$  growth. The growth mechanism of can be explained by the following. First,  $\text{MoO}_3$  starts to evaporate

~550°C, and S vapor is introduced at this time. The S vapor will reduce MoO<sub>3</sub> into volatile MoO<sub>3-x</sub> species, which then reacts with S, forming MoS<sub>2</sub>. The chemical reaction can be described by the following equations.



Or simply



Monolayer MoSe<sub>2</sub> is grown similarly to MoS<sub>2</sub>. However, Se cannot serve as a reduction agent to reduce MoO<sub>3</sub> into MoO<sub>3-x</sub> species even at high temperature. Therefore, H<sub>2</sub> must be introduced to effectively reduce MoO<sub>3</sub>. In monolayer MoSe<sub>2</sub> growth, the Ar and H<sub>2</sub> flow rate 80 and 20 sccm respectively.

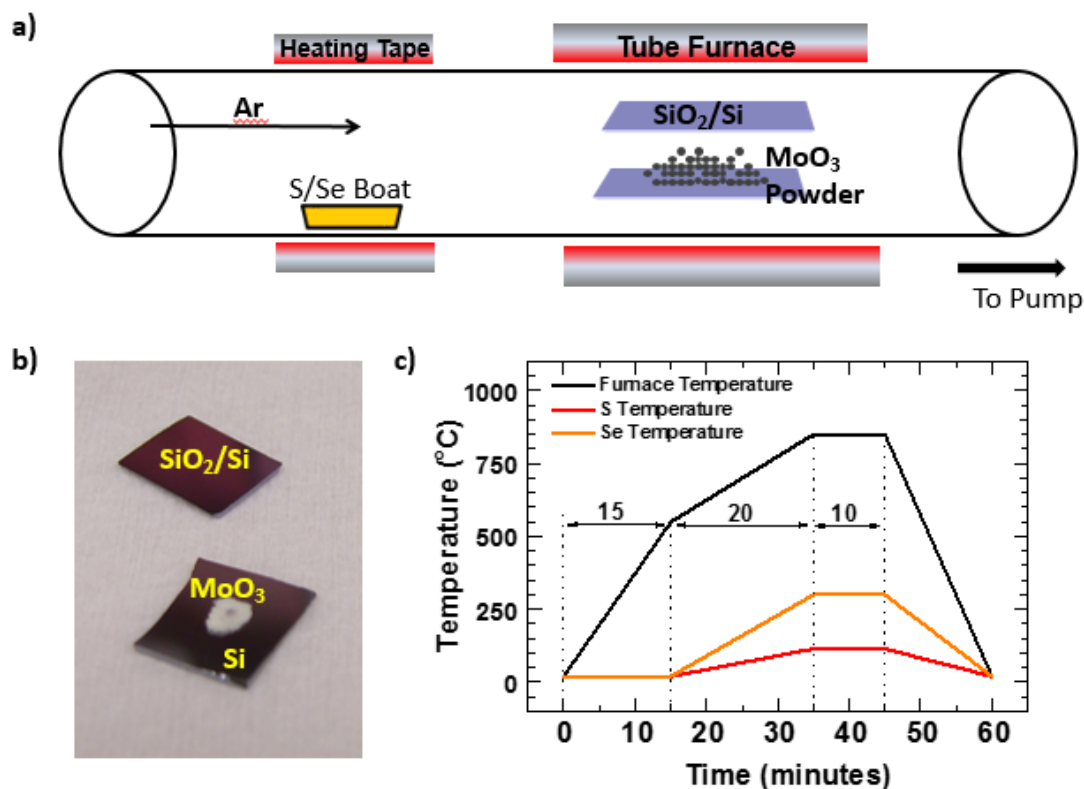


**Figure 2.2.** Synthesis of monolayer MoS<sub>2</sub> and MoSe<sub>2</sub>. a) Schematics of growth setup. b) Digital camera image of MoO<sub>3</sub> powders mounted on Si substrate. c) Temperature profile of furnace and heating belt temperature for MoS<sub>2</sub> and MoSe<sub>2</sub> growth.

### CVD growth of WS<sub>2</sub> and WSe<sub>2</sub>

WO<sub>3</sub> powder was loaded in a quartz boat placed at the center of the heating zone of tube furnace. The set point of the furnace was set to 1075°C. The substrates were placed downstream at the edge of the furnace heating zone where the temperature was lower and

had sharp temperature gradient from  $\sim 1000 - 500$  °C. S or Se source were supplied upstream heated by a heating tape. In  $WS_2$  growth, the S temperature was  $\sim 190^\circ\text{C}$  and in  $WSe_2$  growth, the Se temperature was  $260^\circ\text{C}$ . Ar gas was used as carrier gas and supplied from upstream. The schematic of the growth setup is shown in Figure 2.3a. Similar to  $MoSe_2$  growth, Se source powder cannot effectively reduce  $WO_3$  to  $WO_{3-x}$  vapor species, therefore  $H_2$  gas must be supplied. The Ar flowrate for  $WO_3$  growth was 100 sccm; the Ar and  $H_2$  flowrate for  $WSe_2$  growth was 80 and 20 sccm respectively. The growth time for both  $WS_2$  and  $WSe_2$  were 120 mins, and the growths were carried out in ambient pressure. The heating profiles for the furnace and heating tape are shown in Figure 2.3b.

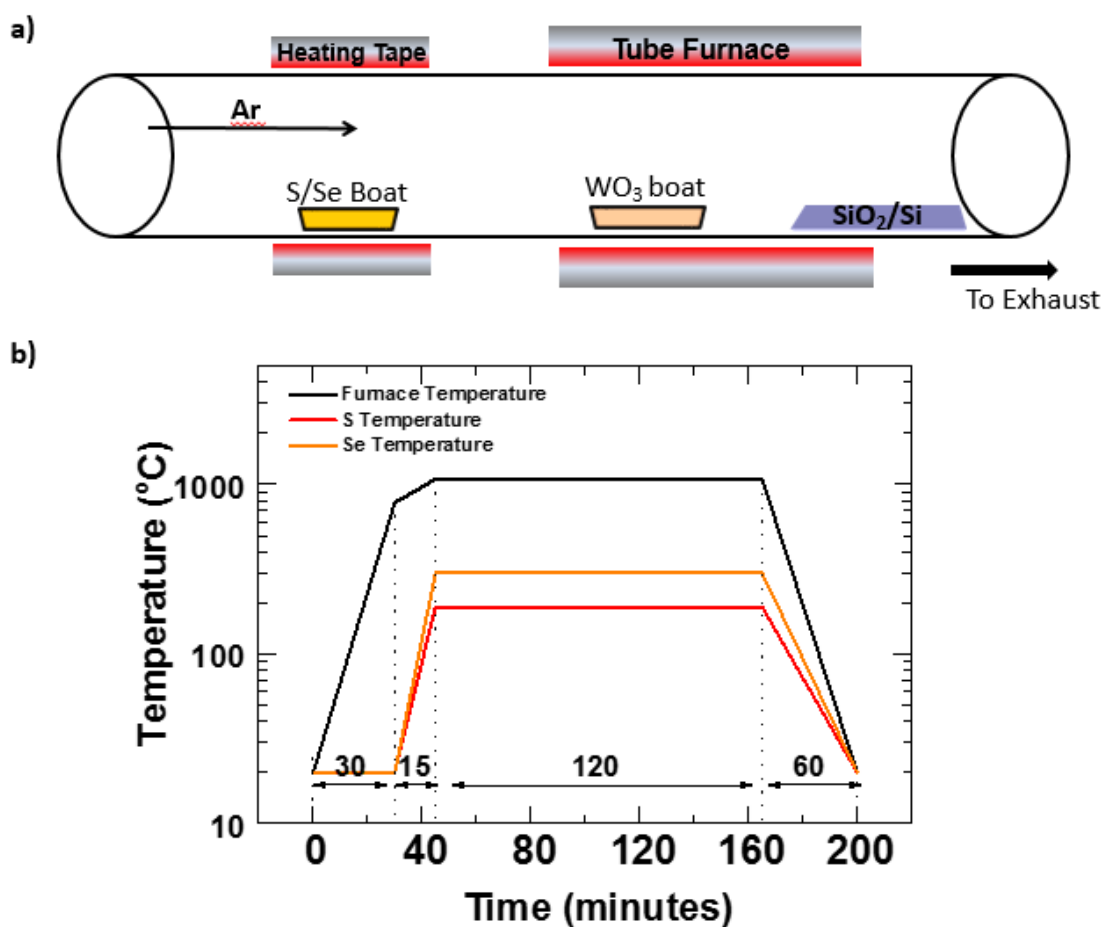


**Figure 2.3.** Synthesis of monolayer  $WS_2$  and  $WSe_2$ . a) Schematics of growth setup. b) Temperature profile of furnace and heating belt temperature for  $WS_2$  and  $WSe_2$  growth.

## 2.4. Optimization of $MX_2$ Growth parameters

### Effect of Sulfur/Selenium Temperature

In monolayer  $MX_2$  growth, S/Se temperature and their timing are undeniably the most

important parameter. As discussed earlier, S/Se are vital not only because they are required precursors to complete chemical reactions but are also a reduction agent. In general, MoO<sub>3</sub> powders are the limiting reactant in MoS<sub>2</sub> and MoSe<sub>2</sub> growths due to its low melting point (795°C) compared to the growth temperature at ~850°C. In vacuum, MoO<sub>3</sub> does not melt, but rather sublimes directly at ~700°C. Furthermore, in monolayer MoS<sub>2</sub>/MoSe<sub>2</sub> growths, the required MoO<sub>3</sub> precursors are typically less than 5 mg for a 1 cm<sup>2</sup> area substrate. On the other hand, WO<sub>3</sub> precursors has a very high melting point at 1473°C. The WO<sub>3</sub> source temperature in WS<sub>2</sub> and WSe<sub>2</sub> growths are below 1100°C, which drastically limits the amount of evaporated WO<sub>3</sub> vapor. Additionally, WS<sub>2</sub> and WSe<sub>2</sub> growths requires much longer growth time compared to MoS<sub>2</sub> and MoSe<sub>2</sub> growths. As a result, WO<sub>3</sub> source powders are susceptible to sulfurization or selenization. Fresh WO<sub>3</sub> powders have pale yellow color as shown in Figure 2.4a. After 60 minutes of growth time, the WO<sub>3</sub> powders darkens but partially sulfurized to grey color as shown in Figure 2.4b. Further increasing the growth time continues sulfurize WO<sub>3</sub> powders until a layer of S – W compounds forms on top of the powders. This layer of S – W compound may limit the evaporation of WO<sub>3</sub>, which increases the difficulty to grow large area single crystal WS<sub>2</sub> or WSe<sub>2</sub>. Therefore, controlling S or Se vapor species should be the most critical aspect in monolayer MX<sub>2</sub>

growths.

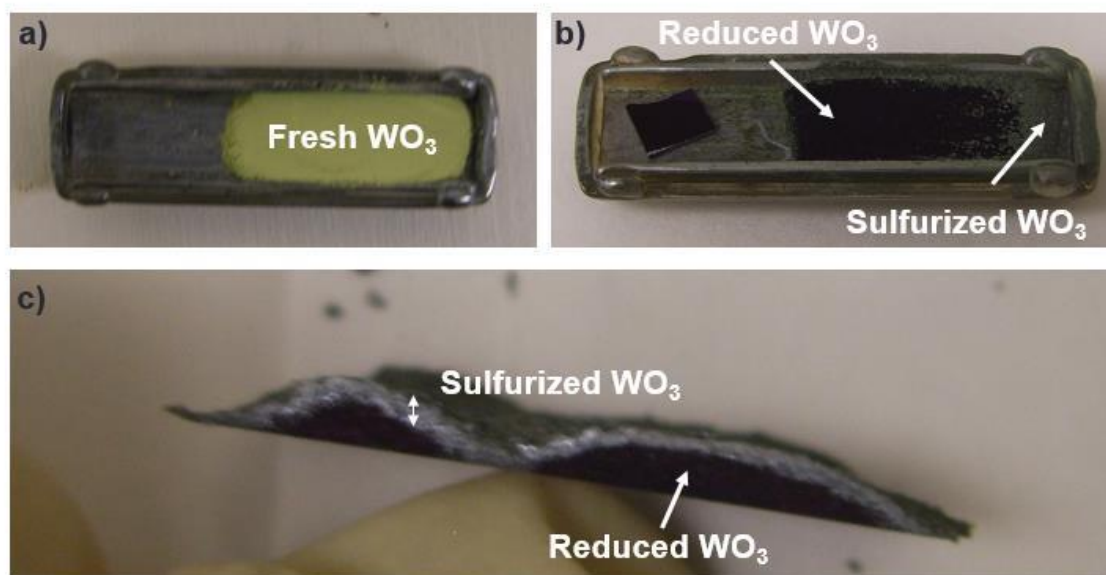


**Figure 2.4.** Sulfurization of WO<sub>3</sub> powders. a) Fresh WO<sub>3</sub> powders mount on a quartz boat. b) WO<sub>3</sub> powders after 60 minutes of growth with S temperature set at 190°C. c) WO<sub>3</sub> powders after 120 minutes of growth with S temperature set at 190°.

The temperature of S/Se directly influences the amount of S/Se vapors introduced in tube furnace. OM images of grown morphology of MoS<sub>2</sub> and MoSe<sub>2</sub> growths under different S or Se temperatures are shown in Figure 2.5. In MoS<sub>2</sub> and MoSe<sub>2</sub> growths, in the absence of S (T < 100 °C) or Se (T < 220 °C), no chemical reaction takes place therefore no or few depositions takes place on the substrate as shown in Figure 2.5a and d. In the

case of insufficient sulfur ( $100 < T < 110$  °C) or selenium ( $220 < T < 270$  °C), a mixture of  $\text{MoS}_2/\text{MoSe}_2$ ,  $\text{MoO}_2$  and oxysulfide ( $\text{MoOS}_2$ ) or oxyselenide ( $\text{MoOSe}_2$ ), which is a composite of  $\text{MoS}_2$  (or  $\text{MoSe}_2$ ) and  $\text{MoO}_{3-x}$  is found on the substrates instead as shown in Figure 2.5b and e. Finally, if sufficient S or Se is provided, triangular or hexagon shaped single crystal  $\text{MoS}_2$  or  $\text{MoSe}_2$  are deposited on  $\text{SiO}_2$  substrate as shown in Figure 2.5c and 5. The shape of grown  $\text{MoS}_2$  and  $\text{MoSe}_2$  can be explained by the Wulff constructions of crystal growth<sup>99, 107, 110-111</sup>. In  $\text{MX}_2$  the edge of the crystal can be either M terminated or X terminated. Triangular morphology occurs when stoichiometric ratio of X:W is larger than 2 or smaller than 1/2, ie. sulfur-rich or sulfur-poor environment, M or X -terminated edges grow fast. The resulting crystal will have either M or X -terminated edges with triangular shape. However, under the conditions where X: M stoichiometric ratio is 2:1, the growth rates of Mo and S terminations are the same, and thus the final shape of the crystal is hexagonal shaped. This phenomenon is demonstrated in Figure 2.6. Two  $\text{MoS}_2$  growths were carried out in same condition using 6 mg of  $\text{MoO}_3$  as precursors carried out at 850°C except S temperature. In Figure 2.6a, the S sulfur temperature is at 127°C, and hexagonal shaped  $\text{MoS}_2$  were observed. In Figure 2.56, the S sulfur temperature is slight higher at 130°C, and triangle shaped  $\text{MoS}_2$  were grown.

S and Se temperatures also play important roles in synthesizing large area monolayer WS<sub>2</sub> and WSe<sub>2</sub> single crystals. WS<sub>2</sub> crystals were grown at ~1070°C with 100 sccm of Ar flow but under different S temperature. Figure 2.7a-c shows the effect of S temperatures on morphology of WS<sub>2</sub> crystals. When S temperature was kept at 190°C during growth, as-grown WS<sub>2</sub> crystals were mostly monolayers with higher nucleation density. However, when S temperature increases to 200°C, multi-layer WS<sub>2</sub> started to dominate. The phenomenon can be explained by the increase in evaporated S vapor, which directly relates to S temperature, which then reduces and reacts with WO<sub>3</sub> vapor. At 240°C S temperature, a reduction of nucleation points was observed, meanwhile, as-grown WS<sub>2</sub> crystals were still mostly multilayers as shown in Figure 2.7c. During the growth, WO<sub>3</sub> source powders were exposed to S vapor. During this time, WO<sub>3</sub> powders were either reduced to WO<sub>2</sub>, which cannot react with S, or being directly converted to WS<sub>2</sub> powders. This lead to the reduction in WS<sub>2</sub> crystal growth. Se temperature also has similar impact on CVD WSe<sub>2</sub>. Figure 2.7 d-f shows the OM images of WSe<sub>2</sub> crystals grown at Se temperature of 235°C, 250°C and 300°C respectively. With insufficient Se, as-grown WSe<sub>2</sub> crystal were polycrystalline and has irregular shapes as shown in Figure 2.7d. With optimized Se temperature at 250°C, monolayer single crystals with ~50 μm domain size were found

evenly distributed on SiO<sub>2</sub> substrates. However, when excessive amount of Se were introduced during growth, multi-layered WSe<sub>2</sub> were found instead. Additionally, these multi-layer WSe<sub>2</sub> flakes attracts nearby WSe<sub>2</sub> vapor, forming black colored WSe<sub>2</sub> nano-beams grown vertically on thick WSe<sub>2</sub> flakes..

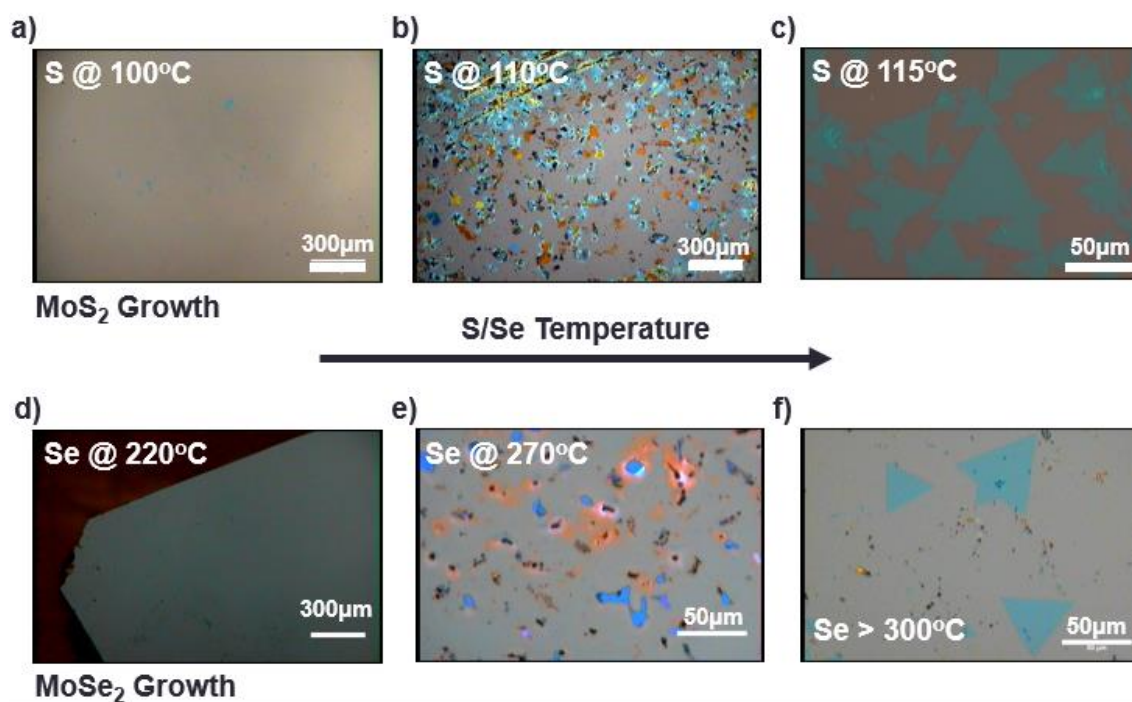


**Figure 2.5.** Optical Images of S and Se temperature effect on growth morphology. a) MoS<sub>2</sub> growth with S temperature at 100°C. b) MoS<sub>2</sub> growth with S temperature at 110°C. c) MoS<sub>2</sub> growth with S temperature at 115°C. d) MoSe<sub>2</sub> growth with Se temperature at 220°C. e) MoSe<sub>2</sub> growth with Se temperature at 275°C. f) MoSe<sub>2</sub> growth with Se temperature greater than 270°C

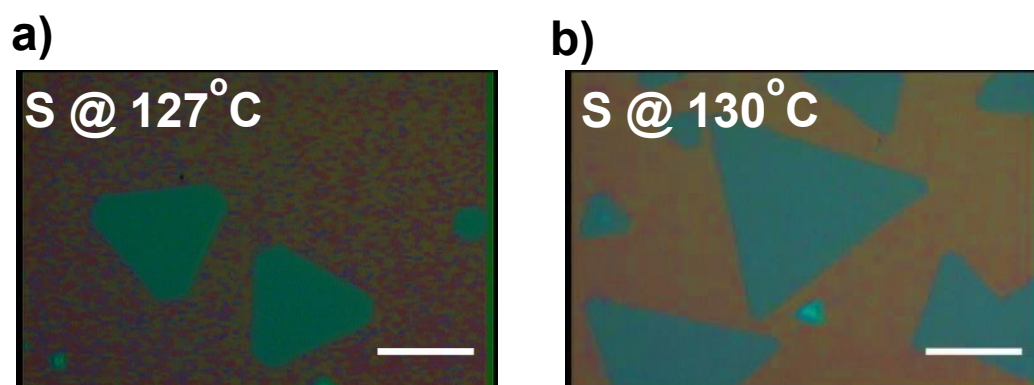


**Figure 2.6.** Optical microscope of monolayer MoS<sub>2</sub> crystal grown at different S temperature. a) S temperature of 127°C, and b) S temperature of 130°C. The scalebar in both images are 50  $\mu\text{m}$ .

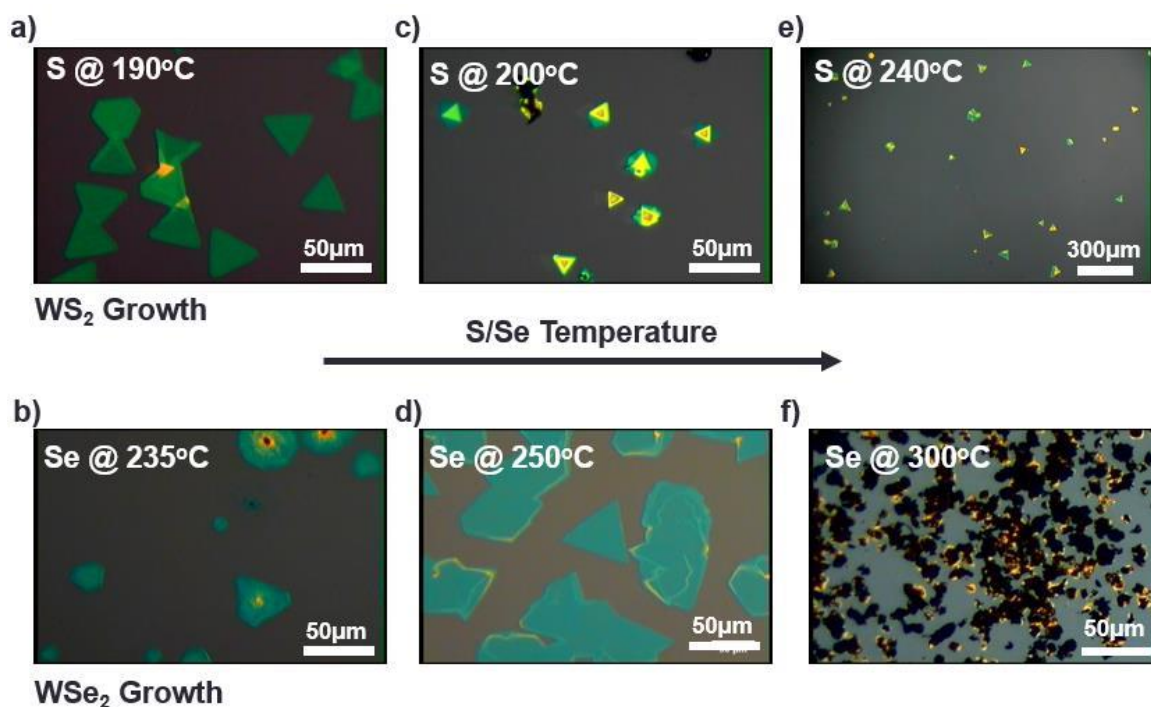


**Figure 2.7.** Optical Images of S and Se temperature effect on growth morphology in WS<sub>2</sub> and WSe<sub>2</sub> growths. a) WS<sub>2</sub> growth with S temperature at 190°C. b) WS<sub>2</sub> growth with S temperature at 200°C. c) WS<sub>2</sub> growth with S temperature at 240°C. d) WSe<sub>2</sub> growth with Se temperature at 235°C. e) WSe<sub>2</sub> growth with Se temperature at 250°C. f) WSe<sub>2</sub> growth with Se temperature at 300°C

### Effect of Growth Temperature

Figure 2.8 shows the OM images of MoS<sub>2</sub> crystals grown at different substrate temperatures. During the growths, the S temperature were kept at 120°C, the Ar flow rate

were kept at 50 sccm and the growth time were 10 mins. Initially, the growth temperature was at 700°C, MoS<sub>2</sub> with small grain size forming a fog-like morphology was observed on the substrate as shown in Figure 2.8a. When the growth temperature in increased to 800°C, monolayer MoS<sub>2</sub> of single crystal domains ~10 – 30 μm were randomly grown on the SiO<sub>2</sub> substrates' surfaces. However, the black-colored MoO<sub>3</sub> powders shown in Figure 2.8b indicates that MoO<sub>3</sub> powders were not fully evaporated. Next, the growth temperature is further elevated to 875°C. Larger single crystal MoS<sub>2</sub> monolayers with domain size of ~50 μm are observed on SiO<sub>2</sub> substrates as shown in Figure 2.8c. Finally, at high source and substrate temperature of 950°C, as-grown MoS<sub>2</sub> crystals grows more rapidly and connects with nearby domains, forming continuous MoS<sub>2</sub> monolayer nanosheets. The morphology difference can be explained by the following mechanisms. First, the growth temperature directly effects vapor pressure of MoO<sub>3</sub> generated. Second, nucleation density is proportional to substrate temperature. At low temperatures ( $T < 800^{\circ}\text{C}$ ), not enough MoO<sub>3</sub> vapor species were evaporated, leading to higher nucleation density but smaller domain size of MoS<sub>2</sub> on SiO<sub>2</sub> substrates. However, at higher temperature ( $T > 800^{\circ}\text{C}$ ), MoS<sub>2</sub> nucleation probability is suppressed which promotes lateral growth and thus forming large single crystal domains.

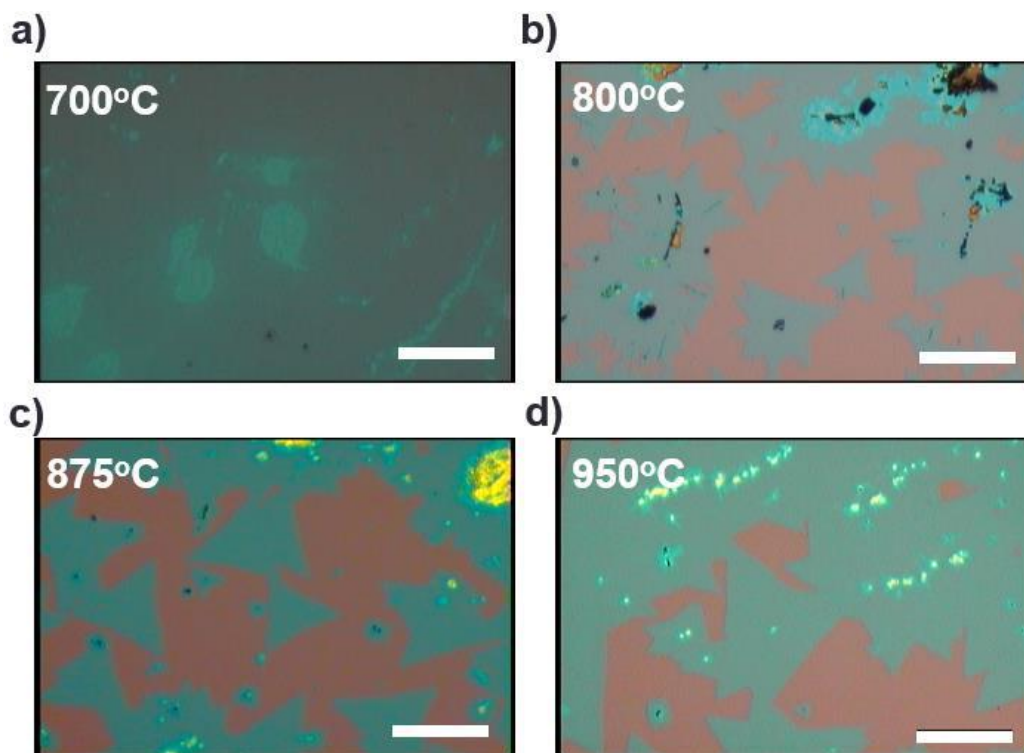


**Figure 2.8.** Optical microscope of monolayer MoS<sub>2</sub> crystal grown at different substrate and MoO<sub>3</sub> source temperature at a) 700°C, b) 800°C, c) 875°C and d) 900°C. The scalebar in the images are 50 μm.

As previously mentioned, in WS<sub>2</sub> growths, the substrates are placed at the heating zone edge, where the temperature has a sharp temperature gradient. Figure 2.9 shows the morphology of WS<sub>2</sub> crystals at different distances relative to the heating zone edge. At the furnace heating zone edge, small single crystal multilayer WS<sub>2</sub> were observed on SiO<sub>2</sub> substrate as shown in Figure 2.9a and b. As the substrate moves further away from the

heating zone, the nucleation density increases due to lower temperature as shown in Figure 2.9 c-f. The optimal growth condition was determined to be  $\sim 3 - 4$  cm away from furnace heating zone edge, where large single monolayer  $\text{WS}_2$  with domain size of  $\sim 200 \mu\text{m}$  were observed.

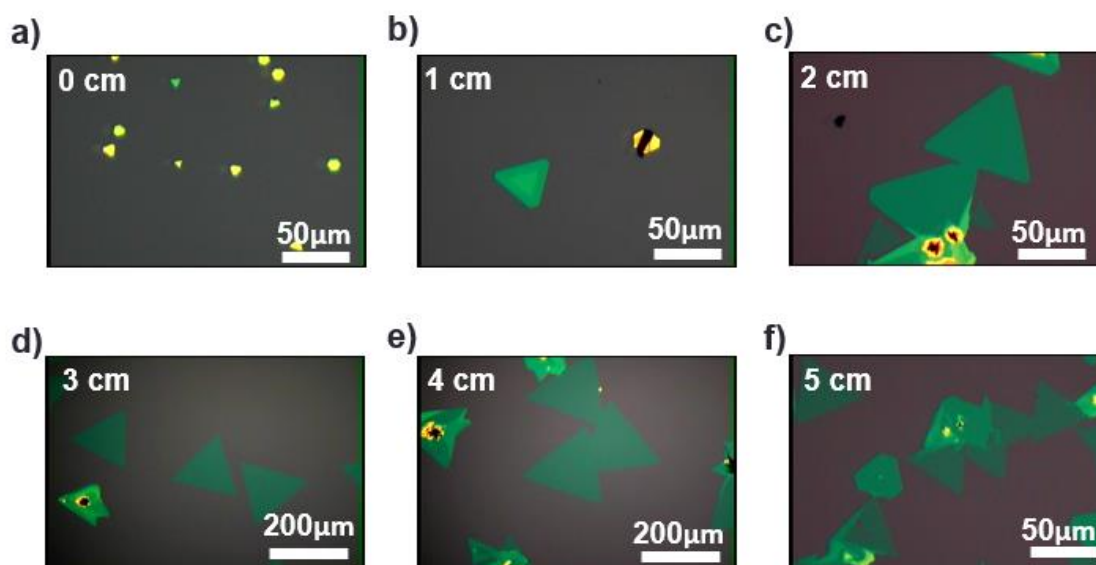


**Figure 2.9.** OM images of  $\text{WS}_2$  grown at different temperature. a) 0 cm, b) 1 cm, c) 2 cm, d) 3 cm, e) 4 cm, and f) 5 cm away from heating zone edge.

Since WSe<sub>2</sub> growths shares similar setup as WS<sub>2</sub> growth, ie. substrates are placed near heating zone edge; the effects of growth temperature can also be studied by the morphologies of as-grown WSe<sub>2</sub> crystals at different distances relative to heating zone. Polycrystalline multi-layer WSe<sub>2</sub> were observed closer to heating zone as shown in Figure 2.10a and 2.10b. When SiO<sub>2</sub> substrates are placed further away from the heating zone, monolayer single crystal WSe<sub>2</sub> were observed. The lower growth temperature also results higher nucleation density as shown in Figure 2.10c and 2.10d.

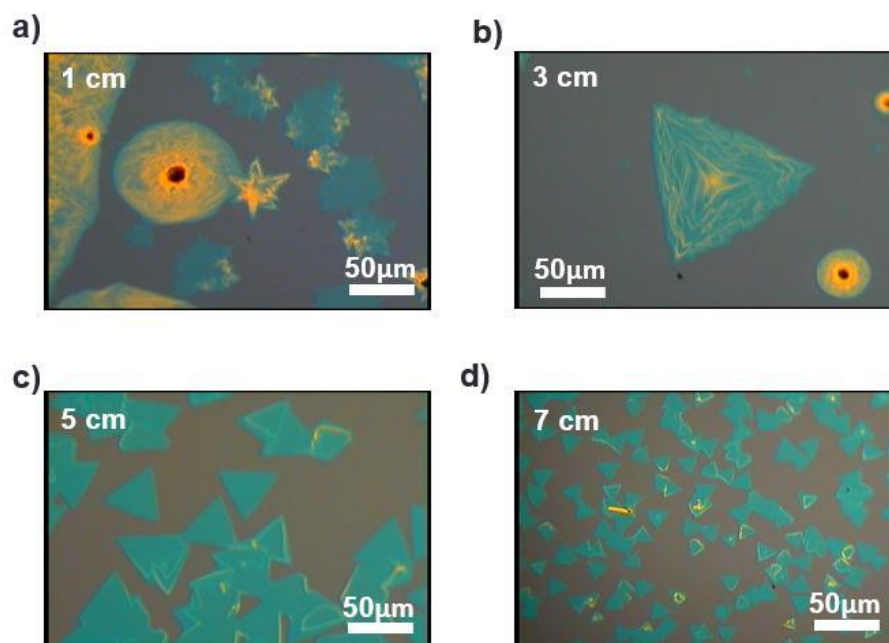


**Figure 2.10.** OM images of WSe<sub>2</sub> grown at different temperature. a) 1 cm, b) 3 cm, c) 5 cm, and d) 7 cm away from heating zone edge.

### Effect of Flow Rate

CVD-MoS<sub>2</sub> were grown on SiO<sub>2</sub>/Si substrates at 875°C for 5 mins at various flow rates. S temperature were kept at 130°C during the growth. Figure 2.11 shows the effect of MoS<sub>2</sub> growth under at different flow rates. First, MoS<sub>2</sub> is grown at low flow rate of 50 sccm, large single crystals with domain size of ~50 – 100 μm are evenly grown on the substrates as shown in Figure 2.11a. In Figure 2.10b, the flowrate is increased to 80 sccm, the grain size

of MoS<sub>2</sub> crystals shrunk to ~20 μm. In addition, more nucleation points are observed throughout the substrate. When the flowrate is further increased 100 sccm, MoS<sub>2</sub> grains are reduced even more, leading to large area of substrates covered by monolayer MoS<sub>2</sub> as shown in Figure 2.11c. Finally, if high flow rate of 200 sccm is introduced during MoS<sub>2</sub> growth, the grain size is suppressed, and large numbers of nucleation points can be observed on the substrate, leading to nearly fully covered MoS<sub>2</sub> as shown in Figure 2.10d.

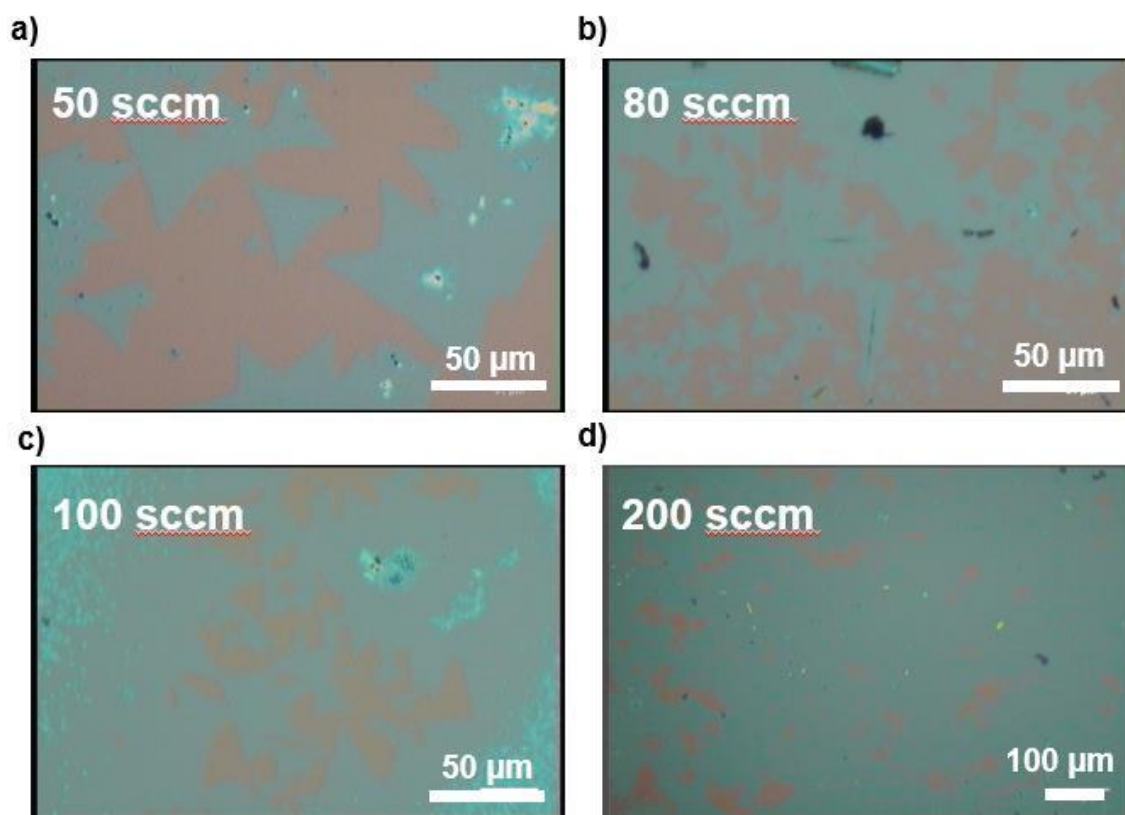


**Figure 2.11.** OM images of MoS<sub>2</sub> monolayers grown at a) 50 sccm, b) 80 sccm, c) 100 sccm, and d) 200 sccm.

In WS<sub>2</sub> and WSe<sub>2</sub> growths, flow rate does not have a noticeable impact of the morphology of crystals. However, the morphology of as-grown WSe<sub>2</sub> is heavily impacted by the gas mixture ratio of Ar and H<sub>2</sub>. Two WSe<sub>2</sub> growths were carried out in same growth conditions other than the gas flow rates. In the first setup, Ar and H<sub>2</sub> flow rate were kept at

60 sccm and 10 sccm respectively during the growth. In the second setup, Ar and H<sub>2</sub> were kept at 70 sccm and 25 sccm respectively. The OM images of grown single crystal monolayer WSe<sub>2</sub> are shown in Figure 2.12. In Figure 2.12a, WSe<sub>2</sub> grown at Ar : H<sub>2</sub> ratio of 6:1 has triangular shaped with smooth edges, whereas WSe<sub>2</sub> grown at Ar : H<sub>2</sub> ratio of 3:1 is flower shaped. The shape difference of the two growths originates from H<sub>2</sub> etching effect. In WSe<sub>2</sub> growths, H<sub>2</sub> is not only important to help the reduction process of WO<sub>3</sub>, but also highly reactive at high temperatures. Under high H<sub>2</sub> environment, H<sub>2</sub> reacts with active bonds in growing WSe<sub>2</sub> crystals, and cause rapid growths in certain directions and results in leaf-shaped morphology.

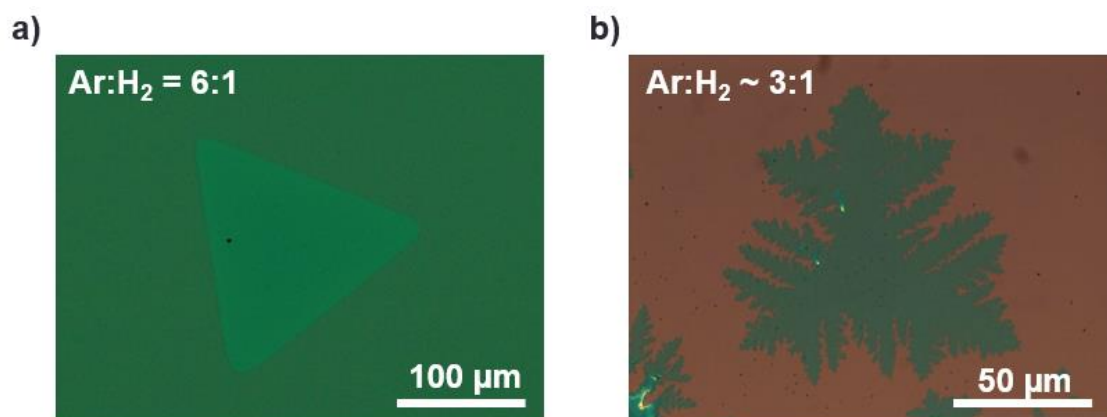


**Figure 2.12.** Effect of Ar:H<sub>2</sub> on WSe<sub>2</sub> growths. a) Optical microscope image of a single crystal WSe<sub>2</sub> flake grown with Ar:H<sub>2</sub> = 6:1. b) Optical microscope image of a single crystal WSe<sub>2</sub> flake grown with Ar:H<sub>2</sub> = ~3:1

### 2.5 Effect of Vapor Pressure

Through the collective effort of many research groups, the development of MX<sub>2</sub> (M = Mo, W; X = S, Se) growths have made significant advances in a few years, with millimeter scale monolayer MoSe<sub>2</sub> single crystals<sup>112</sup> and wafer-scale polycrystalline MoS<sub>2</sub><sup>113</sup> already being demonstrated. 2D materials growths are often carried out in simple tube furnace setups, consisting of horizontal tube furnace, quartz tubes, mass flow controllers, and pressure controllers. While these setups are economical and effective in synthesizing various 2D materials, they do not offer the same level of controls found in

many advanced deposition systems. For example, MBE systems have the capabilities of controlling partial vapor near the substrate by effusion cells while the flux of source vapors can be switched on or off by shutters, initiating and terminating growths immediately. In terms of optimization of  $\text{MX}_2$  growths, many of reported literature focused on the discussion of source materials, growth temperature, growth time, substrate type, and carrier gas. While a particular set of growth parameters are optimized for one configuration, others may not be able to reproduce similar results. The main difference comes from the difference of partial pressure, often not discussed or ignored due to the difficulty of quantifying such parameter. Although partial pressure is difficult to optimize, a qualitative approach of studying its effects is still possible. In one of the pioneering work on graphene growths, Li *et al* reported difference of morphology of CVD graphene flakes at various locations on the Cu enclosures<sup>114</sup>. Cu foils were folded into a Cu enclosures and graphene growths were carried out at 1035°C. The gas mixture used for CVD graphene was methane and  $\text{H}_2$ . Li *et al* observed significant larger graphene domains of ~0.5 mm and lower nucleation density on the inside of Cu enclosures. The authors suggested that the difference originates from the lower partial pressure of methane and much lower pressure of undesirable vapor species. The experiment performed by Li *et al* suggests the importance of growth configuration and

not limited to “traditional” parameters such as growth temperature and time. Zhang *et al* also studied the morphology of graphene by placing Cu foils in a vapor trapping tube opened at one end<sup>115</sup>. The authors postulated that gases flow into the small vapor trapping tube would be trapped inside, and therefore the gas mixture ratio and gas flow rate would be different from outside the vapor trapping tube, thus leading to enhanced graphene growths. Graphene growths were carried out at 1000°C with 1 sccm of methane and 12.5 sccm of H<sub>2</sub>. Zhang and coworkers observed continuous graphene film grown outside of trapping tube. Four-lobe, six-lobe graphene flowers, and other morphologies were observed on Cu foils placed inside vapor trapping tube depending on the growth pressure and methane/hydrogen ratio, thus confirming the local environment inside vapor trapping tube affecting the carrier gas concentration and creating an environment that favors large flower-shaped graphene domains. Rümmeli *et al* also studied the effect of vapor trapping tube by comparing growths carried out in a one-end closed vapor trapping tube to a both-end open vapor trapping tube. Graphene growths were conducted at 1030°C for 15 minutes using 10 sccm of CH<sub>4</sub> and 16 sccm of H<sub>2</sub>. The opening of the one-end closed tube was facing downstream during growth. Rümmeli *et al* observed samples placed in a tube (with both end open) in which the gas flow is not restricted by the growth geometry, 1 – 3 layers

graphene are observed on the substrates. In the case of using one-end closed vapor trapping tube, uniform mono- or bilayer graphene was found on the substrates depending on the sample position. These studies highlight the importance of local pressure for 2D materials growths.

In one of the pioneering work for  $\text{MX}_2$  growths, Cong *et al* reported large area monolayer  $\text{WS}_2$  single crystals grown on  $\text{SiO}_2/\text{Si}$  substrates by enhancing the local pressure.<sup>104</sup>  $\text{WO}_3$  powders were sandwiched between  $\text{SiO}_2/\text{Si}$  substrates and subsequently placed in to a one-end open vapor trapping tube together. S powders were also placed in vapor trapping tube but placed further upstream. The growth was carried out at  $750^\circ\text{C}$  for 5 minutes with 100 sccm of high purity Ar gas supplied during the entire growth process. The authors found triangular shaped  $\text{WS}_2$  single crystals up to  $178\ \mu\text{m}$  isolated on the top  $\text{SiO}_2/\text{Si}$  surfaces. The bottom  $\text{SiO}_2/\text{Si}$  substrates, however, majority of grown  $\text{WS}_2$  were multilayers with irregular shapes. The authors attributed this result to the much higher local concentration of  $\text{WO}_3$  powders. In  $\text{MoS}_2$  growths, Özden *et al* studied the morphology and characterized  $\text{MoS}_2$  nanosheets grown with different Mo:S ratio by keeping precursors amount the same but using different growth configurations<sup>116</sup>. In the first configuration,  $\text{MoO}_3$  and S vapors were able to freely travel to the substrates and not hindered. S vapors

were supplied from upstream while  $\text{MoO}_3$  and substrates were placed face up in a quartz boat. In the second setup,  $\text{MoO}_3$  powders were placed in a quartz cylinder that has a height and a diameter of 2 cm. The substrate is placed facing down on covering most of the quartz cylinder, only leaving a small gap for S vapor to enter. In the third configuration,  $\text{SiO}_2/\text{Si}$  substrates are placed facing down on top of  $\text{MoO}_3$  precursor mounted in a quartz boat. The growths were performed at  $700^\circ\text{C}$  and S was kept at  $150^\circ\text{C}$  during the growths.  $\text{MoS}_2$  morphologies ranging from polycrystalline thin film to triangular single crystal monolayers were observed depending on growth geometry. Özden and coworkers concluded that growths with substrates facing down was more favorable to obtain larger single crystal nanosheets because of higher Mo confinement in the growth zone. This experiment also confirms the importance of local partial pressure for 2D  $\text{MX}_2$  growths.

Despite these results, the development for monolayer  $\text{MX}_2$  is not fully explored and well understood. Centimeter scale  $\text{MX}_2$  has proven to be difficult to synthesize due to the fast growth rate. A better understanding of the growth mechanisms and further optimization of the growth process will help us improve towards higher quality and larger-size single crystalline  $\text{MX}_2$  monolayers. Properly designed growth configuration can produce larger single-crystalline monolayers (up to a few hundred of microns) with minimal amount of

source powder, temperature, and time, which helps industries adapt these novel materials and potentially integrate them into modern devices. In this study, the effect of partial pressure of  $\text{MoO}_3$  were examined on the growth of  $\text{MoS}_2$  by employing trapping tubes and other growth geometries. The results for  $\text{MoS}_2$  growth is likely to be applicable to other  $\text{MX}_2$  growths due to the similarity in the growth mechanism.

### **2.5.1 Experiment:**

Figure 2.13 shows a schematic of  $\text{MoS}_2$  growth.  $\text{SiO}_2/\text{Si}$  and Si substrates were cleaned with acetone, isopropyl alcohol, and de-ionized water, then subsequently dried with  $\text{N}_2$ . 5 mg of  $\text{MoO}_3$  powders were evenly spread across Si substrates, and  $\text{SiO}_2/\text{Si}$  substrate were placed face down on top of  $\text{MoO}_3$  powders and Si substrates, forming a sandwich structure. A gap of 0.5mm was left between top and  $\text{MoO}_3$  powders to prevent contamination of  $\text{SiO}_2/\text{Si}$  substrates' surfaces. The substrates and quartz vapor trapping tube were subsequently placed in a 1-inch diameter quartz tube. The  $\text{SiO}_2/\text{Si}$ - $\text{MoO}_3$ -Si sandwich were placed at locations A, B and C as shown in the growth schematic in Fig 2.13, where the partial vapor pressure of source materials was different. At location A, the precursors can react to each other and deposit on substrates unhindered.  $\text{MoO}_3$  vapors are

not confined, leading to low MoO<sub>3</sub>:S ratio. At location B, partial pressure of MoO<sub>3</sub> is increased due to the confinement of vapor trapping tube while the reaction can still take place. At location C, MoO<sub>3</sub>:S ratio is the highest due to maximized MoO<sub>3</sub> partial pressure, but S vapor cannot effectively reach both the substrate and MoO<sub>3</sub>. The length and diameter of the vapor trapping tube was 10 cm and 1 cm respectively. Before each growth, the quartz tube is annealed at 950°C for 1h to eliminate additional deposition caused by leftover S or MoO<sub>3</sub>. The growths were carried out in vacuum ~50Torr with 70 sccm of Ar used during the entire duration of growth. The furnace was heated to 560°C at a rate of 35°C/m first, at which point Sulfur source is heated to various temperatures to study the effect of growth. The furnace temperature was then further heated to 870°C at 15°C/m. The growths were kept at 870°C for 15 minutes before cooldown. At the end of the growth, the furnace temperature was cooled down naturally, and 500 sccm of Ar was used to purge remaining vapors and prevent further deposition.

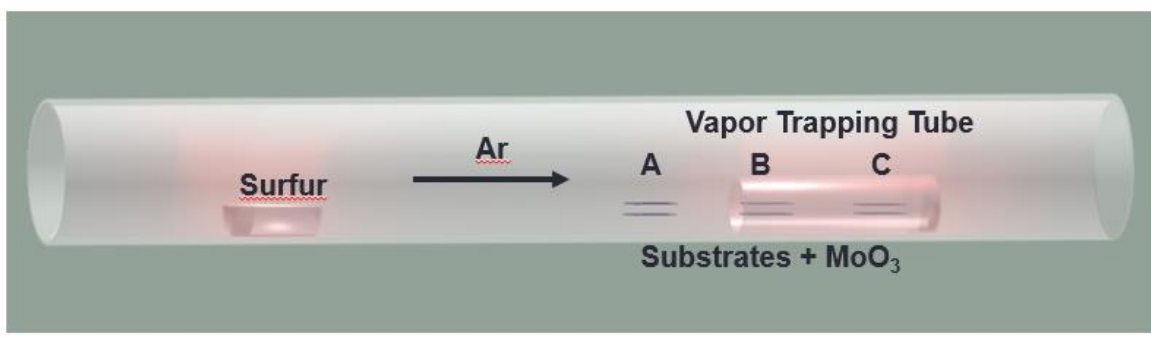


**Figure 2.13.** Schematic of MoS<sub>2</sub> growth setup for local vapor pressure study.

### **2.5.2 Results and Discussion**

As-grown MoS<sub>2</sub> samples were studied under an optical microscope (OM).

The OM images of growths carried out at different sulfur temperatures is shown in Figure 2.14. Figure 2.14a-c shows morphology of MoS<sub>2</sub> growth at 120°C S temperature. At location A, single crystalline monolayer MoS<sub>2</sub> were observed. The average domain size of as-grown MoS<sub>2</sub> monolayers were  $\sim 80\mu\text{m}$  as shown in Figure 2.14a. However, higher concentration of S, which originates from higher S temperatures, results high nucleation density and causes MoS<sub>2</sub> monolayers to join boundaries during growth and creates a partially covered MoS<sub>2</sub> film. At location B and C, polycrystalline MoS<sub>2</sub> film were observed as shown in Figure 2.134 and 2.134 respectively. Due to the contrast between the number

of layers, we were able to determine location B has ~2-3 layers, and location C has 5-6 layers. The confinement of MoO<sub>3</sub> vapors offered by vapor trapping tube has a significant effect on MoS<sub>2</sub> growth. MoS<sub>2</sub> layer thickness seemed to be directly influenced by MoO<sub>3</sub> vapor concentration.

MoS<sub>2</sub> deposition decreases rapidly with lower S temperature, In Figure 2.14d-f (S temperature 115°C) and Figure 2.14g-i (S temperature 110°C), less MoS<sub>2</sub> were deposited compared to the growth carried out at 120°C S temperature. However, a similar trend of MoS<sub>2</sub> morphology was observed in all MoS<sub>2</sub> growths. For example, location C always has more deposition compared to location B and A. The impact of Mo:S vapor ratio also becomes more noticeable at reduced S temperatures. In Figure 2.14d and 2.14g, domain size of MoS<sub>2</sub> single crystal monolayers at location A were ~80 μm and ~10 μm respectively. Figure 2.14j shows partial yellow colored MoO<sub>2</sub> crystals forming on the right-hand side of the image which indicates insufficient S during MoS<sub>2</sub> growth. At 105°C S temperature, the domain size of MoS<sub>2</sub> crystals found at location A (Figure 2.14j) was ~1 μm. However, triangular and hexagonal monolayer single crystal with domains ~50 μm were shown in Figure 2.14k (location B) and 2.14j (location C) due to enhanced MoO<sub>3</sub> local vapor pressure. Overall, using above mentioned growth parameters, vapor trapping tube to

enhance local  $\text{MoO}_3$  partial pressure seems to promote not only lateral growth, but also vertical growth which results in uniform multilayer centimeter sized polycrystalline films.

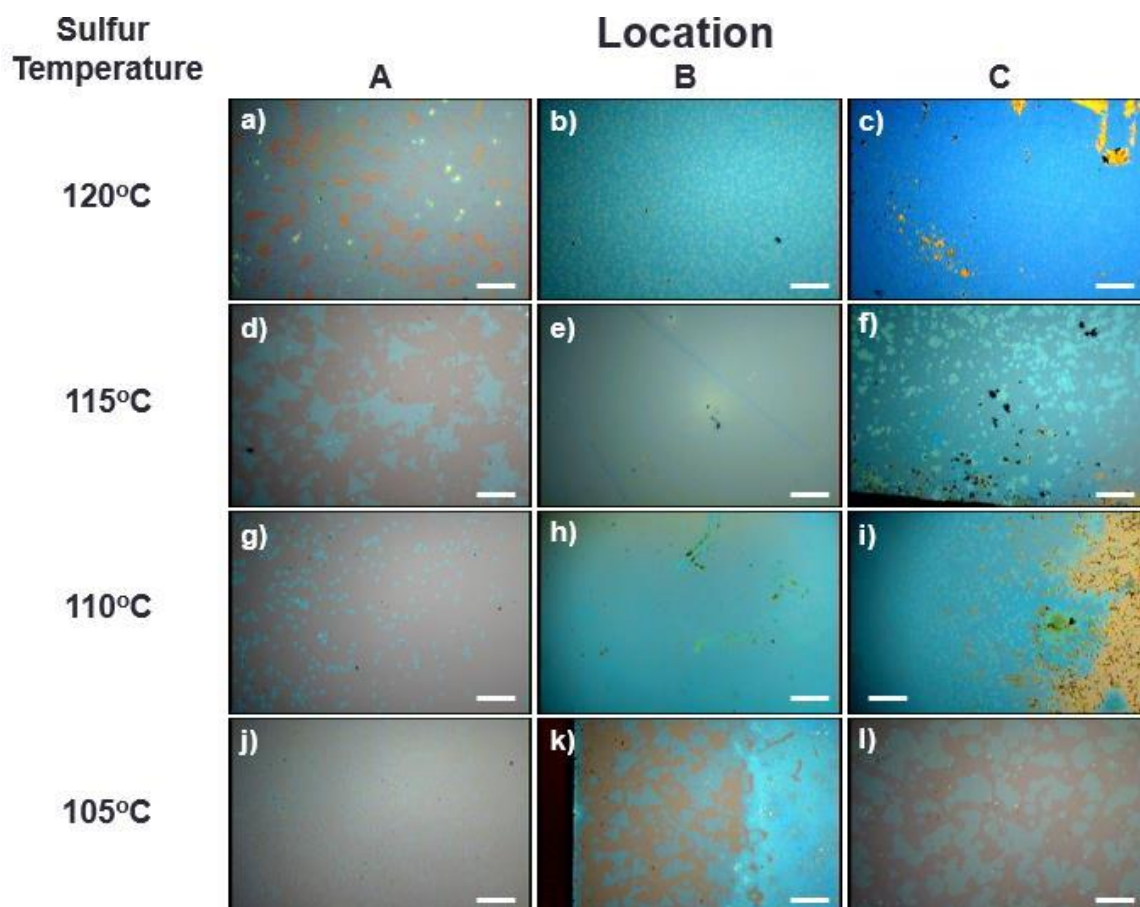


**Figure 2.14.** Morphology of as-grown  $\text{MoS}_2$  under various local pressure. Scalebar is  $100\mu\text{m}$ .

To further confirm the impact of local vapor pressure of  $\text{MoO}_3$ . Another study was performed where the distance between  $\text{MoO}_3$  source powder and  $\text{SiO}_2/\text{Si}$  substrates were varied.  $\text{MoS}_2$  monolayers were grown using previously mentioned method without vapor trapping tube and with reduced growth time of 5 minutes to reduce  $\text{MoS}_2$  domain sizes in order to better observe nucleation densities. Figure 2.15a-d shows the OM images of  $\text{MoS}_2$  crystals where the  $\text{MoO}_3$  precursor to substrate distance of 0, 0.5, 1, and 2 mm respectively. At 0 mm gap, the surface of  $\text{SiO}_2$  substrates have the highest  $\text{MoO}_3$  partial pressure, which results in large area  $\text{MoS}_2$  single crystals as shown in Figure 2.15a. When substrates to precursor distance was increased, as-grown  $\text{MoS}_2$  single crystals were much smaller as shown in Figure 2.15b and c. At this point, noticeable change in nucleation densities were observed. However, once the gap distance was increased to 2 mm, the growth mechanism seemed to shift toward promoting more nucleation points and 3d growth instead of lateral growth. Majority of as-grown  $\text{MoS}_2$  domains were around  $\sim 20 \mu\text{m}$  and bi-layers, with certain areas forming continuous films.

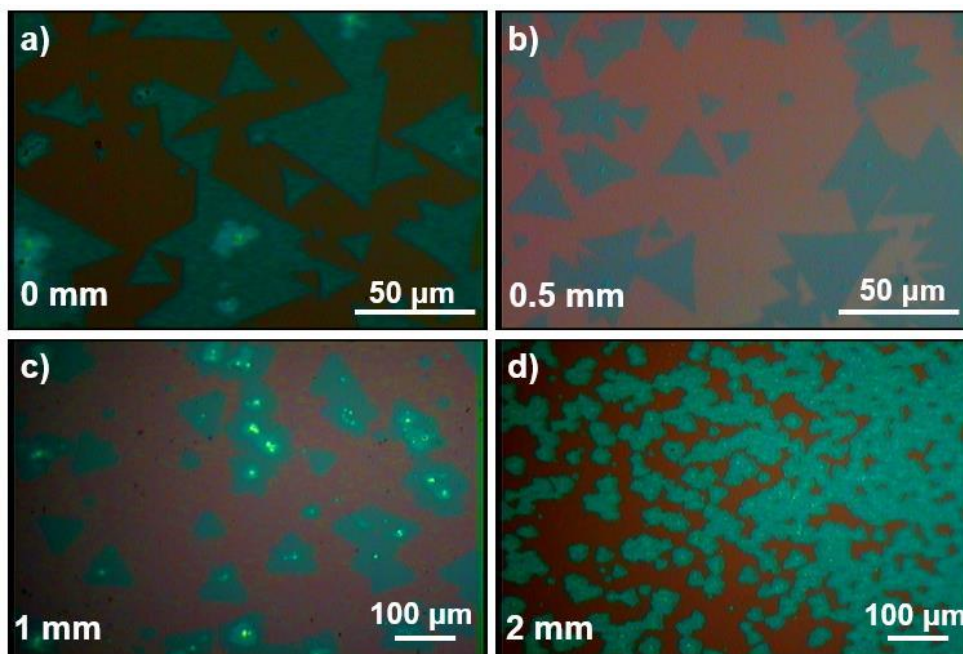


**Figure 2.15.** Effect of source to substrate distance in MoS<sub>2</sub> growths.

## 2.6 Summary

Monolayer MX<sub>2</sub> were grown by CVD method using transition-metal trioxides and chalcogens powders as precursors. Optimization of growth parameters results in large area single crystals MX<sub>2</sub> which can be further studied by characterization or device performance. Figure 2.16a-d shows the largest single crystals monolayers MoS<sub>2</sub>, WS<sub>2</sub>, MoSe<sub>2</sub>, and WSe<sub>2</sub> grown respectively during my research. In addition, by manipulating local vapor pressure, centimeter sized polycrystalline MoS<sub>2</sub> are successfully grown. Even more, we were able to

demonstrate large area MoS<sub>2</sub> single crystals monolayers up to 50 μm at reduced S temperature of 105°C by enhancing local partial pressure of MoO<sub>3</sub> using vapor trapping tube. These results are important as they pave the way for device fabrication and characterization. In the next chapter, CVD grown MX<sub>2</sub> will be characterized through optical and electrical methods to determine their quality.

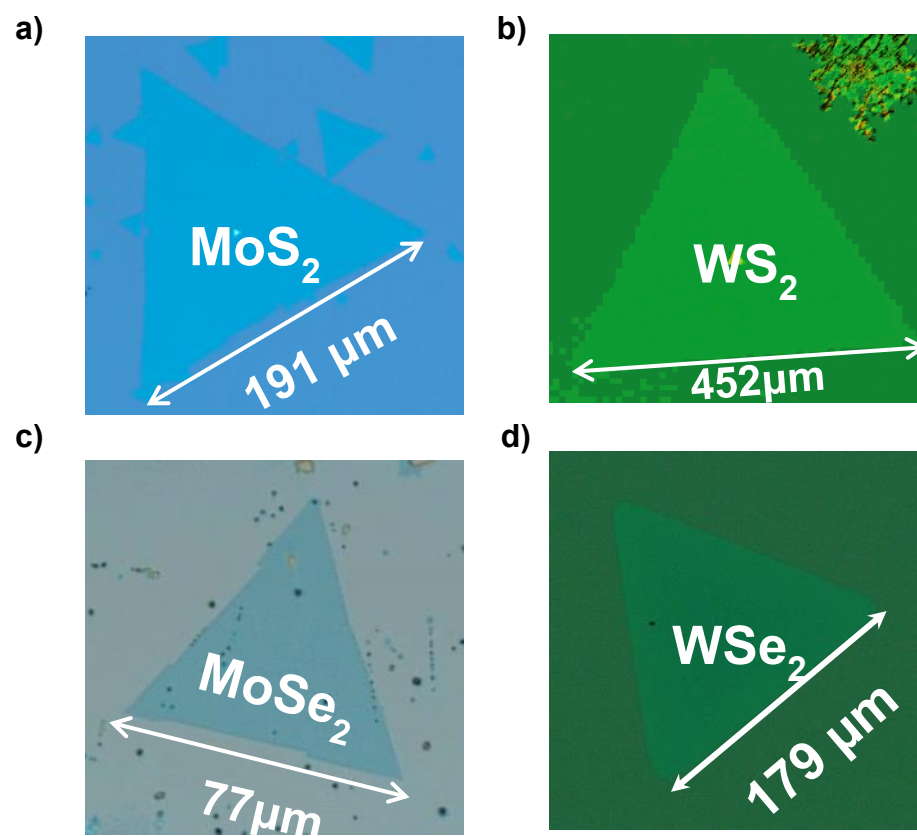


**Figure 2.16.** Largest single crystal  $\text{MX}_2$  monolayers grown after growth optimization. a)  $\text{MoS}_2$ , b)  $\text{WS}_2$ , c)  $\text{MoSe}_2$ , and d)  $\text{WSe}_2$ .

## CHAPTER 3

### CHARACTERIZATION OF TRANSITION-METAL DICHALCOGENIDES

In Chapter 2, large area  $\text{MX}_2$  (M=Mo, W; X = S, Se) monolayers were grown on  $\text{SiO}_2$  coated Si substrates. In this chapter will detail the characterization of as-grown  $\text{MX}_2$  from three main aspects, imaging, optical and electrical characterization. The techniques of characterization will be described and experimental data from different characterization methods will be discussed in each section.

#### **3.1 Imaging of $\text{MX}_2$**

##### **3.1.1 Optical Microscopy of $\text{MX}_2$**

Optical microscope (OM) is one of the most used instruments in scientific studies to observe micro-sized features. As-grown  $\text{MX}_2$  were studied under OM. When  $\text{MX}_2$  is monolayer, all four species appear to be blue-green color under OM.  $\text{MX}_2$  Single crystals are either triangular or hexagonal in shape, which is directly related to precursor ratio during the growth. Figure 3.1a shows an OM image of monolayer, bi-layer and tri-layer single crystal  $\text{WS}_2$ . Color contrast can be observed between the layer thickness. The color

of  $\text{WS}_2$  becomes brighter as the thickness of  $\text{MX}_2$  increases. Typically, blue-green colored area represents thickness of  $n < 10$ , and yellowed colored  $\text{MX}_2$  have number of layers  $n > 10$  as shown in Figure 3.1b. The layers can be readily identified using optical contrasts makes optical microscopes one of the most powerful tools in 2D materials research.

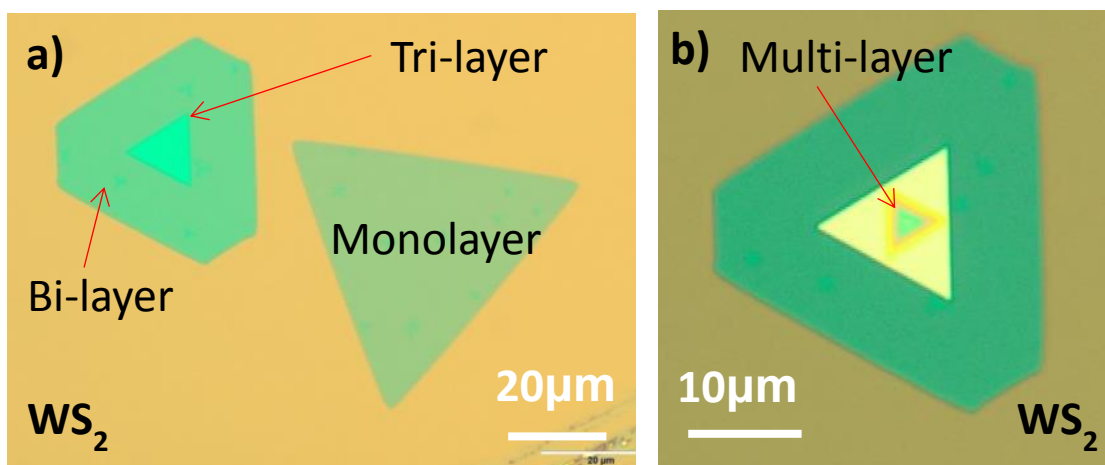


**Figure 3.1.** Optical microscope image of CVD grown  $\text{WS}_2$ . a) monolayer, bi-layer and tri-layer  $\text{WS}_2$ , b) multi-layer  $\text{WS}_2$ .

### 3.1.2 Scanning Electron Microscopy of $\text{MX}_2$

Despite the usefulness of optical microscopes, they typically have resolution

of  $\sim 1 \mu\text{m}$  due to diffraction limit. When the features of an object are smaller than diffraction limit of visible light, OM is no longer effective in identifying those features. Scanning electron microscope (SEM) uses electrons' reflection to image an object. The resolution of SEM is much better than OM is the result of the smaller wavelength of electron beams. The energy of electron beams typically ranges from a few kV to tens of kV. SEM was a useful instrument during initial optimization of growth parameters as the grown nanosheets had domain sizes less than  $1 \mu\text{m}$ . The SEM images of  $\text{MoS}_2$ ,  $\text{WS}_2$ ,  $\text{MoSe}_2$ , and  $\text{WSe}_2$  were taken using Tescan Vega 3 system and the images are shown in Figure 3.2a, 3.2b 3.2c and 3.2d respectively. The SEM images of  $\text{MX}_2$  shows good contrast between  $\text{SiO}_2$  surface and as-grown nanosheets. However, the contrast between individual layers were not clear and it is necessary to characterize using additional tools.

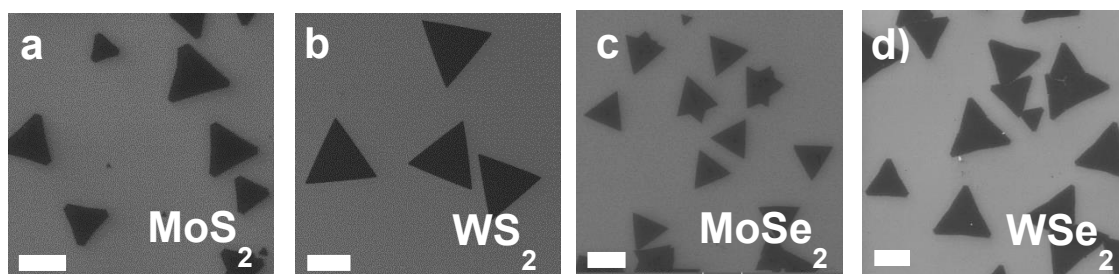


**Figure 3.2.** Scanning electron microscope images of MX<sub>2</sub>. a) MoS<sub>2</sub>, b) WS<sub>2</sub>, c) MoSe<sub>2</sub>, and d) WSe<sub>2</sub>. The scale bars in the images are 20 μm, 100 μm, 20 μm, and 20 μm from left to right.

### **3.1.3 Atomic Force Microscopy of MX<sub>2</sub>**

As-grown MX<sub>2</sub> were studied under atomic force microscopy (AFM) under Park XE-7 system. Figure 3.3a shows an OM image of as-grown MoS<sub>2</sub> monolayer. Figure 3.3b shows the AFM image of the same MoS<sub>2</sub> monolayer shown in Fig.3.3a. The height profile of as-grown MoS<sub>2</sub> along the blue line in Figure 3.3b were shown in Figure 3.3c. The height of MoS<sub>2</sub> is ~1 nm, which is consistent with monolayer thickness of MoS<sub>2</sub>.

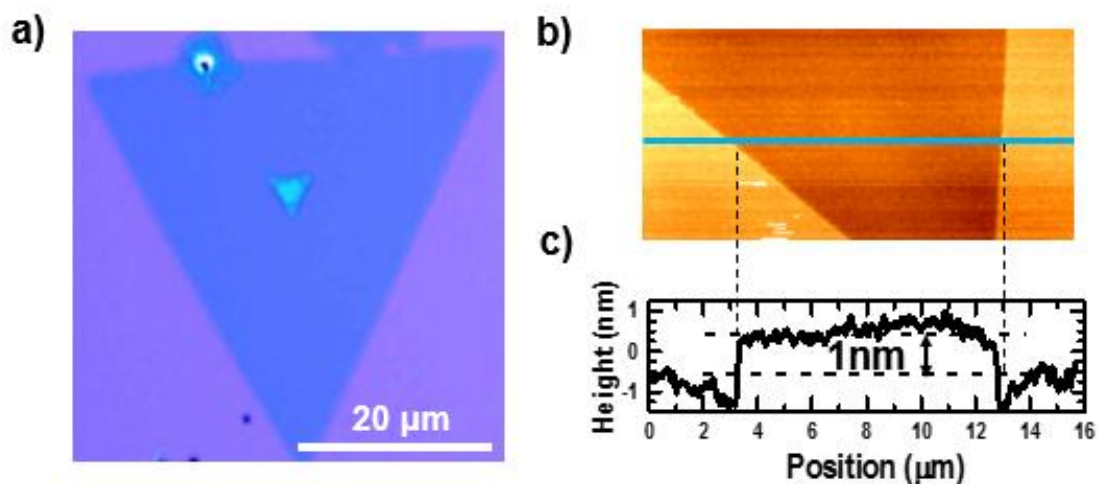


**Figure 3.3.** Atomic force microscopy of monolayer MoS<sub>2</sub>. a) Optical microscope image of as-grown monolayer MoS<sub>2</sub>. b) Atomic force microscopy of MoS<sub>2</sub> shown in a). c) Height profile of MoS<sub>2</sub> monolayer along the blue line in b).

## 3.2 Optical Characterization of MX<sub>2</sub>

### 3.2.1 Raman Spectrum of MX<sub>2</sub>

Raman spectroscopy is a commonly used method to identify materials by observing vibrational and rotational modes in molecules or crystals excited by a laser. When a molecule is scattered by photons, a minority of the scattering processes are inelastic, which results the scattered photons having different wavelength from incident light. This phenomenon is called Raman scattering. Generally, Raman spectroscopy is used to identify materials and crystal structure.

### Raman Spectra of MoS<sub>2</sub>

As grown MoS<sub>2</sub> nanosheets are studied under Renishaw inVia confocal Raman microscope. The Raman microscope has a spot size of  $\sim 1 \mu\text{m}$  and resolution of  $\sim 1.5 \text{ cm}^{-1}$ . The grating used in the measurements was 1200 l/mm. The Raman spectrum of MoS<sub>2</sub> has two prominent peaks E<sub>2g</sub><sup>1</sup> and A<sub>g</sub><sup>1</sup>, corresponding to the in-plane Mo – S and out-of-plane Mo – S phonon mode.<sup>117-118</sup> The E<sub>2g</sub><sup>1</sup> and A<sub>g</sub><sup>1</sup> peaks of MoS<sub>2</sub> are located at  $\sim 385 \text{ cm}^{-1}$ , and  $\sim 405 \text{ cm}^{-1}$  respectively as shown in Figure 3.4a. The difference of the two peaks exhibits dependence on the thickness of the nanosheets. In monolayer MoS<sub>2</sub>, the difference of the two peaks is  $\sim 19 \text{ cm}^{-1}$ , in few layered MoS<sub>2</sub>, the difference between the two peaks increases to  $24 \text{ cm}^{-1}$ , and in bulk MoS<sub>2</sub> the difference becomes  $27 \text{ cm}^{-1}$  as shown in Figure 3.4b. This phenomenon allows Raman spectroscopy to be used to identify the number of layers in MoS<sub>2</sub> nanosheets. These results are in good agreement with CVD grown MoS<sub>2</sub> reported elsewhere.<sup>118-122</sup> Next, a single crystal monolayer MoS<sub>2</sub> shown in Figure 3.4c is examined at different location 1 – 6, and their respective Raman spectra shown in Figure 3.5d. The positions of E<sub>2g</sub><sup>1</sup> and A<sub>g</sub><sup>1</sup> peaks are consistent across all positions indicating uniform monolayer. E<sub>2g</sub><sup>1</sup> and A<sub>g</sub><sup>1</sup> peaks of the same CVD grown single crystal monolayer MoS<sub>2</sub> are mapped in Figure 3.4e and 3.4f. The intensity of peaks is represented by color

scale bar where white-yellow color indicates stronger emission and black-red color indicates low or zero emission. The triangular shape and uniform color of the single crystal MoS<sub>2</sub> can be clearly identified in both E<sup>1</sup><sub>2g</sub> and A<sup>1</sup><sub>g</sub> peaks mapping, which reveals good uniformity of as-grown MoS<sub>2</sub> nanosheet.

### Raman Spectra of MoSe<sub>2</sub>

Figure 3.5a shows the Raman spectra of MoSe<sub>2</sub> measured using 514 nm laser with a spot size of ~ 2 μm. The optical microscope image of CVD grown single crystal monolayer MoSe<sub>2</sub> is shown as inset in Figure 3.5a. E<sup>1</sup><sub>2g</sub> peak is suppressed under 514 nm laser and a single peak of A<sup>1</sup><sub>g</sub> is located at ~240 cm<sup>-1</sup> as shown in Figure 3.5b. These results are in good agreement with pristine MoSe<sub>2</sub> and other CVD grown MoSe<sub>2</sub> nanosheets.<sup>105, 121, 123-125</sup> The Raman spectra of the same MoSe<sub>2</sub> single crystal were subsequently mapped across nearby area and shown in Figure 3.5c, indicating good uniformity.

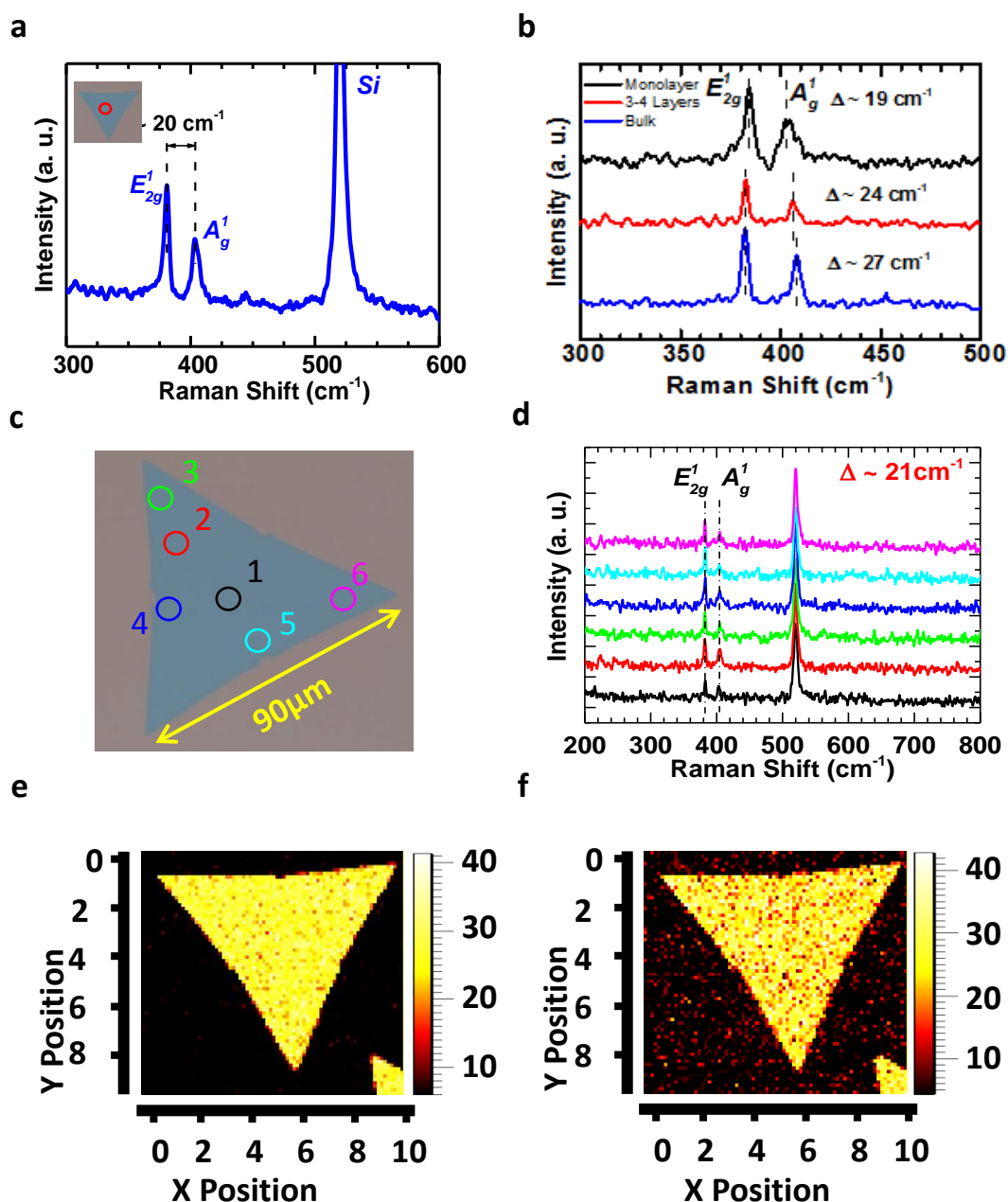


**Figure 3.4.** Raman spectra of MoS<sub>2</sub>. a) Raman spectrum of monolayer MoS<sub>2</sub>. b) Raman spectra of monolayer, few-layer, and multi-layer MoS<sub>2</sub>. The difference of  $E_{2g}^1$  and  $A_g^1$  peaks shows dependency on MoS<sub>2</sub> thickness. c) Optical microscope image of CVD grown single crystal. d) Raman spectra of monolayer MoS<sub>2</sub> at various positions shown in c. e)  $E_{2g}^1$  peak mapping of monolayer MoS<sub>2</sub> at various positions shown in c. f)  $A_g^1$  peak mapping of monolayer MoS<sub>2</sub> shown in c.

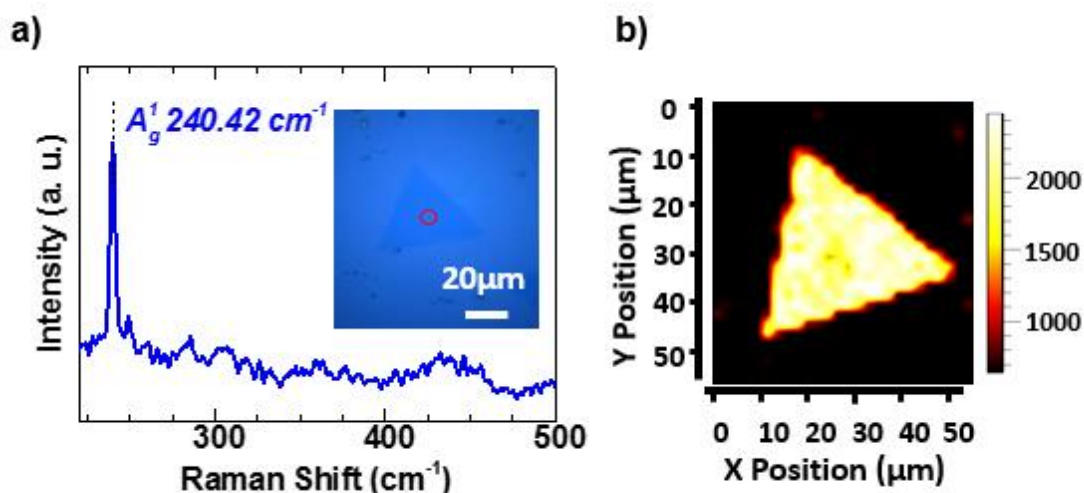


**Figure 3.5.** Raman spectra of monolayer MoSe<sub>2</sub>. a) Raman spectrum of a single crystal MoSe<sub>2</sub> monolayer nanosheet. Inset shows the MoSe<sub>2</sub> which the Raman spectrum is taken from. b) Raman mapping image of MoSe<sub>2</sub> shown in a).

### Raman Spectra of WS<sub>2</sub>

The Raman spectrum of WS<sub>2</sub> is shown in Figure 3.6a. Under 514 nm laser excitation, two prominent peaks were observed at 354.4 cm<sup>-1</sup>, which is an overlap of 2LA(M) peak and E<sup>1</sup><sub>2g</sub> peak, and A<sub>1g</sub> peak is located at 417.7 cm<sup>-1</sup>.<sup>126</sup> The inset of Figure 3.6a shows the OM image of the WS<sub>2</sub> nanosheet being studied, and the red circle represents the laser spot location. The laser used for Raman spectroscopy was subsequently changed to 633nm to suppress 2LA(M) peak. Figure 3.6b shows the Raman spectra of monolayer

and multi-layer WS<sub>2</sub> single crystal excited by 633 nm laser. The distance between the two peaks was also layer dependent. The wave number differences between E<sup>1</sup><sub>2g</sub> peak and A<sub>1g</sub> peaks are ~62.1 cm<sup>-1</sup> for monolayer WS<sub>2</sub> and 64.4 cm<sup>-1</sup> for multi-layer WS<sub>2</sub> as shown in Figure 3.6b. The two peaks of monolayer WS<sub>2</sub>, E<sup>1</sup><sub>2g</sub> peak and A<sub>1g</sub>, were subsequently mapped and shown in Figure 3.6c and 3.6d. The two mapping images shows good uniformity in as-grown WS<sub>2</sub> monolayers.

#### Raman Spectra of WSe<sub>2</sub>

Raman spectrum of monolayer WSe<sub>2</sub> was studied using similar approach mentioned previously. Similar to MoSe<sub>2</sub>, the Raman spectrum of WSe<sub>2</sub> shown in Figure 3.7 also has a single peak A<sub>1g</sub> located at 248.44 cm<sup>-1</sup>. This result is also in good agreement with report values from literature.<sup>106, 121, 127</sup>

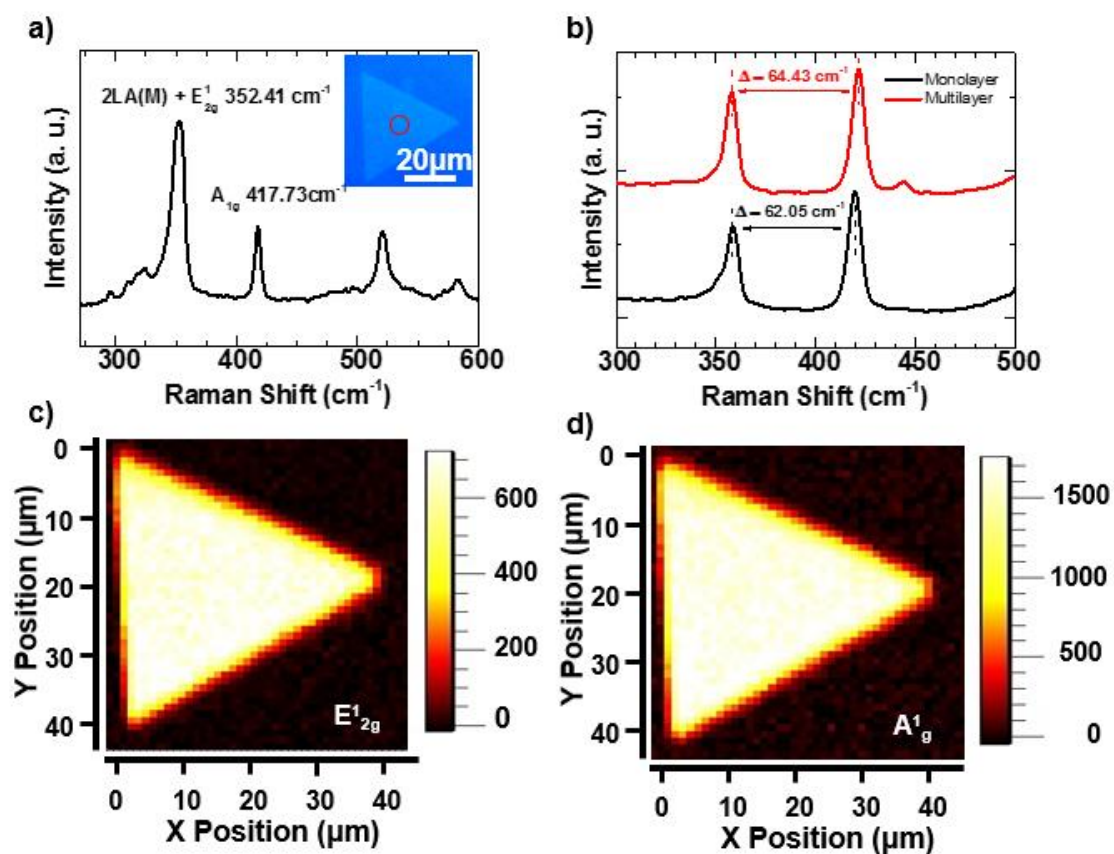


**Figure 3.6.** Raman spectra of WS<sub>2</sub>. a) Raman spectra of WS<sub>2</sub> monolayer. Inset shows the optical microscope image of characterized WS<sub>2</sub>. b) Layer dependence in Raman spectra of WS<sub>2</sub>. c)  $E_{2g}^1$  mapping of single crystal WS<sub>2</sub> monolayer nanosheet. d)  $A_{1g}$  mapping of single crystal WS<sub>2</sub> monolayer nanosheet.

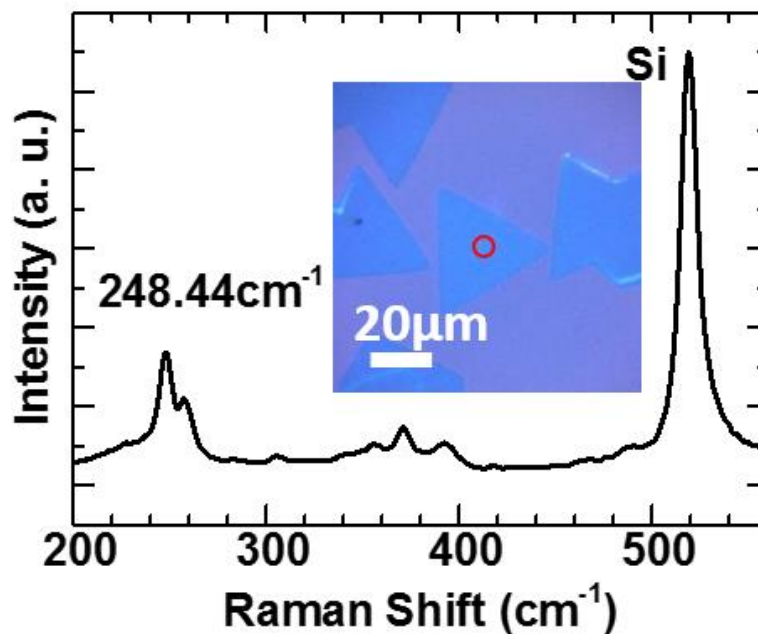


**Figure 3.7.** Raman spectra of monolayer WSe<sub>2</sub>.

### **3.2.2 Photoluminescence of MX<sub>2</sub>**

Photoluminescence (PL) is one of the most powerful tools in material characterization, in particular to identify the bandgap of a direct semiconductor. The quality of the crystals can be generally characterized by the full width half maximum of the peaks. Furthermore, other parameters such as doping levels and crystallinity, can sometimes be estimated from PL spectra.

#### **Photoluminescence Spectra of MoS<sub>2</sub>**

The PL spectrum of MoS<sub>2</sub> was measured by Renishaw inVia confocal Raman

microscope using a 514 nm laser and 1800 l/mm grating. Monolayer MoS<sub>2</sub> has a strong single PL peak at ~1.8eV as shown in Figure 3.8a. The inset shows CVD grown monolayer single crystal MoS<sub>2</sub> which the PL characterization was performed on. The circle represents the location of the laser spot used to excite monolayer MoS<sub>2</sub>. As previously discussed in Chapter 1, monolayer MoS<sub>2</sub> are direct semiconductors materials, and becomes indirect semiconductors when the number of layer exceeds two.<sup>94, 128-130</sup> The layer dependence PL spectra of MoS<sub>2</sub> is shown in Figure 3.8b. CVD grown monolayer, bi-layer, tri-layer, multi-layer (n ~10), and bulk (n ~ 50) MoS<sub>2</sub> were characterized under PL spectroscopy. The intensities of the PL were enhanced by 10 times due to the weak signal except for monolayers. Monolayer MoS<sub>2</sub> exhibit the strongest PL emission, which further confirms the direct bandgap nature of monolayer MoS<sub>2</sub>. In bi-layer and tri-layer MoS<sub>2</sub>, a second peak from B exciton is observable at ~1.95eV. The mapping of PL spectra of CVD-MoS<sub>2</sub> is shown in Figure 3.8c. Uniform intensity were observed on across the entire nanosheet, indicating good uniformity of CVD growth process.

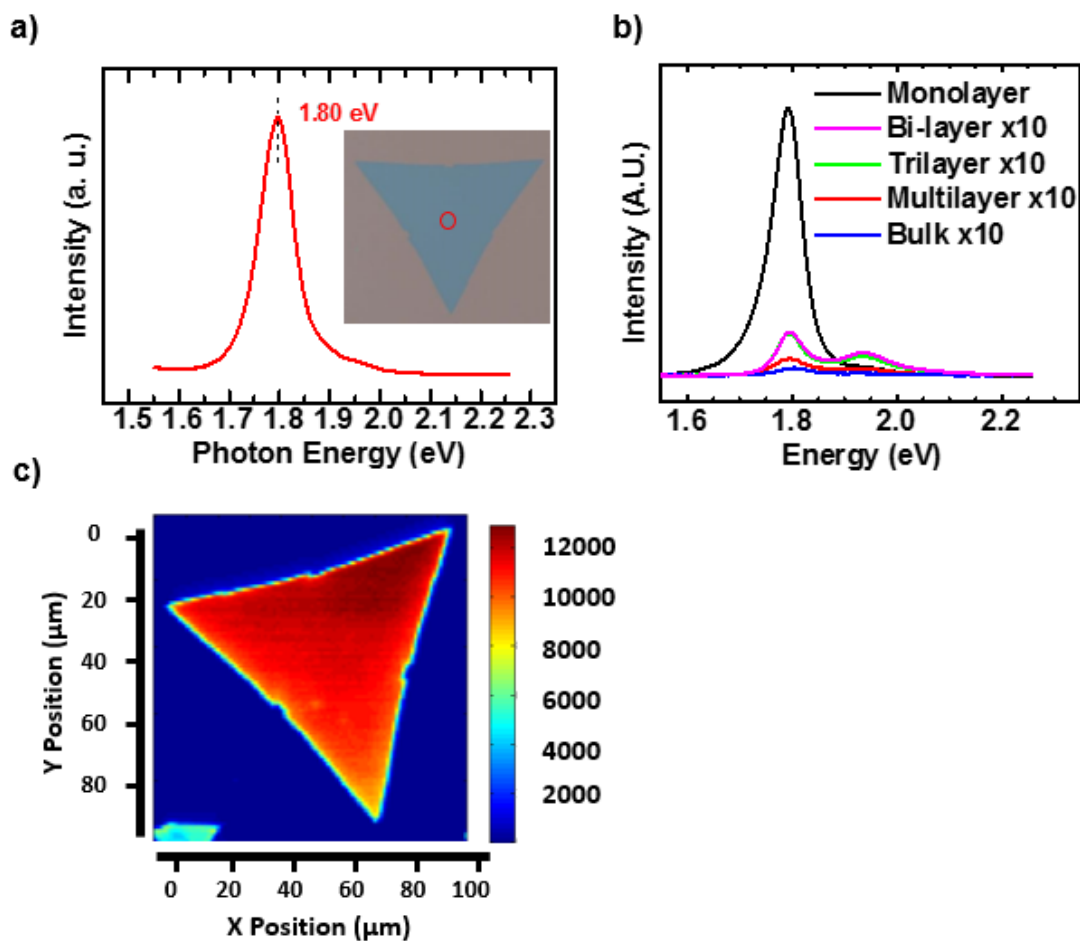


**Figure 3.8.** Photoluminescence spectra of CVD-MoS<sub>2</sub>. a) PL spectra of monolayer MoS<sub>2</sub>. Inset shows an optical microscope image of as-grown MoS<sub>2</sub> on SiO<sub>2</sub> substrates, in which the PL spectroscopy was performed on. b) Layer dependent PL spectra of CVD-MoS<sub>2</sub>. c) PL mapping of CVD-MoS<sub>2</sub> at 1.8 eV.

### Photoluminescence Spectra of MoSe<sub>2</sub>

PL spectroscopy of monolayer MoSe<sub>2</sub> were carried out in the same setup used

for MoS<sub>2</sub> described before. Figure 3.9a shows the PL spectrum of a CVD grown MoSe<sub>2</sub> at room temperature. The OM image of the MoSe<sub>2</sub> monolayer is shown in the inset of Figure 3.9a. PL spectrum shows a single emission at 1.52eV, consistent with the band gap of MoSe<sub>2</sub> monolayers reported elsewhere.<sup>105, 130-131</sup> Additionally, the PL mapping reveals the uniform layers of CVD-grown MoSe<sub>2</sub>.

#### Photoluminescence Spectra of WS<sub>2</sub>

The PL spectra of CVD grown WS<sub>2</sub> is shown in Figure 3.10a. The strong PL emission at 1.96 eV is consistent with other reports<sup>58, 88, 117, 126, 132</sup>, indicating its monolayer nature. The mapping of the PL peaks was subsequently carried out and shown in Figure 3.10b. The dark spots in the PL mapping point out nucleation points and hints at the formation of a second layer. The bilayer nucleation points appear to be scattered across the entire WS<sub>2</sub> single crystal. This interesting phenomenon gives insight on the growth mechanics of CVD WS<sub>2</sub>, as well as future growth strategies to optimize single crystal WS<sub>2</sub> monolayers. In addition, monolayer WS<sub>2</sub> has the strongest PL emission out of all four materials of MX<sub>2</sub> studied under same laser intensity and other optical settings. The FWHM of WS<sub>2</sub> PL spectrum also reflects the high quality of grown WS<sub>2</sub> single crystal.

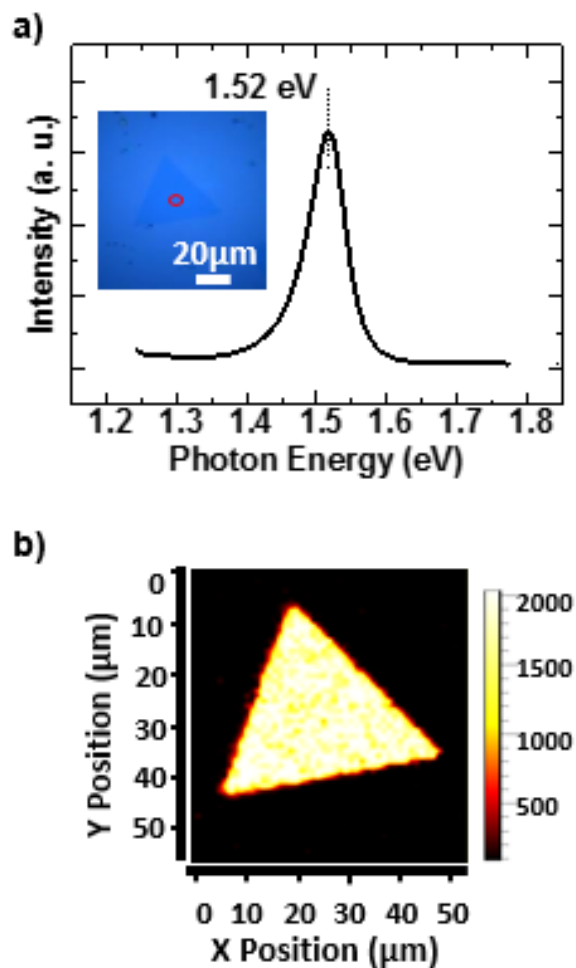


**Figure 3.9.** Photoluminescence spectra of CVD-MoSe<sub>2</sub>. a) PL spectra of CVD grown monolayer MoSe<sub>2</sub>. Inset shows an optical microscope image of as-grown MoSe<sub>2</sub> on SiO<sub>2</sub> substrates, in which the PL spectroscopy was performed on. b) PL mapping of CVD-MoSe<sub>2</sub> at 1.52 eV.

### Photoluminescence Spectra of WSe<sub>2</sub>

The PL of monolayer WSe<sub>2</sub> was obtained using the same setup described before.

Monolayer WSe<sub>2</sub> have a single peak located at 1.58 eV as shown in Figure 3.11. The inset of Figure 3.11 shows an OM image of CVD-WSe<sub>2</sub> monolayers. The red circle indicates the laser spot location. The strong emission of WSe<sub>2</sub> monolayers also confirmed the monolayer nature of CVD process and consistent with values reported by others.<sup>106-107, 133</sup>

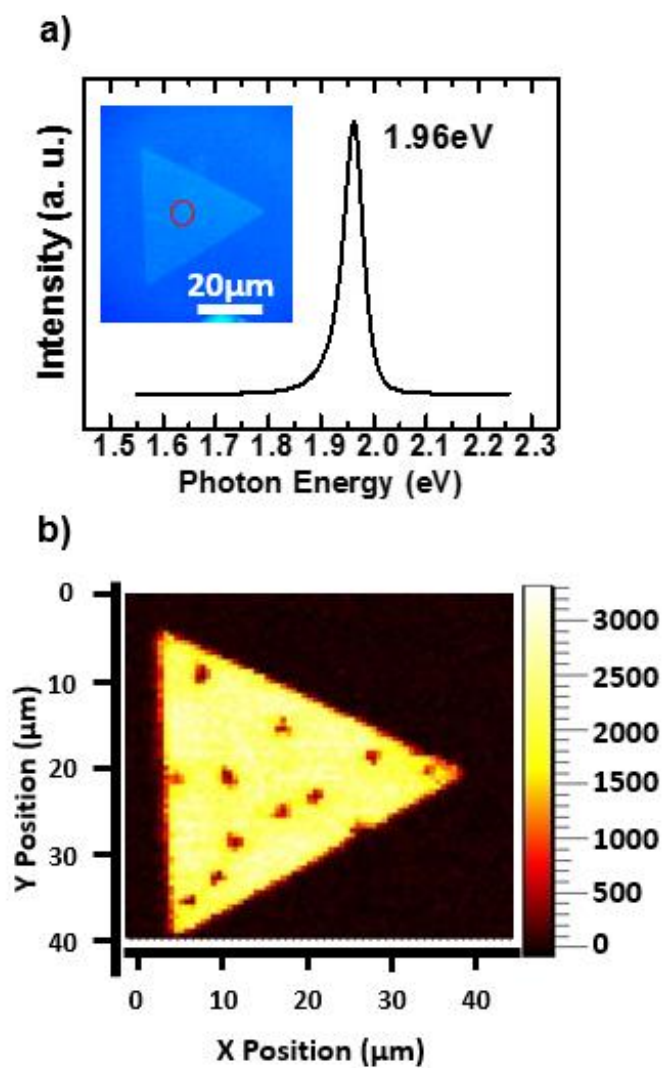


**Figure 3.10.** Photoluminescence of monolayer CVD-WS<sub>2</sub>. a) PL spectra of CVD grown monolayer WS<sub>2</sub>. Inset shows an optical microscope image of as-grown WS<sub>2</sub> on SiO<sub>2</sub> substrates, in which the PL spectroscopy was performed on. b) PL mapping of CVD-WS<sub>2</sub> at 1.96 eV shown in the insert of Fig 3.10a.

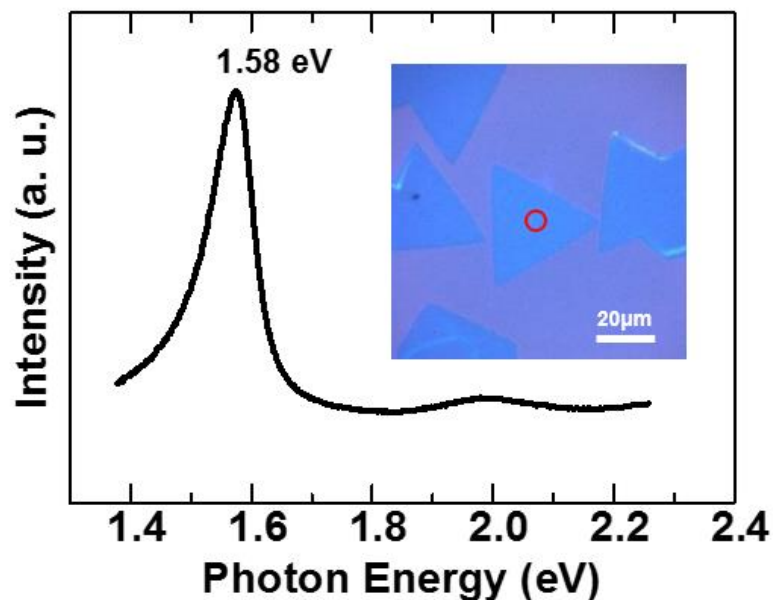


**Figure 3.11.** Photoluminescence spectra of CVD grown WSe<sub>2</sub>.

### 3.4 Electrical Characterization of MX<sub>2</sub>

Due to the honey-comb lattice structure and the two-dimensional confinement of electron movement, graphene has exhibited exceptional electrical transport properties. Graphene field effect transistors (FET) have been at the center of electronics research in recent years, with field-mobility measured up to  $10^5 \text{ cm}^2\text{V}^{-1}\text{s}^{-1}$ .<sup>38, 134-136</sup> However, due to the lack of a bandgap, the on-off ratio of graphene transistors has been a major drawback in graphene FET. MX<sub>2</sub> are direct semiconductors that has a bandgap  $\sim 1.5 - 1.9 \text{ eV}$ . The

semiconducting nature of  $\text{MX}_2$  allows the carriers in FET channels to be further modulated by gate bias. Additionally, the 2D confinement in monolayer  $\text{MX}_2$  also shows superior transport properties up to a few hundreds of  $\text{cm}^2\text{V}^{-1}\text{s}^{-1}$ .<sup>108, 137-138</sup> However, the quality of CVD grown  $\text{MX}_2$  can vary tremendously due to the growth parameters. For example, nearly all of the CVD-grown  $\text{MoS}_2$  reported so far have been n-type due to S vacancies.<sup>65, 67, 139-141</sup> Furthermore, the performance of  $\text{MX}_2$  FETs are heavily impacted by contact resistance. For these reasons, the electrical transport properties of CVD- $\text{MX}_2$  should be investigated. In this section, the fabrication of  $\text{MoS}_2$  FET and Hall-Bar device is explained first. Then the strategies used to reduce contact resistance are elaborated, and the transport properties of CVD grown  $\text{MX}_2$  are discussed.

### **3.4.1 Experiments**

#### **Fabrication of $\text{MX}_2$ FET/Hall-Bar Devices:**

As-grown  $\text{MX}_2$  monolayers were transferred to fresh  $\text{SiO}_2/\text{Si}$  substrates due to the leaky insulating layer damaged by high temperature during growth. As-grown  $\text{MX}_2$  monolayers were spin coated with Microchem PMMA A5.5 at 3000 rpm then baked at  $180^\circ\text{C}$  to remove the solvents. Then, the spin coated samples were dip into 10% HF

solution for 20 minutes to etch away the SiO<sub>2</sub> layer. The PMMA-coated-MX<sub>2</sub>-monolayers were subsequently transferred to fresh degenerately doped Si substrates coated with 300 nm thermal oxide, followed by baking at 100°C for 20 minutes to remove water molecules. The highly doped Si substrates will function as the back gate of the transistor. Finally, the PMMA was removed with acetone, rinsed by de-ionized (DI) water, and dried by N<sub>2</sub> gun.

After transfer, an etch mask with Hall-bar geometry was patterned on transferred MX<sub>2</sub>. Shipley1811 photoresist were spun-coated at 3000 rpm for 30 s, then soft-baked at 115°C for 60 s. The thickness for the photoresist is 1.3 μm. The exposure for the Hall-bar pattern was carried out in Microtech LW405 laser pattern generator (direct-write photolithography tool). After exposure, the substrates were developed in diluted Microchem 351 developer (351: H<sub>2</sub>O = 1:3) solution for 30 s, then rinsed by DI water. The etching is carried out in March CS-1701 plasma system under 22 sccm of O<sub>2</sub>, 20 W of power, and 160mTorr for 20s – 120s depending on the material. After dry etching, the substrates were rinsed with acetone, isopropyl alcohol (IPA), and DI water, and dried by N<sub>2</sub> gun.

The contact of the FET/Hall-bar devices were subsequently formed on MX<sub>2</sub>. Shipley1811 photoresist were spun-coated at 3000 rpm for 30 s, then soft-baked at 115°C for 60 s. The exposure for the contacts was also carried out in Microtech LW405 laser

pattern generator. After development, the metal deposition is carried out in an e-beam evaporator system with a base pressure of  $1 \times 10^{-8}$  Torr. Ti(10nm)/Au(50nm), Ni(50nm), Au(50nm), and Pd(50nm) were used for MoS<sub>2</sub>, MoSe<sub>2</sub>, WS<sub>2</sub> and WSe<sub>2</sub> contacts. Liftoff process is accomplished by immersing the substrates under acetone for 20 m. The fabrication process is shown in Figure 3.12.

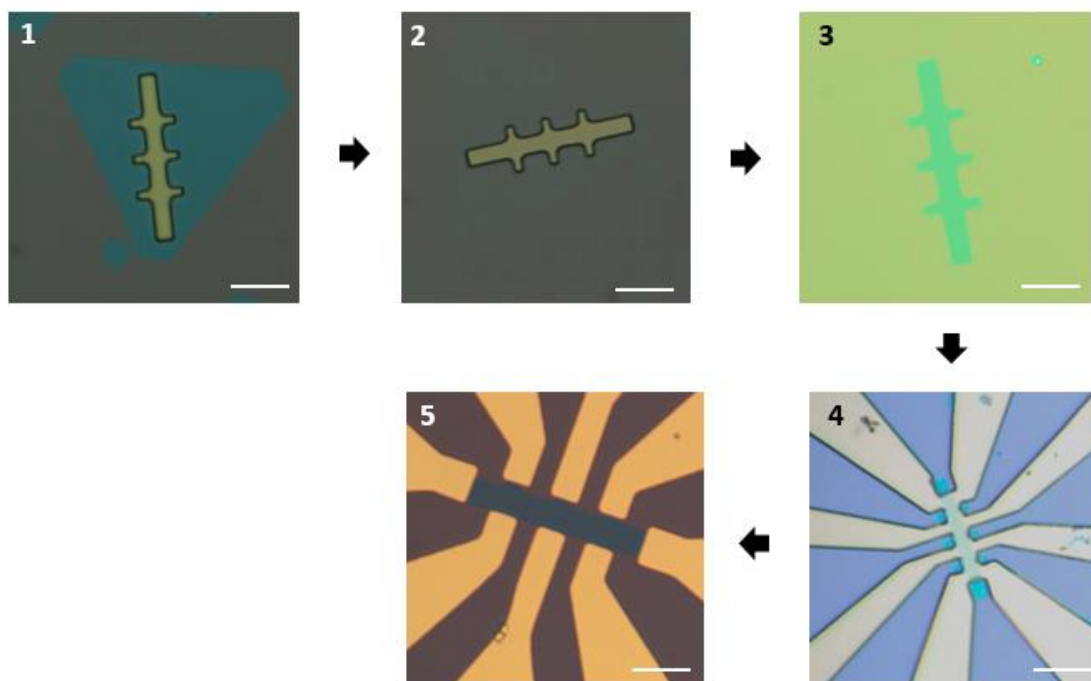


**Figure 3.12.** Fabrication process of MX<sub>2</sub> FET/Hall-Bar devices. The scale bars in the images are 20  $\mu\text{m}$ .

### Measurement

The back-gated  $\text{MX}_2$  devices were measured using a conventional probe station. Before measurements, the backsides of Si substrates were scratched to expose the highly conductive degenerately doped Si. Silver paste and indium were applied to form the connection between probe and the gate as shown in Figure 3.13a. The back-gate voltage is supplied via Keithley 6487 pico-ammeter. The source-drain  $I$ - $V$  is measured by Keithley 2400 source meter as shown in Figure 3.13b. For Hall effect measurements, The fabricated devices were wire-bonded (Westbond 7476D) to a Chelsea Tech. chip carrier then mounted to a home-built cryogenic measurement system equipped with Lakeshore EM4 electromagnet, Lakeshore 643 electromagnet power supply, and Lakeshore 475 gauss meter. Keithley 6221 AC/DC current source meter and 2182A nano-voltmeter were used to supply longitudinal current and measure the voltage drop across individual pairs of transverse contacts respectively.

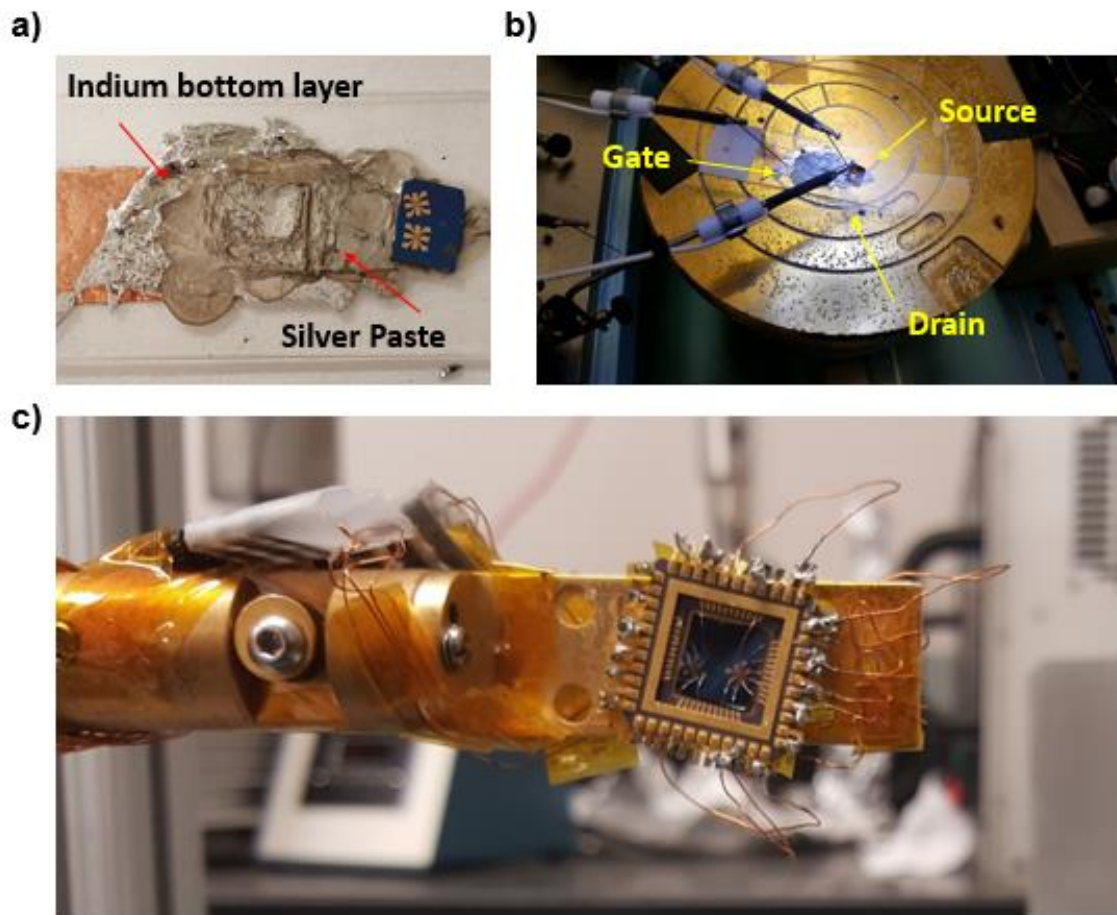


**Figure 3.13.** Electrical measurement of MX<sub>2</sub> FET and Hall effect.

### **3.4.2 Contact Resistance**

Despite recent advances in MX<sub>2</sub> research, one of the critical problem lies with the contact resistance. Often times, the performance of MX<sub>2</sub> FET devices were severely hindered by the presence of high Schottky barrier at the MX<sub>2</sub>/Metal junction. In

semiconductor-metal junction theory, Ohmic contact can be formed with low work function metals in n-type semiconductors. For, p-type semiconductors, a high work function metal is required. Das *et al* reported high performance MoS<sub>2</sub> FET using Sc as contact.<sup>141</sup> However, the results presented in Das *et al*'s work can be misleading as the contact resistance and the formation of Ohmic contact can also be attributed to a variety of reasons such as interface oxidation<sup>142</sup>, interface chemical reaction<sup>143-144</sup>, and S vacancies<sup>145-146</sup>. Even under ideal conditions, the intrinsic contact resistance for MX<sub>2</sub> is still far away from the requirements of International Technology Roadmap for Semiconductors (ITRS)<sup>147</sup>. Currently, the strategies to reduce contact resistance includes molecular doping<sup>49, 88</sup> and using graphene as contacts<sup>148</sup>.

During the initial optimization process of fabrication, the source-drain  $I$ - $V$  relationship of MX<sub>2</sub> FETs were often non-linear. Figure 3.14a shows an example of Schottky junction observed in a fabricated MoS<sub>2</sub> FET. The strong presence of Schottky barrier heavily restricted the current flow of MX<sub>2</sub> FETs, and the  $I$ - $V$  does not improve with any annealing. The results point towards Fermi-level pinning caused by S vacancies for MoS<sub>2</sub> and WS<sub>2</sub>, and Se vacancies in MoSe<sub>2</sub> and WSe<sub>2</sub>. To improve the chalcogen deficiency in as-grown MX<sub>2</sub>, in situ sulfur or selenium annealing were performed after each growth. Afterwards,

the  $I$ - $V$ s of FET improved dramatically and Ohmic junctions were achieved indicated by the linearity. Figure 3.14b shows the gating measurements of an as-fabricated monolayer MoS<sub>2</sub> FET using in-situ S annealed MoS<sub>2</sub>. The FET shows n-type behavior. However, the FET does not have good gate modulation. The on-off ratio of the FET was  $\sim 10^2$ . The field mobility extracted from the  $V_g$ - $I_{ds}$  reveals the FET has field mobility less than  $0.01 \text{ cm}^2\text{V}^{-1}\text{s}^{-1}$ . Although significant improvements were observed, water molecules, PMMA, and photoresist residue during the fabrication process can still have a substantial impact on the performance of MX<sub>2</sub> FETs. Post-fabrication annealing was introduced to remove residues from fabrication process. The devices were annealed in a vacuum chamber at 200°C with 50 sccm of Ar flow for 2 h. Figure 3.14c shows the three-terminal measurements of the MoS<sub>2</sub> FET shown in Figure 3.14b after the annealing process. After annealing, the current magnitude increased by fivefold and good gate modulation. The contact resistance of MoS<sub>2</sub> transistors was also estimated using transfer length method, where the two-terminal resistances were plotted against the distances between the measuring pair of electrodes. The linear fitting of the two-terminal resistance with respect to the distance between electrodes shows  $2R_c = 4.68 \text{ M}\Omega$ . The result is shown in Figure 3.15. Although the calculation of contact resistance is not precise due to the different contact area for

longitudinal and transverse electrodes, it should be a good estimation on the order of magnitude of the contact resistances nevertheless.

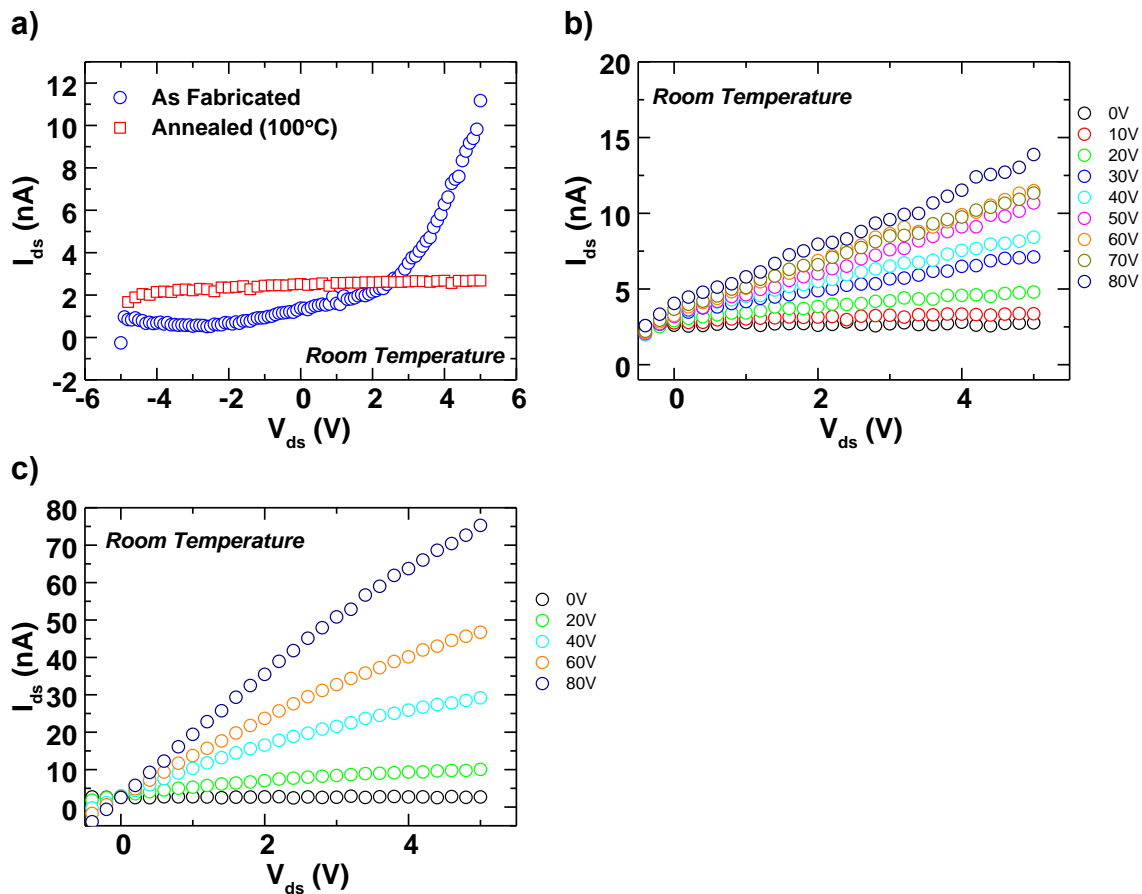


**Figure 3.14.** Optimazation of MoS<sub>2</sub> FET fabrication. a)  $I$ - $V$  of MoS<sub>2</sub> FET at 0 gate bias using un-annealed monolayer MoS<sub>2</sub> as channel. b) Gate voltage dependent  $I$ - $V$  curves with annealed MoS<sub>2</sub> as channel. c) ) Gate voltage dependent  $I$ - $V$  curves with annealed MoS<sub>2</sub> as channel after annealing at 200°C.

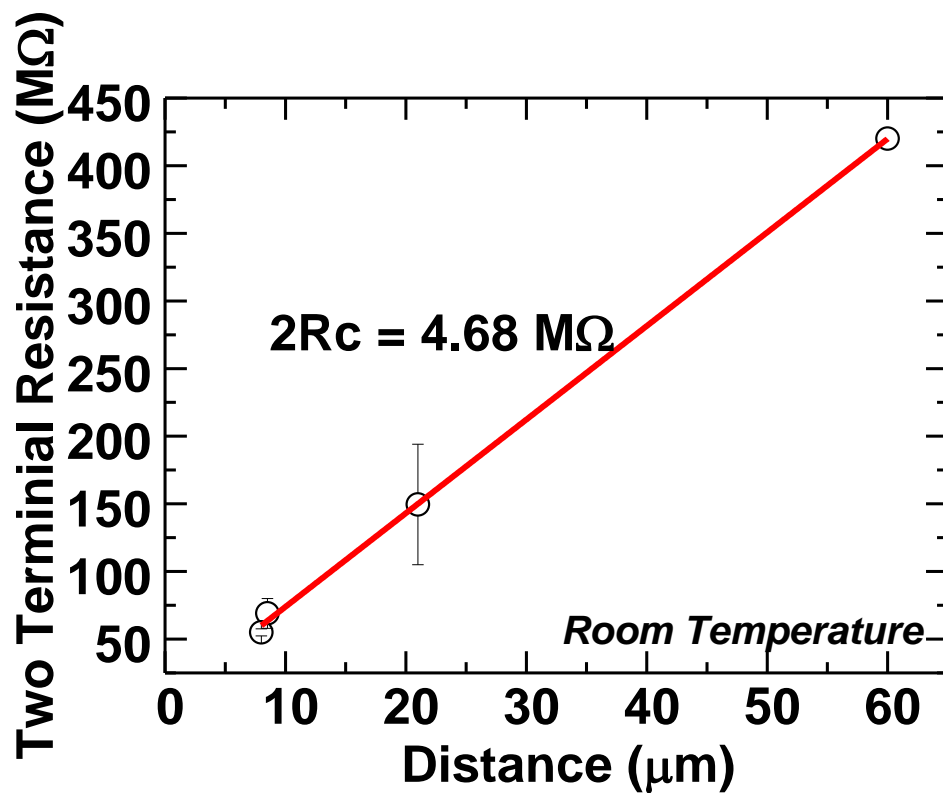


Figure 3.15. Estimation of MoS<sub>2</sub> contact resistance using transfer-length method.

### 3.4.3 MX<sub>2</sub> Field Effect Transistor

#### MoS<sub>2</sub> FET

After successfully reducing contact resistance and optimizing fabrication procedures, monolayer MoS<sub>2</sub> FET were fabricated on Si substrates coated with 300 nm of

SiO<sub>2</sub>. The optical microscope image of fabricated MoS<sub>2</sub> FET/Hall-bar device is shown as inset in Figure 3.16. The source-drain voltage and current  $I_{DS}$  vs  $V_{DS}$  between the longitudinal contacts was measured by Keithley 2400 source meter, while the back-gate voltage was supplied by Keithley 6487 pico-ammeter (used as voltage source) from 0 V to 80 V. The conductivity of the MoS<sub>2</sub> channel increases as the gating voltage  $V_G$  increases, indicating n-type behavior. The leakage current for 300 nm SiO<sub>2</sub> was ~50 pA to 100 pA at 80 V bias, which are significantly less than the source-drain current. Field mobility of monolayer MoS<sub>2</sub> is extracted from the following expression

$$\mu_{FE} = g_m \times \frac{L}{WCV_{DS}}$$

, where length of the channel  $L$  is 60  $\mu\text{m}$ , width of the channel  $W$  is 8  $\mu\text{m}$ , and  $C = 1.15 \times 10^{-4} \text{ F m}^{-2}$  is the capacitance per unit area of SiO<sub>2</sub> layer (300 nm,  $\epsilon_r = 3.10$ ).  $V_{GS}$  vs  $I_{DS}$  were fitted at linear region from 40 V to 80 V for transconductance

$$g_m = \frac{dI_{DS}}{dV_G}$$

The field mobility of the device shown in Figure 3.15 is  $6.7 \pm 0.2 \text{ cm}^2\text{V}^{-1}\text{s}^{-1}$ . The range of field mobility observed for MoS<sub>2</sub> FETs over 7 devices are 0.3 - 6.7  $\text{cm}^2\text{V}^{-1}\text{s}^{-1}$ .

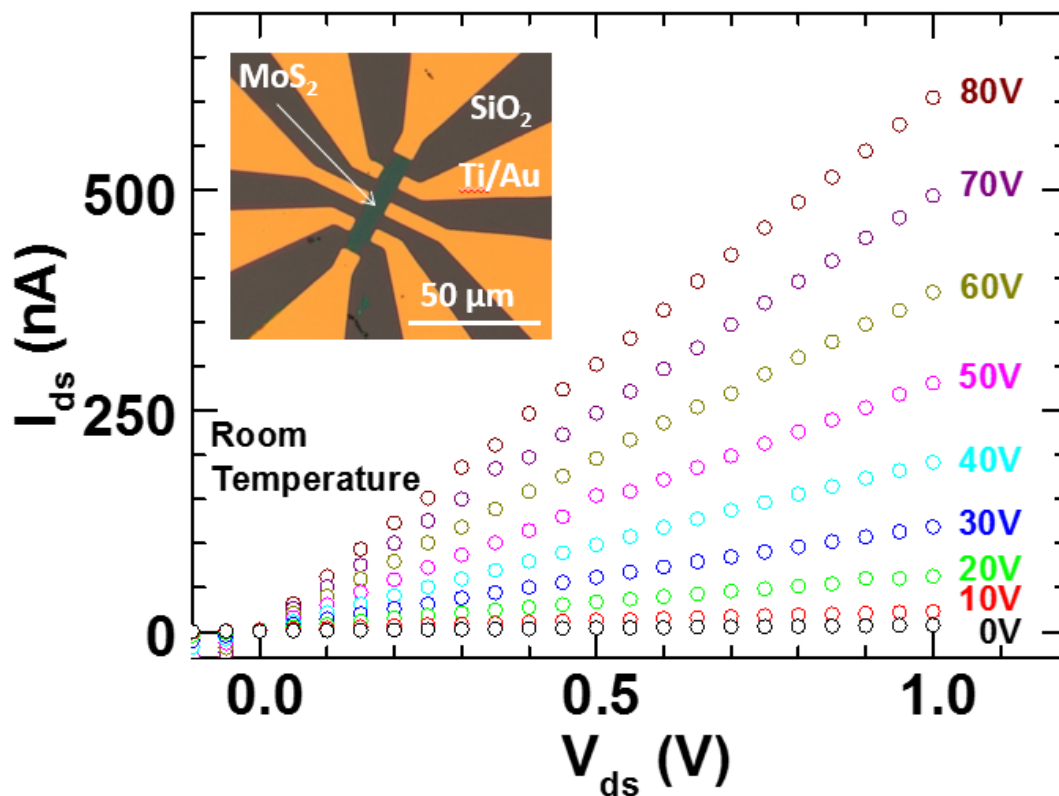


**Figure 3.16.**  $I_{ds}$ - $V_{ds}$  curves of a monolayer MoS<sub>2</sub> field effect transistor at different gate voltage bias. The  $I$ - $V$  measurements were performed on the longitudinal pair of contacts in Hall-bar geometry.

#### Other MX<sub>2</sub> FET

Monolayer MoSe<sub>2</sub>, WS<sub>2</sub>, and WSe<sub>2</sub> FETs were subsequently prepared using the methods described earlier. Ni, Au, and Pd metals were chosen as contacts for MoSe<sub>2</sub>, WS<sub>2</sub>, and WSe<sub>2</sub> devices respectively due to their work functions. The gate voltage was applied from 0 to 80V for n-type WS<sub>2</sub> and MoSe<sub>2</sub> FETs and 30V to -80V for WSe<sub>2</sub> FET.  $I_{ds}$ - $V_{ds}$

curves for each material were measured and shown in Figure 3.17a, 3.17b and 3.17c. The channel currents are well modulated by the gate voltage. The leakage current was  $\sim 50$  pA to 100 pA at 80 V bias. In WS<sub>2</sub> FET, the on-off ratio is  $\sim 10^4$ , while MoSe<sub>2</sub> and WSe<sub>2</sub> FETs have on-off ratio  $\sim 10^3$ . The extract field mobilities for the FETs shown in Figure 3.17a-c, corresponding to MoSe<sub>2</sub>, WS<sub>2</sub>, and WSe<sub>2</sub>, were  $82 \pm 18 \text{ cm}^2\text{V}^{-1}\text{s}^{-1}$ ,  $297 \pm 45 \text{ cm}^2\text{V}^{-1}\text{s}^{-1}$ , and  $12 \pm 3 \text{ cm}^2\text{V}^{-1}\text{s}^{-1}$  respectively. In addition, WSe<sub>2</sub> FET shows p-type behavior due to the Pd contact.<sup>61, 107, 109, 149</sup> The  $I_{\text{ds}}-V_{\text{g}}$  curves were plotted in Figure 3.17d. Most fabricated WS<sub>2</sub> FETs showed high resistivity, possibly due to high Schottky barrier originated from the intrinsic nature of CVD-WS<sub>2</sub><sup>150</sup>, which resulted poor gate modulation of drain-source current. Overall, more than 200 monolayer MX<sub>2</sub> FET devices were fabricated for this study to ensure its reproducibility.

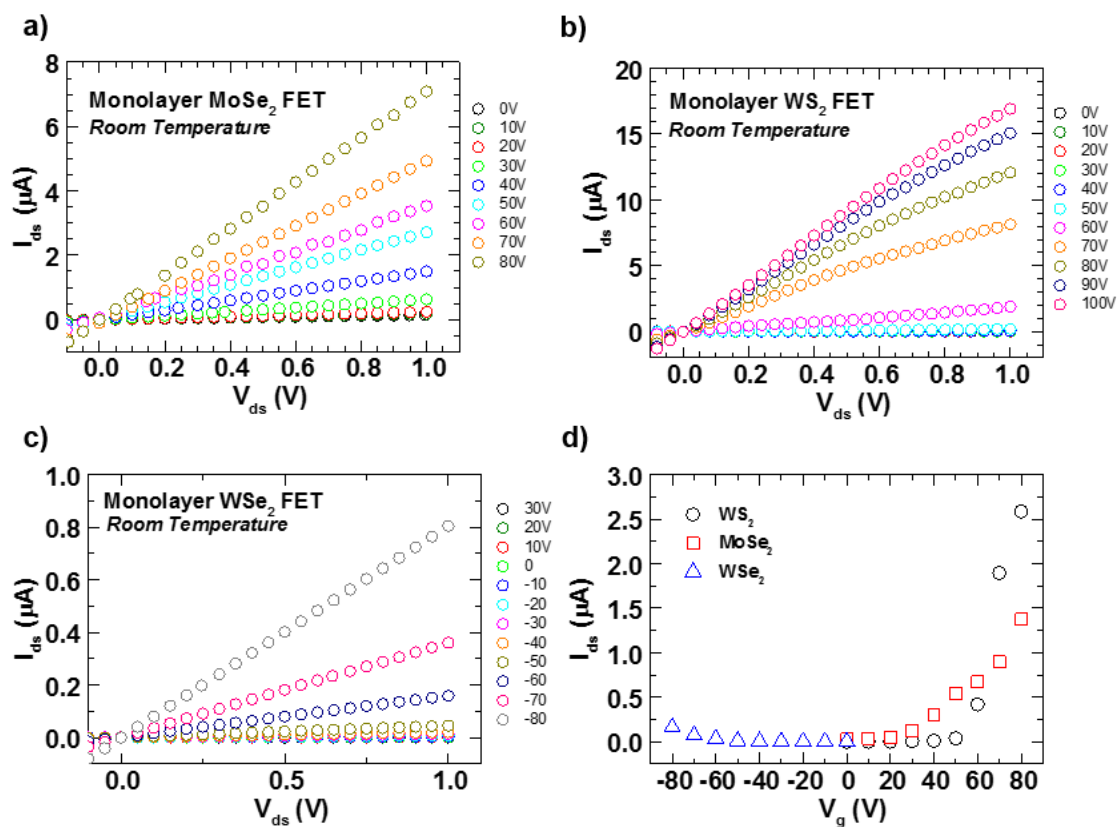


**Figure 3.17.** Gating effect in MoSe<sub>2</sub>, WS<sub>2</sub>, and WSe<sub>2</sub> field-effect transistors. a)  $I_{ds}$ - $V_{ds}$  curves at different gate voltage bias for MoSe<sub>2</sub> transistor. b)  $I_{ds}$ - $V_{ds}$  curves at different gate voltage bias for WS<sub>2</sub> transistor. c)  $I_{ds}$ - $V_{ds}$  curves at different gate voltage bias for WSe<sub>2</sub> transistor. d)  $I_{ds}$ - $V_g$  curves for the three devices shown in Figure 3.16a-c.

### 3.4.5 Hall effect of monolayer MX<sub>2</sub>

Through fabrication of MX<sub>2</sub> FET devices, the field-effect mobility can be extracted from the  $I_{ds}$ - $V_g$  curves. However, these values are typically far away from the intrinsic carrier mobility, especially in 2D materials where contact resistance still plays a major factor in the performance of FET. Furthermore, the field-effect mobility is derived

from the transconductance of  $I_{ds}$ - $V_g$ , in many cases, can cause over estimation due to preferred fitting method. Hall effect is often used in characterization of semiconductor materials. When a current is passed through a semiconductor in the longitudinal direction under an external magnetic field, the electrons and holes of the semiconductor will move in the direct normal to the magnetic field and current, causing a voltage drop across the transverse direction. Due to the measurement method, which measures the resistivity and excludes contact resistance, carrier concentration and mobility of a semiconductor can be measured more accurately.

MoS<sub>2</sub> and WSe<sub>2</sub> Hall-bars were fabricated on insulating substrates described in previous sections. DC current was flown through longitudinal electrodes, and the voltage drops across transverse contacts were measured at different external magnet fields. To account for the resistivity change caused by repeated measurements (ie Joules heating), the magnetic field were zeroed after each magnetic field point. Figure 3.18 shows the Hall effect data of MoS<sub>2</sub> and WSe<sub>2</sub>. At each magnetic field point, the resistivity of MX<sub>2</sub> was measured multiple times. The average and standard deviation of measured resistivity was plot as data point and error bar. After the measurement, the Hall resistance versus magnetic field plot was linear fitted. The slope  $m$  from the linear fitting can be expressed as:

$$m = \frac{dR_{Hall}}{dBz} = \frac{1}{n \times e \times t}$$

, where  $Bz$  is the external magnet field in Tesla,  $n$  is the carrier concentration in  $\text{cm}^{-3}$ ,  $e$  is the electron charge in coulomb, and  $t$  is the thickness of the semiconductor. In 2D materials, the carrier concentration  $n_{2D}$  can be expressed by

$$n_{2D} = n \times t$$

Therefore,

$$n_{2D} = \frac{1}{m \times e}$$

The mobility of carriers can be expressed by

$$\mu_{HALL} = \frac{1}{n \times e \times \rho}$$

Monolayer MoS<sub>2</sub> Hall-bar shown in Figure 3.18a gives Hall mobility of  $118 \pm 4 \text{ cm}^2\text{V}^{-1}\text{s}^{-1}$ . Additionally, the negative slope indicated n-type behavior in CVD-grown MoS<sub>2</sub>. Similarly, Hall mobility of  $22 \pm 2 \text{ cm}^2\text{V}^{-1}\text{s}^{-1}$  and p-type carriers is found in WSe<sub>2</sub> Hall-bar shown in Figure 3.18b. Over 100 Hall-bars were fabricated in this study. WS<sub>2</sub> and MoSe<sub>2</sub> Hall-bars were not measured due to the difficulty to obtain Ohmic contacts in all the electrodes. The summary of the measured Hall mobility and carrier concentration for MoS<sub>2</sub> and WSe<sub>2</sub> Hall bars were listed in Table II.

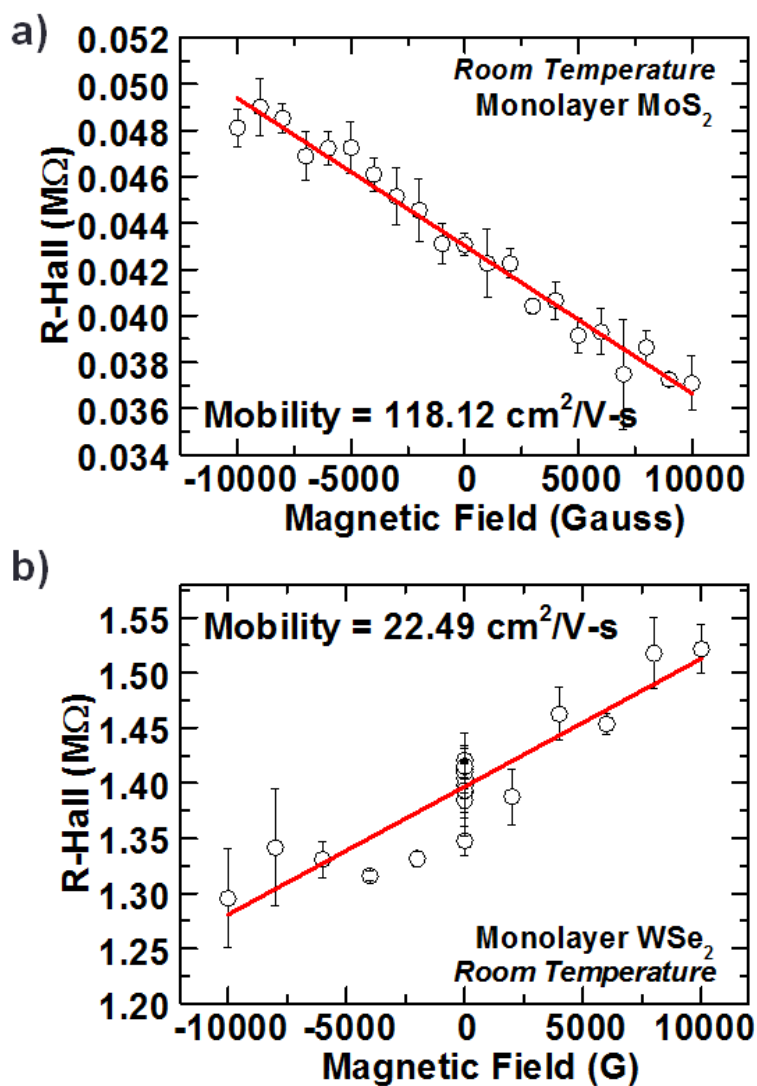


**Figure 3.18.** Hall Effect of monolayer MX<sub>2</sub>. a) Magnetic field dependent Hall resistance in monolayer MoS<sub>2</sub> and b) Magnetic field dependent Hall resistance in monolayer WSe<sub>2</sub>.

**Table II.** Hall Mobility and Carrier Concentration in Monolayer MoS<sub>2</sub> and WSe<sub>2</sub>.

<b>Material</b>	<b>Sample Number</b>	<b>Mobility (cm<sup>2</sup>V<sup>-1</sup>s<sup>-1</sup>)</b>	<b>Carrier Concentration (cm<sup>-2</sup>)</b>
<b>MoS<sub>2</sub></b>	<b>b466A2-A</b>	42 ± 4	1.0 ± 0.3 × 10 <sup>10</sup>
		118 ± 4	2.6 ± 0.2 × 10 <sup>11</sup>
<b>MoS<sub>2</sub></b>	<b>b466A2-B</b>	15 ± 2	7.1 ± 0.8 × 10 <sup>10</sup>
<b>MoS<sub>2</sub></b>	<b>b465A2</b>	5.6 ± 0.8	5.4 ± 0.8 × 10 <sup>11</sup>
		4.1 ± 0.7	7.7 ± 1.2 × 10 <sup>10</sup>
<b>MoS<sub>2</sub></b>	<b>b462A2</b>	19 ± 2	4.7 ± 0.6 × 10 <sup>10</sup>
		12 ± 1	9.8 ± 0.5 × 10 <sup>10</sup>
<b>MoS<sub>2</sub></b>	<b>b461A1</b>	17 ± 2	5.0 ± 0.5 × 10 <sup>10</sup>
<b>WSe<sub>2</sub></b>	<b>e076A3</b>	20 ± 2	6.0 ± 0.6 × 10 <sup>9</sup>
		22 ± 2	5.0 ± 0.5 × 10 <sup>9</sup>
<b>WSe<sub>2</sub></b>	<b>e109B</b>	28 ± 2	1.1 ± 0.1 × 10 <sup>10</sup>
<b>WSe<sub>2</sub></b>	<b>e109A</b>	6.3 ± 0.8	5.4 ± 0.7 × 10 <sup>10</sup>
		17 ± 2	1.1 ± 0.1 × 10 <sup>11</sup>
<b>WSe<sub>2</sub></b>	<b>e110B</b>	12 ± 1	1.5 ± 0.1 × 10 <sup>11</sup>
		1.7 ± 0.2	3.9 ± 0.4 × 10 <sup>11</sup>
<b>WSe<sub>2</sub></b>	<b>e114A</b>	4.2 ± 0.3	1.6 ± 0.1 × 10 <sup>11</sup>
		4.0 ± 0.5	1.5 ± 0.2 × 10 <sup>11</sup>
<b>WSe<sub>2</sub></b>	<b>e116A</b>	4.6 ± 0.5	1.3 ± 0.2 × 10 <sup>11</sup>
		7.4 ± 0.5	9.2 ± 0.1 × 10 <sup>10</sup>

### **3.5 Summary**

CVD-grown MX<sub>2</sub> monolayers were characterized under OM and SEM to determine their respective domain sizes. Then, Raman and PL spectroscopy were performed on as-grown MX<sub>2</sub> nanosheets. Raman spectra of MoS<sub>2</sub> and WS<sub>2</sub> showed layer dependence. The PL spectra confirmed the MX<sub>2</sub> nanosheets were direct band-gap semiconductors and verified their monolayer nature. These results are in good agreement with literature. More than 200 FET devices and 100 Hall-bar devices were fabricated for the electrical characterization of monolayer MX<sub>2</sub>. The contact resistance is successfully reduced through a series of optimization both in growth and fabrication process. Field-effect mobility up to  $6.7 \pm 0.2 \text{ cm}^2\text{V}^{-1}\text{s}^{-1}$ ,  $82 \pm 18 \text{ cm}^2\text{V}^{-1}\text{s}^{-1}$ ,  $297 \pm 45 \text{ cm}^2\text{V}^{-1}\text{s}^{-1}$ , and  $12 \pm 3 \text{ cm}^2\text{V}^{-1}\text{s}^{-1}$  were extract from  $I_{\text{ds}}-V_{\text{g}}$  curves in MoS<sub>2</sub>, MoSe<sub>2</sub>, WS<sub>2</sub>, and WSe<sub>2</sub> respectively. Hall Effect was measured in MoS<sub>2</sub> and WSe<sub>2</sub> Hall-bar device. Hall mobility up to  $118 \pm 4 \text{ cm}^2\text{V}^{-1}\text{s}^{-1}$  and  $28 \pm 2$  were measured from CVD grown MoS<sub>2</sub> and WSe<sub>2</sub> monolayers. These results confirm the crystallinity and monolayer nature of CVD grown MX<sub>2</sub>, as well as electrical performance of MX<sub>2</sub> monolayers.

## CHAPTER 4

### SPIN VALVES BASED ON TRANSITION-METAL DICHALCOGENIDES

#### **4.1 Introduction**

The development of 2D material spin valves were discussed in Chapter 1. Despite these results, it is difficult to assess the viability of MX<sub>2</sub> spin valves as most of the existing literature focuses demonstrating proof-of-concept devices, which lacks the depth and spectrum of analysis<sup>90, 92, 151</sup>. Furthermore, some of the reported MX<sub>2</sub> spin valves have yet to show room temperature MR. In this chapter, spin valve effect based on monolayer MX<sub>2</sub> over several devices. To understand the physics of MX<sub>2</sub> spin valves, annealing and layer dependency effect were investigated. Additionally, the anisotropy nature of these devices and fabricated exchange bias pinned spin valve as a demonstration of a more practical approach of fabrication were studied. Finally, the life time and aging effect of the MX<sub>2</sub> spin valves were studied over a period of 6 months in ambient conditions. These results covers a broader area of interest over several MX<sub>2</sub> spin valves and will result an overall unbiased understanding of MX<sub>2</sub> as spacer layers in magnetic tunneling junctions.

## **4.2 Experiment**

### Fabrication of monolayer TMDC spin valves

*Bottom electrode* The vertical TMDC spin valves were fabricated using Permalloy (Ni 80% Fe 20%), TMDC monolayer, and Co as bottom electrode, insulating layer, and top electrode, respectively. The bottom Py electrodes were fabricated on SiO<sub>2</sub> coated Si substrates by standard photo-lithography, e-beam evaporation deposition, and liftoff process. The dimensions of Py (4 μm × 100 μm) bottom electrode arrays were designed to increase the transfer process success rate. Shipley1811 photoresist were spun-coated at 3000 rpm for 30 s, then soft-baked at 115°C for 60 s. The thickness for the photoresist is 1.3 μm. The exposure for the pattern was carried out in Microtech LW405 laser pattern generator (direct-write photolithography tool). After exposure, the substrates were developed in diluted Microchem 351 developer (351:H<sub>2</sub>O = 1:3) solution for 30 s, then rinsed by DI water, finally followed by careful inspection under the Olympus MX61 optical microscope. Py deposition was performed under a home-built e-beam evaporator system with a base pressure of  $1 \times 10^{-8}$  Torr at a deposition rate of 0.5 Å/s. Liftoff was subsequently performed by immersing the substrates in acetone for 20 minutes. After liftoff, the substrates were cleaned with acetone, IPA, DI water, and dried by N<sub>2</sub> gun.

Transfer process As-grown MX<sub>2</sub> monolayers on SiO<sub>2</sub>/Si substrates were transferred onto the SiO<sub>2</sub> coated Si substrates with pre-deposited Py metal electrode arrays. First, the as-grown MX<sub>2</sub> monolayers were spin coated with a 1:1 mixture of Microchem PMMA A5 and A6 at 3000 rpm then baked at 180°C to remove the solvents. The thickness of the PMMA is ~ 3 μm. Then, the spin coated samples were dip into 10% HF solution for 20 minutes to etch away the SiO<sub>2</sub> layer. The PMMA-coated-MX<sub>2</sub>-monolayers were subsequently transferred to the substrates with Py electrodes, followed by a baking at 100°C for 20 minutes to remove water molecules. Finally, the PMMA was removed with acetone, rinsed by DI water, and dried by N<sub>2</sub> gun.

Top electrodes Top electrodes were patterned by in Microtech LW405 laser pattern generator using Shipley S1811 photoresist. The resist was spun-coated at 3000 rpm for 30 s then baked at 115°C for 60 s. The 10 nm of Co and 10 Au films were deposited in a e-beam evaporator system (Lesker PVD-250) with base pressure in the 10<sup>-8</sup> Torr range. The deposition is carried out at room temperature. Liftoff was performed by immersing the substrates in acetone for 20 minutes and subsequently cleaned with acetone, IPA, DI water, and dried by N<sub>2</sub> gun.

Lead electrodes The lead electrodes connecting to top and bottom ferromagnetic

electrodes were fabricated by standard photo-lithography, e-beam evaporation deposition, and liftoff process. The large contacts ( $300\ \mu\text{m} \times 300\ \mu\text{m}$ ) were fabricated for probe measurements and wire bonding. Shipley1811 photoresist were spun-coated at 3000 rpm for 30 s, then soft-baked at  $115^\circ\text{C}$  for 60 s. The thickness for the photoresist is  $1.3\ \mu\text{m}$ . The exposure for the pattern was carried out in Microtech LW405 laser pattern generator. After exposure, the substrates were developed in diluted Microchem 351 developer solution for 30 s, then rinsed by DI water. 10nm Ti and 50 nm Au were deposited under a home-built e-beam evaporator system with a base pressure of  $1 \times 10^{-8}$  Torr at a deposition rate of 0.6 Å/s and 1 Å/s. Liftoff was subsequently performed by immersing the substrates in acetone for 20 minutes. After liftoff, the substrates were cleaned with acetone, IPA, DI water, and dried by  $\text{N}_2$  gun.

The whole fabrication process is shown in Figure 4.1.

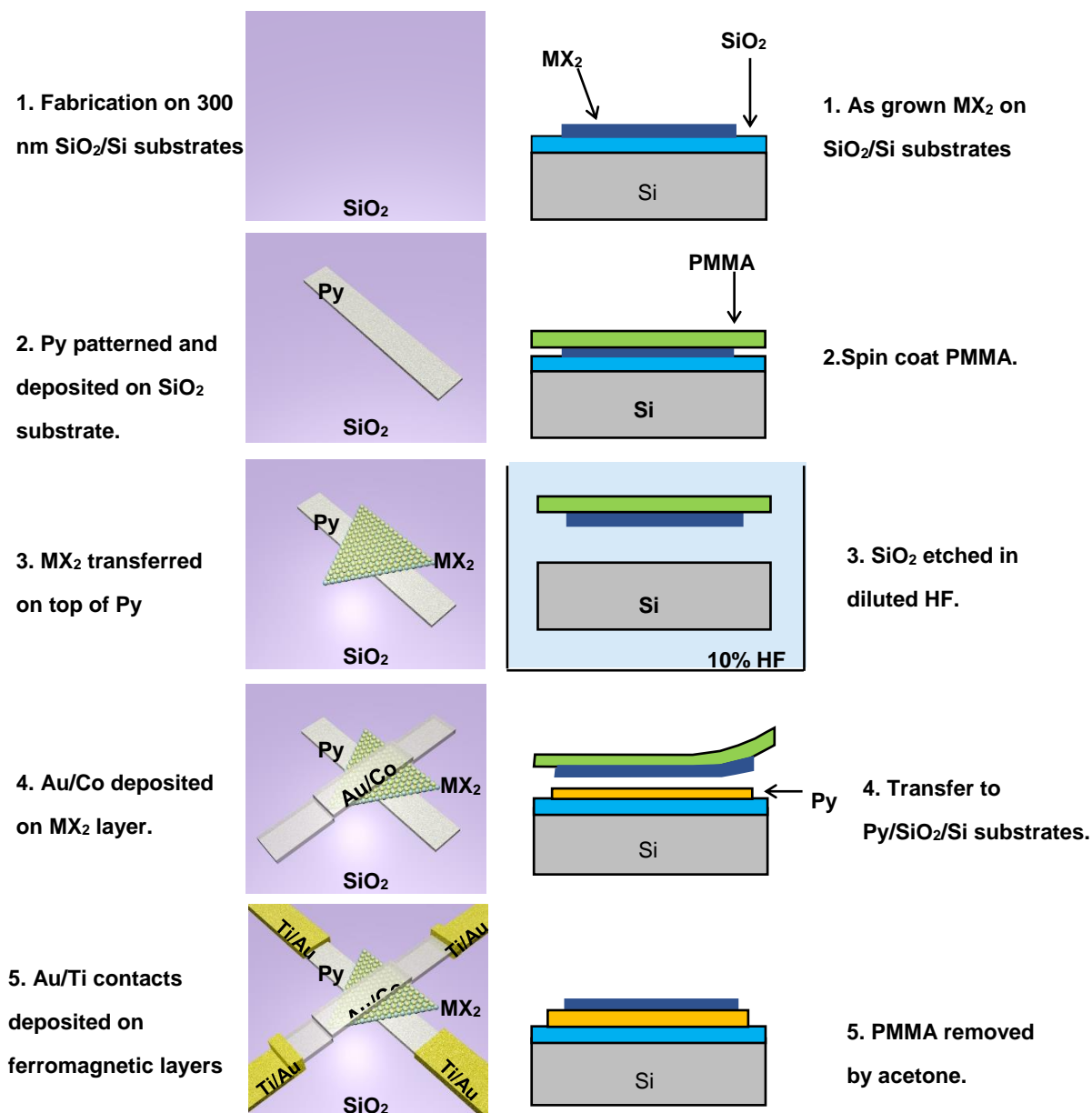


**Figure 4.1.** Fabrication process for  $\text{MX}_2$  spin valves.

### Measurements

The fabricated MTJ devices were wire-bonded (Westbond 7476D) to a Chelsea Tech. chip carrier then mounted to a home-built cryogenic measurement system equipped with Lakeshore EM4 electromagnet, Lakeshore 643 electromagnet power supply, Lakeshore 475 gauss meter, Thermo Scientific ThermalFlex 2500 water chiller, and cryogen-free Janis cryostat. The temperature is controlled by Lakeshore 335. The junction resistances versus applied magnetic field were measured from 16K to room temperature. Keithley 6221 AC/DC current source meter and 2182A nano-voltmeter were used to supply current and measure the voltage drop across the junctions respectively. The junction IVs were measured several times at a single magnetic field point and IVs were linearly fitted to obtain the resistance value. Four-probe measurement method was employed to exclude the magnetoresistance from the Co and Py electrodes as well as the resistance from the Ti/Au leads.

## **4.3 Results and Discussion**

### **4.3.1 Characterization**

Monolayer and few-layered MoS<sub>2</sub>, WS<sub>2</sub>, MoSe<sub>2</sub>, and WSe<sub>2</sub> single crystals were grown on SiO<sub>2</sub> substrates using chemical vapor deposition (CVD) with the detailed method described in experimental section. As-grown MX<sub>2</sub> nanosheets are typically ~50 – 200  $\mu\text{m}$ , and were imaged under scanning electron microscopy (SEM) as shown in Figure 4.2a. The triangular shaped domain of the as-grown nanosheets indicates that they are single crystals. Subsequently, the MX<sub>2</sub> nanosheets are characterized under photoluminescence (PL) and Raman spectroscopy. The PL spectrum of MX<sub>2</sub> under 514nm laser are shown in Figure 4.2b. One sharp peak was found for each MX<sub>2</sub> at 1.81 (MoS<sub>2</sub>), 1.96 (WS<sub>2</sub>), 1.52 (MoSe<sub>2</sub>), and 1.57 (WSe<sub>2</sub>) eV. Monolayer TMDCs are direct bandgap materials, thus PL is only evident when the 2D crystal is monolayer therein. MX<sub>2</sub> nanosheets were then studied under Raman spectroscopy excited with 514 nm laser. Under such conditions, MoS<sub>2</sub> and WS<sub>2</sub> have two dominant peaks, E<sub>2g</sub><sup>1</sup> and A<sub>1g</sub>, located at 382 cm<sup>-1</sup> and 402 cm<sup>-1</sup> for MoS<sub>2</sub> and at 352 cm<sup>-1</sup> and 402 cm<sup>-1</sup> for WS<sub>2</sub> shown in Figure 4.2c. In MoS<sub>2</sub> and WS<sub>2</sub>, the difference between E<sub>2g</sub><sup>1</sup> and A<sub>1g</sub> modes can be used to identify monolayers. Considering the ~ cm<sup>-1</sup> resolution of the Raman system, the distance between

the two modes ( $\Delta = A_{1g} - E_{2g}^1$ ) for MoS<sub>2</sub> and WS<sub>2</sub> is  $20 \pm 1 \text{ cm}^{-1}$  and  $62 \pm 1 \text{ cm}^{-1}$ . These values agree with monolayer CVD MoS<sub>2</sub><sup>98-99, 152</sup> and WS<sub>2</sub><sup>104, 152</sup> in literature. As-grown MoSe<sub>2</sub> and WSe<sub>2</sub> have A<sub>1g</sub> peaks located at  $240 \text{ cm}^{-1}$  and  $248 \text{ cm}^{-1}$  respectively also shown in Figure 4.2c. PL and Raman measurements combined with the contrast of different layer thickness in optical microscope (OM) images confirm the high quality and monolayer nature of CVD grown MX<sub>2</sub>.

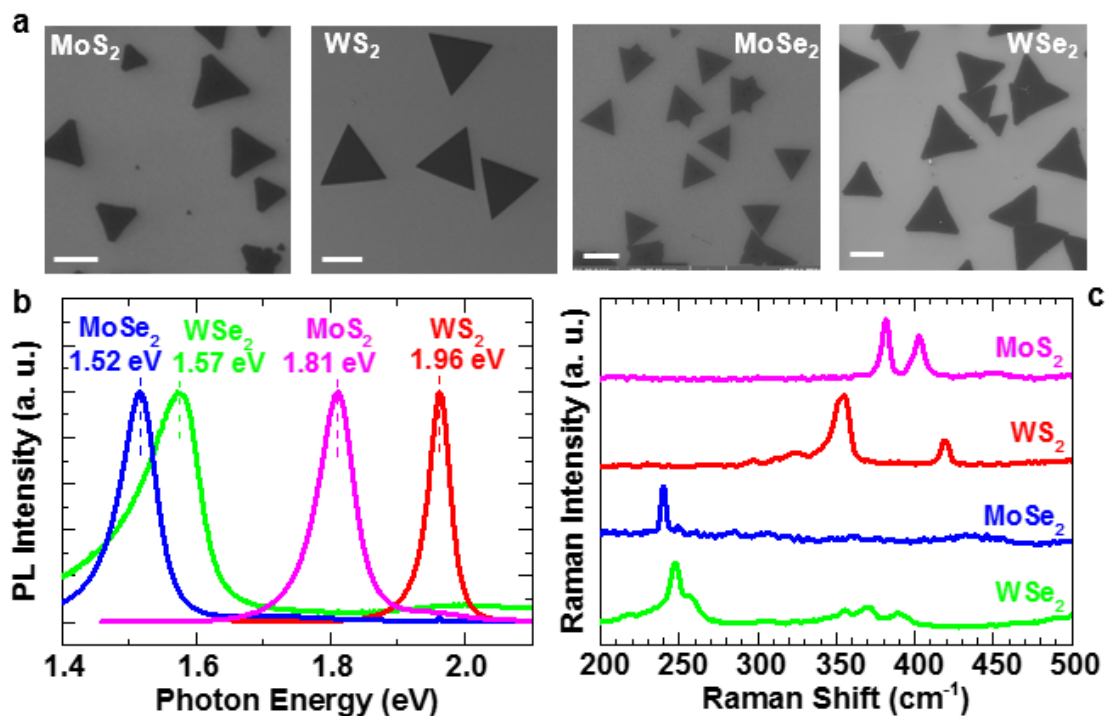


**Figure 4.2.** Characterizations of as-grown MoS<sub>2</sub>, WS<sub>2</sub>, MoSe<sub>2</sub>, and WSe<sub>2</sub> monolayer by chemical vapor deposition. (a) Scanning electron microscopy images of MoS<sub>2</sub>, WS<sub>2</sub>, MoSe<sub>2</sub>, and WSe<sub>2</sub> monolayers, from left to right respectively. The scale bars in the images are 20  $\mu\text{m}$ , 100  $\mu\text{m}$ , 20  $\mu\text{m}$ , and 20  $\mu\text{m}$  from left to right respectively. (b) Photoluminescence spectra of MoS<sub>2</sub>, WS<sub>2</sub>, MoSe<sub>2</sub>, and WSe<sub>2</sub> monolayers. (c) Raman Spectra of MoS<sub>2</sub>, WS<sub>2</sub>, MoSe<sub>2</sub>, and WSe<sub>2</sub> monolayers

### 4.3.2 TMR of Monolayer MX<sub>2</sub> Spin Valves

A cross-sectional view of the pseudo-spin valve structure is shown in Figure 4.3a, consisting of Co/MX<sub>2</sub>/Py core, a 10 nm Au layer to encapsulate Co electrodes, and

Ti/Au connection leads. The measurement setup and the top view schematic of the spin valve is shown in Figure 4.3b. Four probe  $I$ - $V$  measurement method was employed to measure the junction resistance which excludes the resistance contribution from the Ti/Au lead connections. A representative OM image of multiple  $\text{MX}_2$  spin valve was shown in a Figure 4. 3c. A blue-green colored single crystal  $\text{MX}_2$  is sandwiched between Py and Co electrodes. Unlike graphene spin valves, the  $\text{MX}_2$  outside the junction area are not etched due to  $\text{MX}_2$ 's high in-plane resistance. A list of all fabricated monolayer  $\text{MX}_2$  spin valve and their  $\Delta\text{MR}/R$  shown in Table III. One MR from each of the monolayer  $\text{MX}_2$  material shown in Figure 4.3. The junction  $I$ - $V$  of  $\text{MX}_2$  spin valves at both room temperature and 16K are linear and shown in Figure 4.5. The junction resistance - area products of the fabricated spin valves are  $\sim 200 - 300 \Omega\mu\text{m}^2$ . Density functional theory calculations report by Wang *et al*<sup>90</sup> and Dankert *et al*<sup>91</sup> suggest that  $\text{MoS}_2$ -Py interface has strong hybridization, which lead to the junction's metallic nature. In few layered  $\text{MoS}_2/\text{Al}_2\text{O}_3$  spin valves, Dankert *et al* was able to observe non-linear I-V curves possibly due to the presence of an  $\text{Al}_2\text{O}_3$  layer. Before each MR scan, the two FM electrodes were aligned by either -1000 or 1000 Gauss magnetic field. The junction resistance was measured from -50 Gauss to 50 Gauss and vice versa as indicated by the arrows in the Figure 4.3. Figure 4.3a shows the

room temperature MR response of a MoS<sub>2</sub> junction (Device B in Table III). A ‘bump’ in junction resistance was observed at each scanning direction, which corresponds to typical spin valve response. In MoS<sub>2</sub> spin valve when the two FM electrodes are antiparallel aligned, the junction has higher electrical resistance, which results in a positive  $\Delta\text{MR}/R$  of 0.40% at room temperature.  $\Delta\text{MR}/R$  is directly related to polarization which is described in Julliere’s work<sup>8</sup> such that  $\Delta\text{MR}/R = 2P_1P_2 / (1 - P_1P_2)$  where  $P_1$  and  $P_2$  are the spin polarization of Co and Py electrodes. In the assumption that Co and Py have similar behavior,  $P = P_1 = P_2$ , MoS<sub>2</sub> junction shows  $P = 4.4\%$  at room temperature. Room-temperature MR of WS<sub>2</sub> junction (Device E) is shown in Figure 4.3b, with a highest  $\Delta\text{MR}/R$  ratio of ~0.53% out of all the fabricated monolayer MX<sub>2</sub> junctions and corresponds to  $P = 5.0\%$  at room temperature. This result is also highest reported  $\Delta\text{MR}/R$  in monolayer MX<sub>2</sub> spin valves so far. MoSe<sub>2</sub> and WSe<sub>2</sub> spin valve devices (Device K and O) show ~0.21% and ~0.15%  $\Delta\text{MR}/R$  at room temperature as shown in Figures 3c and 3d. To further confirm the origin of the MR in the MX<sub>2</sub> spin valves, two types of reference devices were fabricated. The first type of reference device (Device U) was fabricated without the transfer process, hence a junction composed of only Co/Py. The second type of reference device (Device V) was fabricated along with MX<sub>2</sub> spin valves, which has an additional transfer

process. The additional transfer process may introduce PMMA residue. The corresponding  $\Delta MR/R$  of the junctions were then measured at both room temperature and 16 K. In both of the reference devices, no spin valve effect was observed as shown in Figure 4.4. However, the device adjacent to device V is a WSe<sub>2</sub> spin valve, device O, which showed clear TMR response as shown in Figure 4.3d. These results undoubtedly suggest that the MR responses are originated from monolayer MX<sub>2</sub>, and thus showing MX<sub>2</sub> even at monolayer thickness, can achieve reasonable spin filtering capabilities.

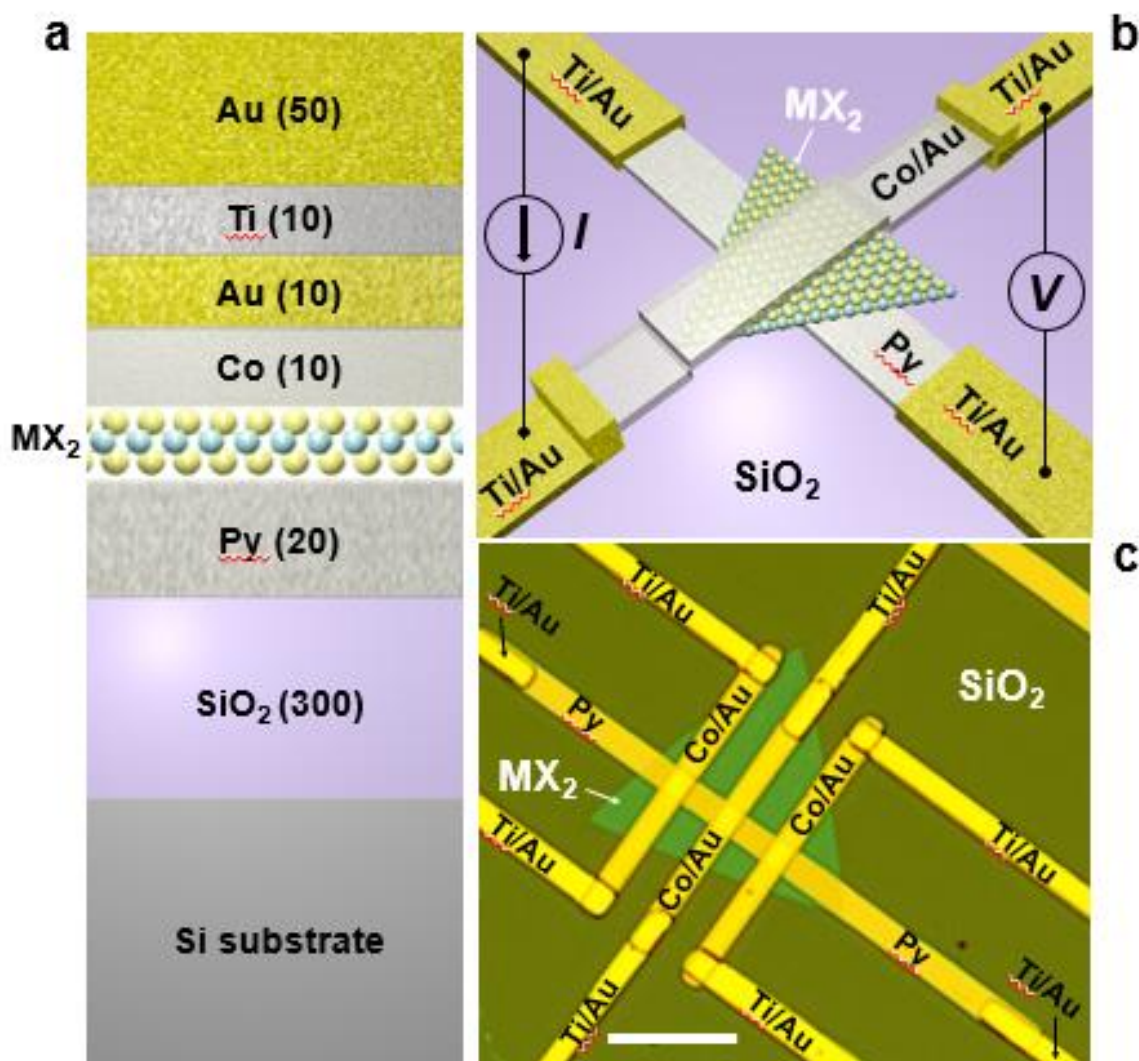


**Figure 4.3.** Device Structure of the MX<sub>2</sub> spin valves. (a) A cross-sectional view schematic of spin valves. The unit of the numbers in the brackets is nm, representing the thickness of each layer. (b) A top-view schematic of the spin valves. Four-probe configuration were employed to measure the tunneling magnetoresistance of the spin valves, with current flowing between two electrodes while voltage measured between the other two electrodes. (c) An optical microscope image of a representative fabricated MX<sub>2</sub> monolayer spin valve device (WSe<sub>2</sub>, Device Q in Table III). The scale bar in the image is 20  $\mu\text{m}$ .

**Table III.** List of Measured Monolayer TMDC Spin Valves.

Device Number	Spacer layer	Number of Layers	Annealed	Annealing Temperature (°C)	TMR at Room-temperature	TMR at ~16K
<b>A</b>	MoS <sub>2</sub>	Monolayer	N	N/A	~0.60%	~0.94%
<b>B</b>	MoS <sub>2</sub>	Monolayer	N	N/A	0.40±0.04%	0.75±0.03%
<b>C</b>	MoS <sub>2</sub>	Monolayer	N	N/A	0.13±0.02%	~0.50%
<b>D</b>	MoS <sub>2</sub>	Monolayer	N	N/A	~0.34%	
<b>E</b>	WS <sub>2</sub>	Monolayer	N	N/A	~0.70% 0.53±0.05%	~1.42% 1.03±0.03%
<b>F</b>	WS <sub>2</sub>	Monolayer	N	N/A	~0.26%	
<b>G</b>	WS <sub>2</sub>	Monolayer	N	N/A	~0.17%	~0.78%
<b>H</b>	WS <sub>2</sub>	Monolayer	N	N/A	~0.24% ~0.25%	~0.55%
<b>I</b>	WS <sub>2</sub>	Monolayer	N	N/A	~0.24%	
<b>J</b>	WS <sub>2</sub>	Monolayer	N	N/A	~0.21%	
<b>K</b>	MoSe <sub>2</sub>	Monolayer	N	N/A	0.21±0.01%	0.48±0.03%
<b>L</b>	MoSe <sub>2</sub>	Monolayer	N	N/A	~0.30%	~0.41%
<b>M</b>	MoSe <sub>2</sub>	Monolayer	N	N/A	~0.23%	
<b>N</b>	MoSe <sub>2</sub>	Monolayer	N	N/A	0.19±0.01%	
<b>O</b>	WSe <sub>2</sub>	Monolayer	N	N/A	0.15±0.01%	0.46±0.01%
<b>P</b>	WSe <sub>2</sub>	Monolayer	N	N/A	~0.20% 0.17±0.01%	~0.37%
<b>Q</b>	WSe <sub>2</sub>	Monolayer	N	N/A	~0.10%	
<b>R</b>	WSe <sub>2</sub>	Monolayer	N	N/A	~0.21%	
<b>S</b>	WSe <sub>2</sub>	Monolayer	N	N/A	~0.11%	
<b>T<sup>a</sup></b>	WS <sub>2</sub>	Monolayer	N	N/A	0.21±0.03%	0.38±0.04%
<b>U</b>	Reference device <sup>b</sup>		N	N/A	0%	0%
<b>V</b>	Reference device <sup>c</sup>		N	N/A	0%	0%

**Table III(continued).** List of Measured Monolayer TMDC Spin Valves.

Device Number	Spacer layer	Number of Layers	Annealed	Annealing Temperature (°C)	TMR at Room-temperature	TMR at ~16K
---------------	--------------	------------------	----------	----------------------------	-------------------------	-------------

- a Py layer is PtMn pinned.
- b Reference device fabricated without transfer process.
- c Reference device fabricated with transfer process.

The MR of fabricated MX<sub>2</sub> spin valves were subsequently measured at low temperature. Figure 4.6. shows the MR from the same devices (Device B, E, K, and O) appeared in Figure 4.3a-d at 16K, 50K, 100K, 150K, 200K, 250K, and 295K. Resistance ‘bumps’ were also observed at different temperature for all four MX<sub>2</sub> spin valves. At low temperatures, the shape of MR response becomes wider and shifted due to increased coercivities in FM at low temperatures, and  $\Delta MR/R$  ratio increase due to increase of spin polarization from reduced scattering at the FM/MX<sub>2</sub> interface. The temperature dependent MR measurement for a monolayer MoS<sub>2</sub> (Device B) is shown in Figure 4.6a. At 16K, the MoS<sub>2</sub> junctions showed  $\Delta MR/R$  ratio of 0.75% (16K), 0.67% (50K), 0.61% (100K), 0.54% (150K), 0.49% (200K), 0.42% (250K), and 0.38% (300K). Additionally, spin polarization P was found to be 6.1% for MoS<sub>2</sub> junctions at 16K. Similar responses were obtained from

other fabricated monolayer  $\text{MX}_2$  spin valves indicating good reproducibility. In monolayer  $\text{WS}_2$  junctions shown in Figure 4.6b, 1.03%  $\Delta R/R$  at 16K was measured which corresponds to  $P = 7.2\%$ ,  $\Delta R/R$  decreases slightly with increasing temperature. At 295K, the MR ratio was found to be 0.5%. At 16K, monolayer  $\text{WS}_2$  spin valves also showed highest reported MR ratio in all reported monolayer  $\text{MX}_2$  junctions so far. Monolayer  $\text{MoSe}_2$  and  $\text{WSe}_2$  spin valves were also studied at various temperatures. Monolayer  $\text{MoSe}_2$  spin valves showed 0.48% MR at 16K, and 0.46% MR was observed in monolayer  $\text{WSe}_2$  spin valve at 16K. The polarization  $P$  was calculated to be 4.9% and 4.8% for  $\text{MoSe}_2$  and  $\text{WSe}_2$  spin valves respectively. In both transition-metal diselenides spin valves,  $\Delta R/R$  also reduced at elevated temperatures.

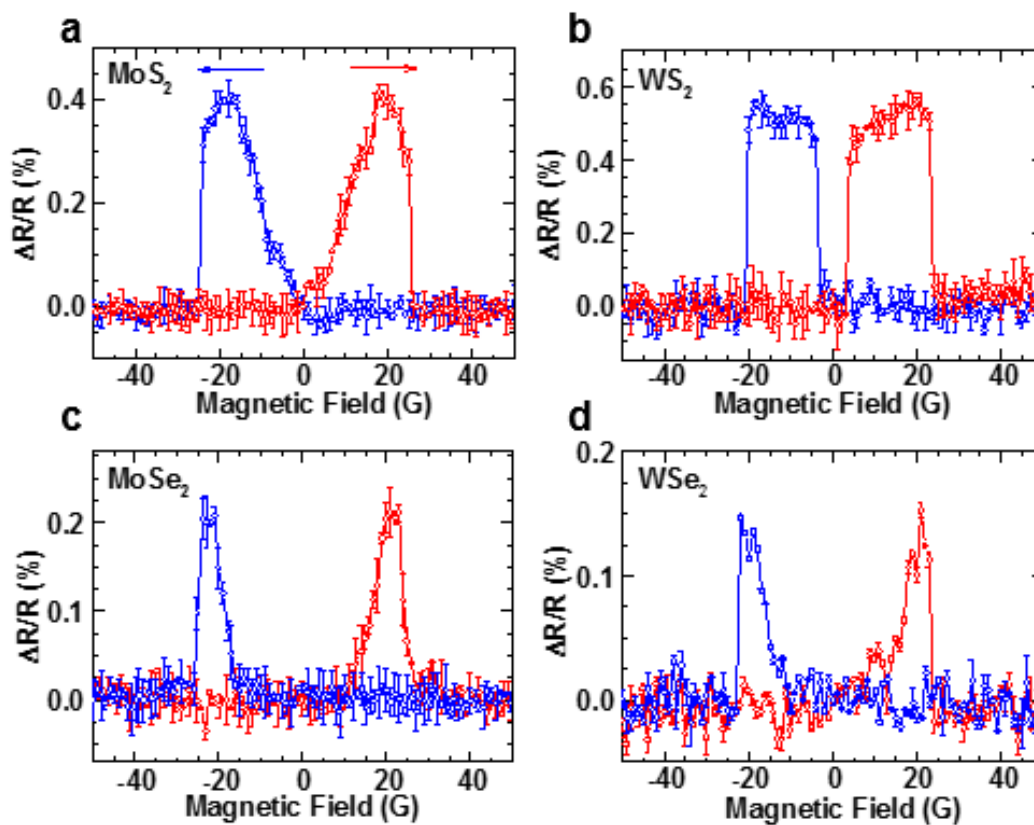


**Figure 4.3.** Room temperature tunneling magnetoresistance (TMR) of monolayer MX<sub>2</sub> spin valves. (a) TMR of monolayer MoS<sub>2</sub> spin valve (Device B) at room temperature. (b) TMR of monolayer WS<sub>2</sub> spin valve (Device E) at room temperature. (c) TMR of monolayer MoSe<sub>2</sub> spin valve (Device K) at room temperature. (d) TMR of monolayer WSe<sub>2</sub> spin valve (Device O) at room temperature.

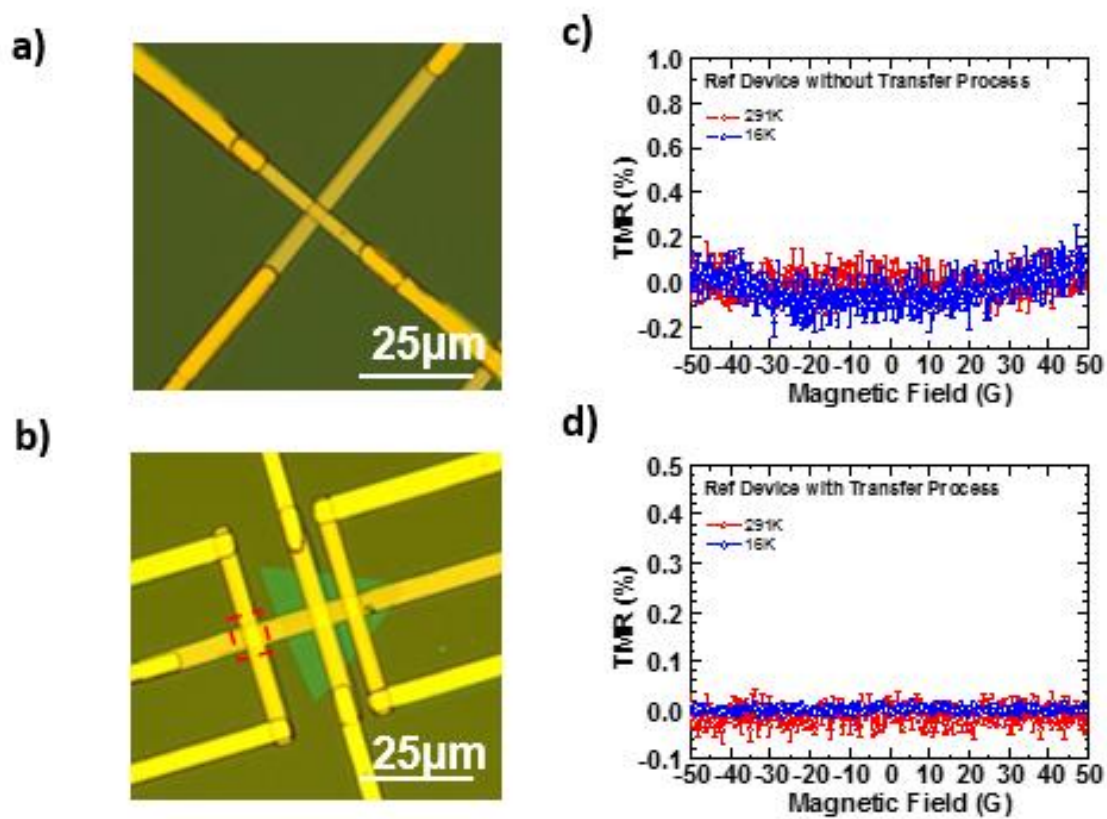


**Figure 4.4.** Magnetoresistance of reference devices without MX<sub>2</sub> insulating layer. a) OM image of a junction without PMMA transfer process. b) OM image of a junction with PPMA transfer process. c) MR of reference device without PMMA transfer process. d) MR with PPMA transfer process

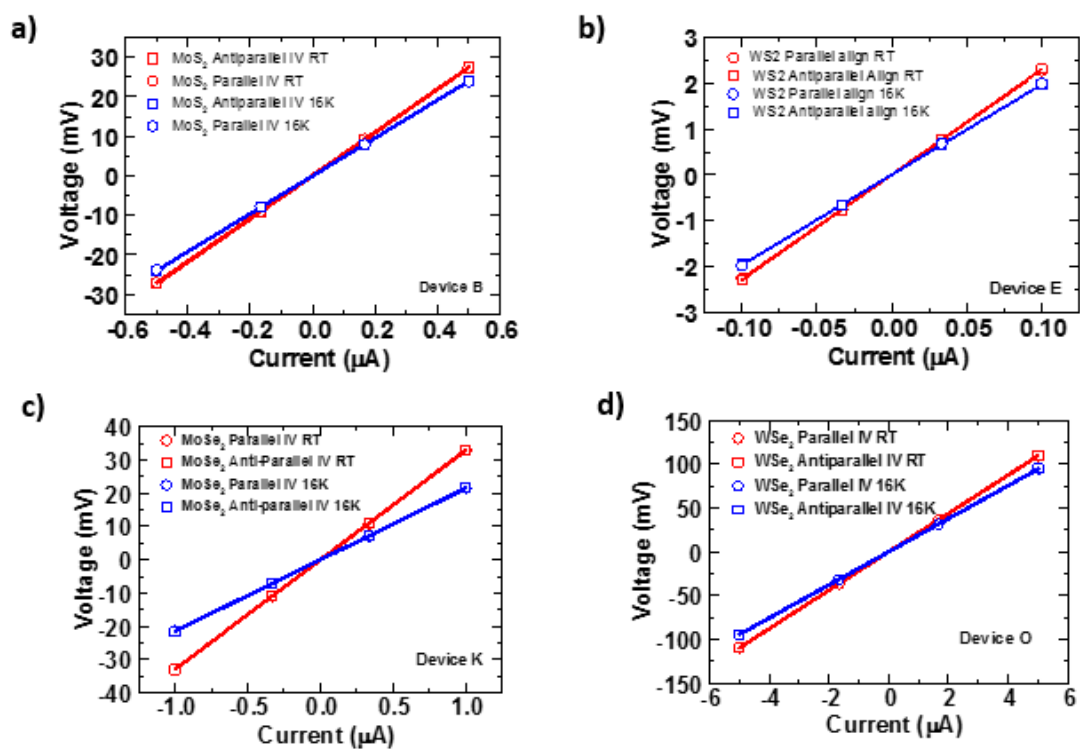


**Figure 4.5.** Junction  $I$ - $V$  characteristics for MX<sub>2</sub> spin valves. a) MoS<sub>2</sub>, b) WS<sub>2</sub>, c) MoSe<sub>2</sub>, d) WSe<sub>2</sub> spin valves.

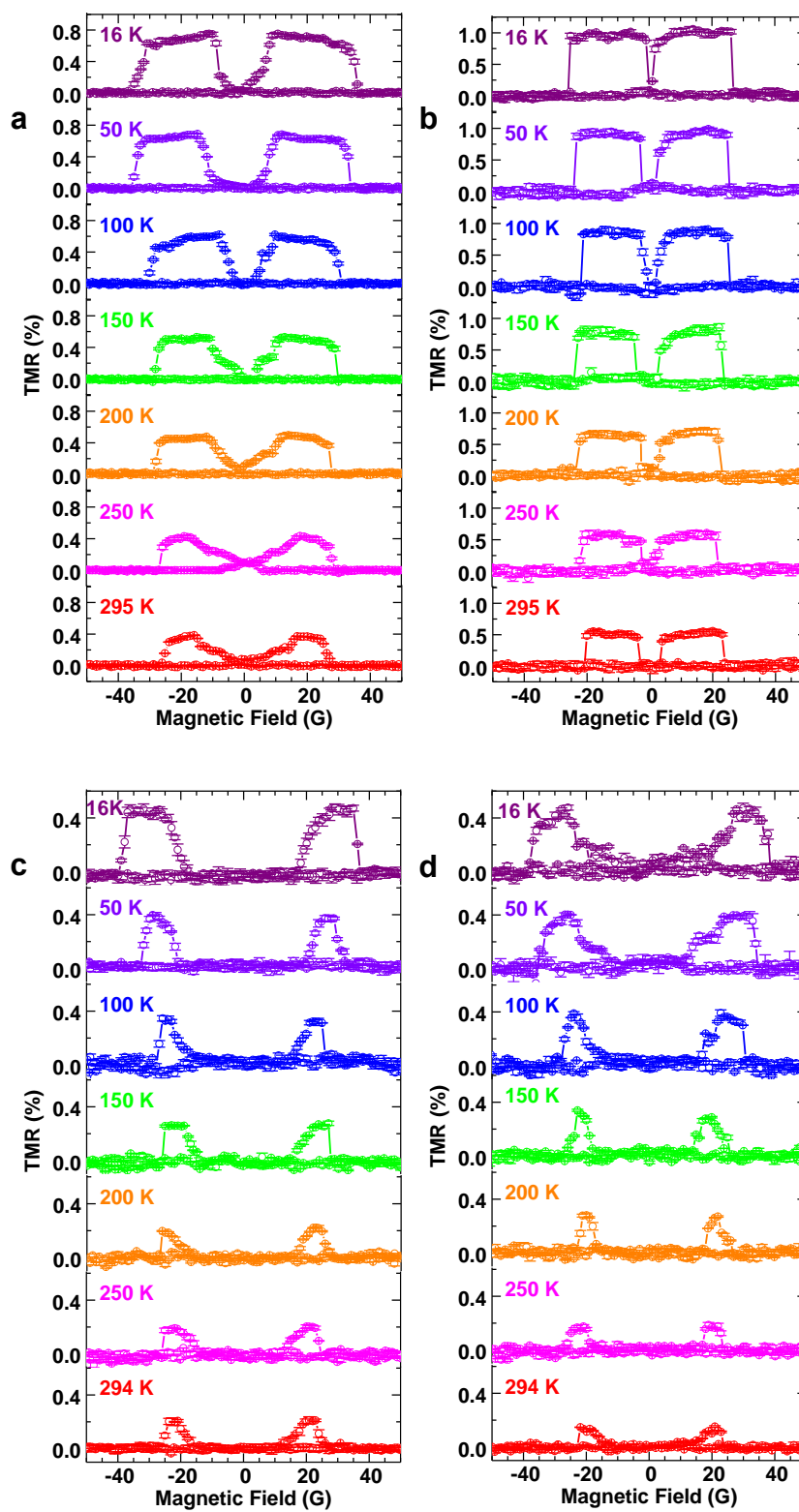


**Figure 4.6.** Temperature dependent MR of a) MoS<sub>2</sub>, b) WS<sub>2</sub>, c) MoSe<sub>2</sub>, and d) WSe<sub>2</sub> spin valves measure at various temperatures.

The temperature dependence of MR in MTJs have been theorized in the past for  $\text{Al}_2\text{O}_3$  and MgO junctions. Shang *et al* used Bloch's law  $P = P_0 (1 - \alpha T^{3/2})$  to describe the temperature dependence spin polarization<sup>153</sup>. In the assumption that  $P = P_1 = P_2$ , MR versus temperature plot can be fitted for  $\alpha$ , which is an important parameter that is associated with junction quality. On the other hand, Zhang *et al* derived equations based on 2D spin wave in the MTJs<sup>154</sup>, which a cut-off energy  $E_c$  was related to spin-coherent length. The anti-parallel and parallel resistance in a tunneling junction can be expressed as:

$$R_{AP,P}(T, 0) = R_{AP,P}(0,0) \left[ 1 + Q\beta_{AP,P} \ln\left(\frac{k_B T}{E_c}\right) \right]$$

where  $R_{AP,P}(T, V)$  denotes the anti-parallel and parallel resistance at T K and V applied bias,  $Q$  is the probability of a magnon of tunneling, and  $\beta_{AP}$  or  $\beta_P$  are terms related to the spin and curie temperature of the ferromagnetic electrodes<sup>155</sup>. Combining the equation of the magnon model with the definition of TMR, yielding:

$$\text{TMR} = \left[ \frac{R_{AP}(0,0) \left[ 1 + Q\beta_P \ln\left(\frac{k_B T}{E_c}\right) \right]}{R_p(0,0) \left[ 1 + Q\beta_{AP} \ln\left(\frac{k_B T}{E_c}\right) \right]} - 1 \right] \times 100\%$$

The temperature dependence of  $\Delta R/R$  of monolayer  $\text{MX}_2$  spin valves were fitted using both spin polarization model for  $\alpha$  and magnon model for  $Q$  and  $E_c$ . Resistances of anti-parallel and parallel states at 16K were used as  $R(0,0)$ . Figure 4.7a shows the

temperature dependence of  $\Delta R/R$  for a MoS<sub>2</sub> spin valve (Device B). The red curve represents the fitting result using Spin polarization model and the blue curve represents the fitting using magnon model.  $\alpha = 1.01 \times 10^{-4}$ ,  $E_c = 1.15 \times 10^{-8}$ , and  $Q = 0.0156$  were extracted from the fitting. Spin polarization model yielded larger temperature dependence at elevated temperature whereas magnon model showed less temperature dependence at high temperature. Both of the model fit relatively well in MoS<sub>2</sub> spin valve. The value of  $\alpha$  extracted from the MoS<sub>2</sub> spin valve were similar to other MoS<sub>2</sub> spin valve reports, but larger than classical MTJs which uses MgO or Al-O as spacer layers. Larger  $\alpha$  value indicates less ideal interface between the ferromagnetic electrodes and MX<sub>2</sub>. This can be caused by either transfer process during fabrication, or the oxidation of Py electrodes.  $Q$  value extracted from the fitting are similar to MgO junctions as reported by Drewello<sup>155</sup>. However, the  $E_c$  extracted from  $\Delta R/R$  vs T is to be significant lower, which indicates either low coherence length or anisotropy at FM-MX<sub>2</sub> interface. In WS<sub>2</sub> junctions shown in Figure 4.7b,  $\alpha = 9.73 \times 10^{-5}$ ,  $E_c = 2.83 \times 10^{-3}$ , and  $Q = 0.08$ . This time,  $E_c$  of WS<sub>2</sub> higher than  $E_c$  of MoS<sub>2</sub> spin valve, which suggest the better quality of WS<sub>2</sub> junctions.  $\Delta R/R$  vs T of MoSe<sub>2</sub> and WSe<sub>2</sub> spin valves are shown in Fig 5c and 5d respectively.  $\alpha = 1.17 \times 10^{-4}$ ,  $E_c = 2.20 \times 10^{-2}$ , and  $Q = 6.79 \times 10^{-3}$  are extracted from MoSe<sub>2</sub> spin valves and  $\alpha = 1.39$

$\times 10^{-5}$ ,  $E_c = 6.53 \times 10^{-3}$ , and  $Q = 0.25$ . are extracted from WSe<sub>2</sub> spin valves. Overall, Spin polarization model seems to fit better for tungsten-dichalcogenides based spin valves and Drewello's model fits better for molybdenum- dichalcogenides based spin valves. This may indicate the possibility of different kinds of spin mechanism in MX<sub>2</sub> junctions.

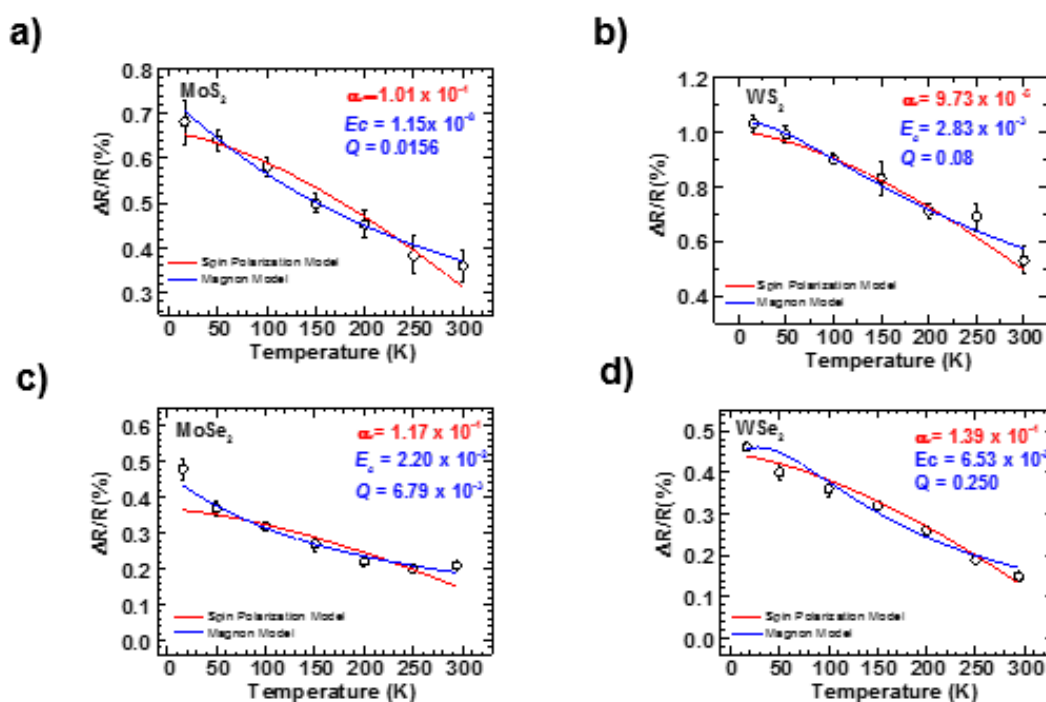


**Figure 4.7.** Temperature dependence tunneling magnetoresistance of a) MoS<sub>2</sub> spin valve (Device B), b) WS<sub>2</sub> spin valve (Device E), c) MoSe<sub>2</sub> spin valve (Device K), d) WSe<sub>2</sub> spin valve (Device O).

The summary of monolayer MX<sub>2</sub> spin valves are Figures 4.8a and 4.8b for room temperature and 16K respectively. In room temperature monolayer TMDC spin valves,

only monolayer WS<sub>2</sub> was reported to show room temperature TMR<sup>156</sup>. In low temperature studies, previously reported TMR value were 0.4% for MoS<sub>2</sub> at 10K and 0.47% for WS<sub>2</sub> at 4.2 K. Our study has demonstrated room temperature spin valve effect for MoS<sub>2</sub>, WS<sub>2</sub>, MoSe<sub>2</sub>, and WSe<sub>2</sub>, and has largest TMR values reported so far.

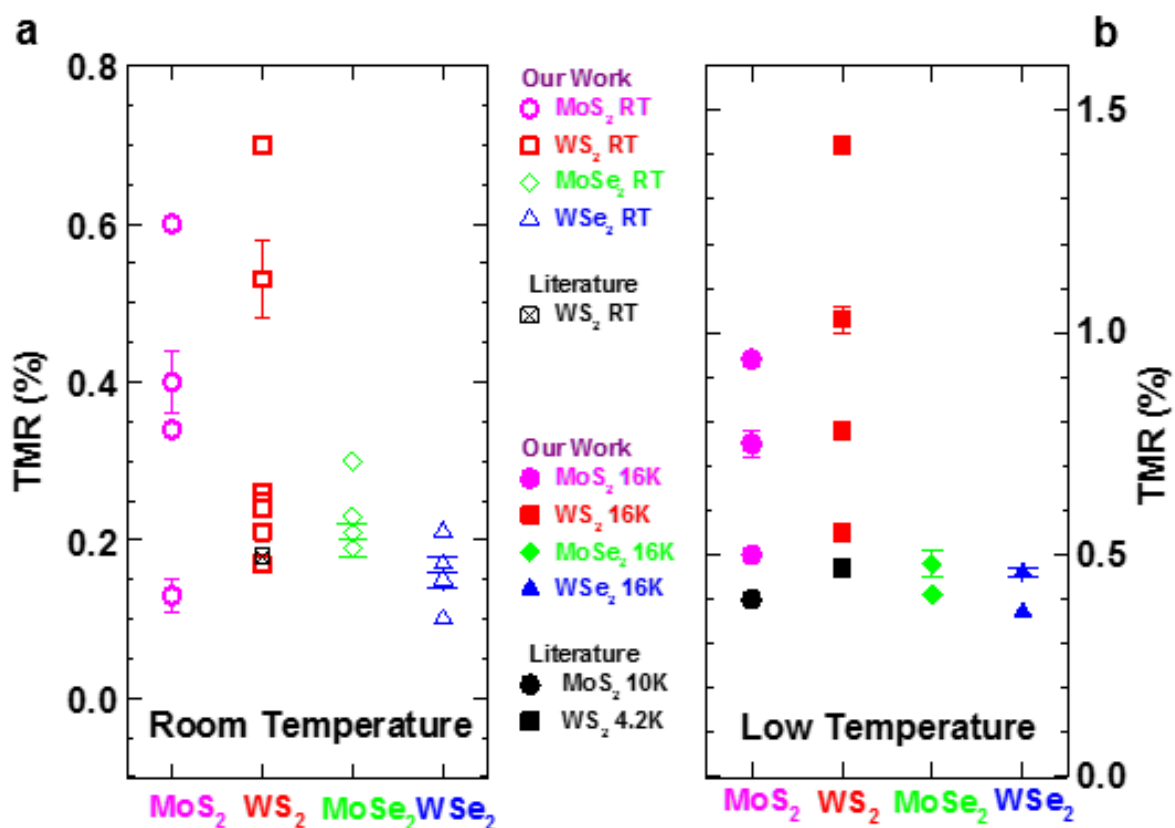


**Figure 4.8.** Summary of tunneling magnetoresistance of all MX<sub>2</sub> spin valves. a) Room temperature (RT) tunneling magnetoresistance of MX<sub>2</sub> spin valves. b) Low temperature tunneling magnetoresistance of MX<sub>2</sub> spin valves.

### **4.3.3 Annealing Effect in MX<sub>2</sub> Spin Valves**

In classical MTJs using MgO as tunnel barrier, annealing proves to be very effective in optimizing the TMR ratio<sup>157</sup>. Although in this study, MX<sub>2</sub> spin valves are not epitaxially grown on FM electrodes, annealing could remove unwanted contaminants at the FM/MX<sub>2</sub> interface as well as possibly reveal otherwise unknown properties, leading to increased MR ratio. MX<sub>2</sub> spin valves were annealed in vacuum for 30 m at 100°C or 200°C after fabrication of top Co/Au electrodes. A list of fabricated annealed MX<sub>2</sub> spin valves and their corresponding MR values is shown in Table IV. Figure 4.9a shows the MR of a MoS<sub>2</sub> spin valve (Device AG) annealed at 100°C and  $\Delta R/R = 0.59\%$  was measured. The device is then annealed again at 200°C for 30 m, and  $\Delta R/R$  was decreased from 0.59% to 0.51%. The magnetoresistance of the MoSe<sub>2</sub> spin valve (Device AM) with annealing process during fabrication was shown in Figure 4.9b and the measured  $\Delta R/R$  ratio was 0.44%. It is interesting to point out that for the MoSe<sub>2</sub> spin valve annealed at 100°C, the MR ratio were considerably higher than the MoSe<sub>2</sub> spin valves fabricated without annealing process. The annealing study of MX<sub>2</sub> spin valves are summarized in Figure 4.9c. The MR were measured at room temperature. The horizontal axis shows the annealing temperature and the vertical axis represents the measured MR ratio. For the MX<sub>2</sub> spin valves fabricated without the

annealing process, MoS<sub>2</sub> spin valve shows  $\Delta R/R$  ratio of 0.13% - 0.6%; WS<sub>2</sub> spin valve shows  $\Delta R/R$  ratio of 0.17% - 0.7%; MoSe<sub>2</sub> spin valve shows  $\Delta R/R$  ratio of 0.19%, - 0.3%; finally, WSe<sub>2</sub> spin valves shows TMR ratio of 0.1% - 0.21%. For the spin valves fabricated with annealing process at 100°C, MoS<sub>2</sub> spin valve showed  $\Delta R/R$  ratio of 0.11% - 0.59%; WS<sub>2</sub> spin valve showed  $\Delta R/R$  ratio of 0.09%; MoSe<sub>2</sub> spin valve showed 0.44%. For the spin valves fabricated with annealing process at 200°C, MoS<sub>2</sub> spin valves showed  $\Delta R/R$  ratio of 0.10% - 0.5%; WS<sub>2</sub> spin valves showed  $\Delta R/R$  ratio of 0.15% - 0.33%; WSe<sub>2</sub> spin valve showed  $\Delta R/R$  ratio of 0.26% and 0.31%. Overall, we did not observe a significant effect from these annealing conditions for MoS<sub>2</sub>, WS<sub>2</sub>, and WSe<sub>2</sub> spin valves. In MoSe<sub>2</sub> spin valves, the junction quality may have been improved which led to higher MR. Longer annealing time or higher temperature may be required to observe a significant change in device behavior as Asshoff *et al* annealed graphene spin valves at 300°C up to 10h.<sup>158</sup>

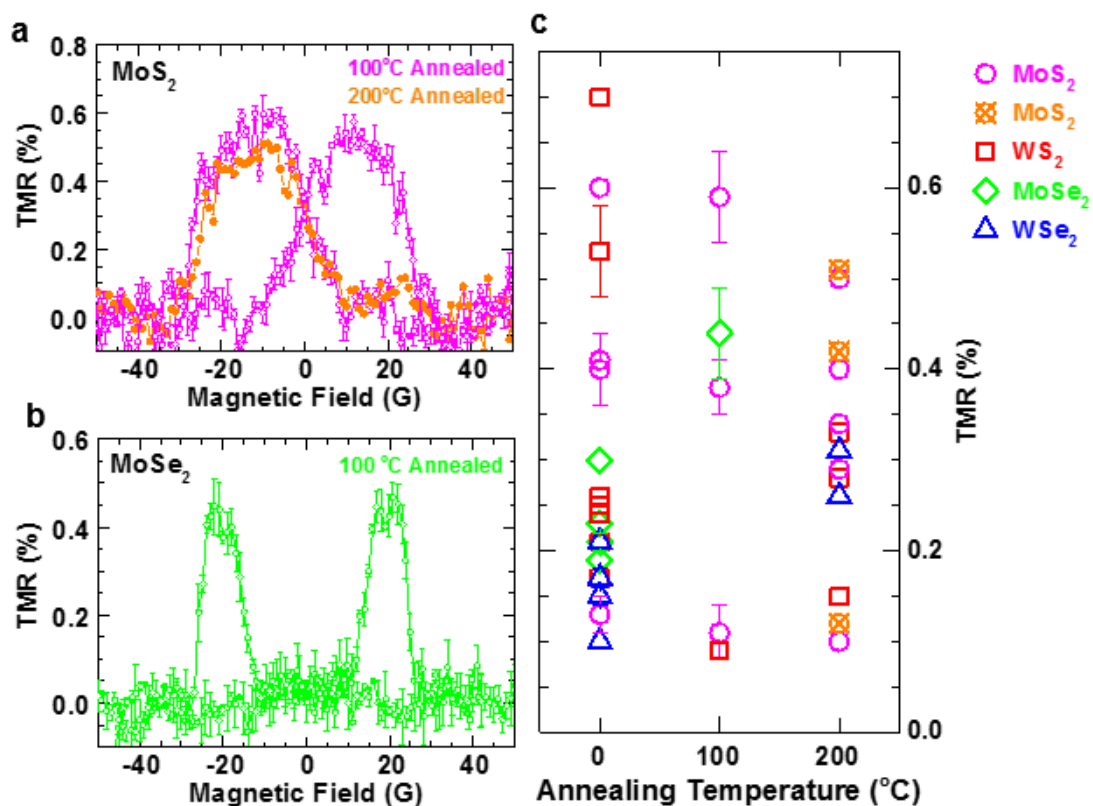


**Figure 4.9.** Annealing effect on MX<sub>2</sub> spin valves. (a) Tunneling magnetoresistance of annealed MoS<sub>2</sub> spin valve (Device AG) at room temperature. (b) Tunneling magnetoresistance monolayer MoSe<sub>2</sub> spin valve (Device AM) at room temperature. (c) Summary of annealing effect on room-temperature tunneling magnetoresistance of monolayer MoS<sub>2</sub>, WS<sub>2</sub>, MoSe<sub>2</sub>, and WSe<sub>2</sub> spin valves.

**Table IV.** List of Annealed TMDC Spin Valves.

<b>Device Number</b>	<b>Spacer layer</b>	<b>Number of Layers</b>	<b>Annealed</b>	<b>Annealing Temperature (°C)</b>	<b>TMR at Room-temperature</b>
AA	MoS <sub>2</sub>	Monolayer	Y	200	~0.34%
AB	MoS <sub>2</sub>	Monolayer	Y	200	~0.10%
AC	MoS <sub>2</sub>	Monolayer	Y	200	~0.40%
AD	MoS <sub>2</sub>	Monolayer	Y	200	~0.29%
AE	MoS <sub>2</sub>	Monolayer	Y	200	~0.50%
AF1	MoS <sub>2</sub>	Monolayer	Y	100	0.38±0.03%
AF2	MoS <sub>2</sub>	Monolayer	Y	100 + 200	~0.42%
AG1	MoS <sub>2</sub>	Monolayer	Y	100	0.59±0.05%
AG2	MoS <sub>2</sub>	Monolayer	Y	100 + 200	~0.51%
AH1	MoS <sub>2</sub>	Monolayer	Y	100	0.11±0.03%
AH2	MoS <sub>2</sub>	Monolayer	Y	100 + 200	~0.12%
AI	WS <sub>2</sub>	Monolayer	Y	200	~0.15%
AJ	WS <sub>2</sub>	Monolayer	Y	200	~0.28%
AK	WS <sub>2</sub>	Monolayer	Y	200	~0.33%
AL	WS <sub>2</sub>	Monolayer	Y	100	~0.09%
AM	MoSe <sub>2</sub>	Monolayer	Y	100	0.44±0.05%
AN	WSe <sub>2</sub>	Monolayer	Y	200	~0.31%
AO	WSe <sub>2</sub>	Monolayer	Y	200	~0.26%

#### **4.3.4 Layer Dependent TMR of MX<sub>2</sub> Spin Valves**

To better understand the physics of MX<sub>2</sub> spin valves, the layer dependence properties of WS<sub>2</sub> spin valve were investigated. Table V summarizes the list of fabricated multilayer devices. The room temperature MR of a tri-layer device (Device MC) is shown in Figure 4.10a. The MR curve is symmetric and showing MR ratio of 0.48%. The red curve represents MR measurements from negative magnetic field and the blue curve represents MR curve measured from positive to negative magnetic field. The magnetoresistance of a multilayer ( $n \geq 4$ ) layers device (Device MD) at room temperature and 16K is shown in Figure 4.10b. The red curve represents MR measurements at room temperature (294K) and the blue curve represents MR curve measured at 16K. The measured TMR ratio is 0.58% at 294K and 0.88% at 16K. The layer dependence properties of WS<sub>2</sub> spin valve is summarized in Figure 4.10c, where the horizontal axis represents number of layers and the vertical axis shows the TMR ratio of WS<sub>2</sub> spin valves. In monolayer WS<sub>2</sub> spin valves, the range of TMR ratio ranges from 0.17% to 0.7%. Bi-layer, tri-layer, and multi-layer WS<sub>2</sub> spin valve showed TMR ratio of 0.28%, 0.42% to 0.48%, and 0.58% respectively. TMR at 16K for multi-layer WS<sub>2</sub> device shows 0.88%. In our study, we did not observe a correlation between MX<sub>2</sub> thickness and MR. Density functional

theory calculation report<sup>91 159</sup> suggest that the MR response is more dependent on the spin polarization at the interface, in contrast to epitaxial junction such as in MgO<sup>157, 160</sup>, in which the thickness of the spacer layer also plays a significant role. This result suggests that the TMR value depends less on the thickness, but rather dominated by interface cleanness. In device MA and MB, the MR ratio of these spin valves are negative. In this case, the spin polarization is dependent on the majority or minority carriers. In monolayer spin valves, the single MX<sub>2</sub> layer can only conform to FM electrode; while in multi-layer MX<sub>2</sub> spin valve, the layers may electronically ‘split’ and conform to each FM electrodes, which causes the MR to become negative. Similar phenomenon was also observed by Asshoff *et al.*<sup>158</sup> In their studies, graphene is n-doped and p-doped when in contact with Co and Py, which lead to positive TMR at monolayers and negative TMR with  $n > 2$  layers.

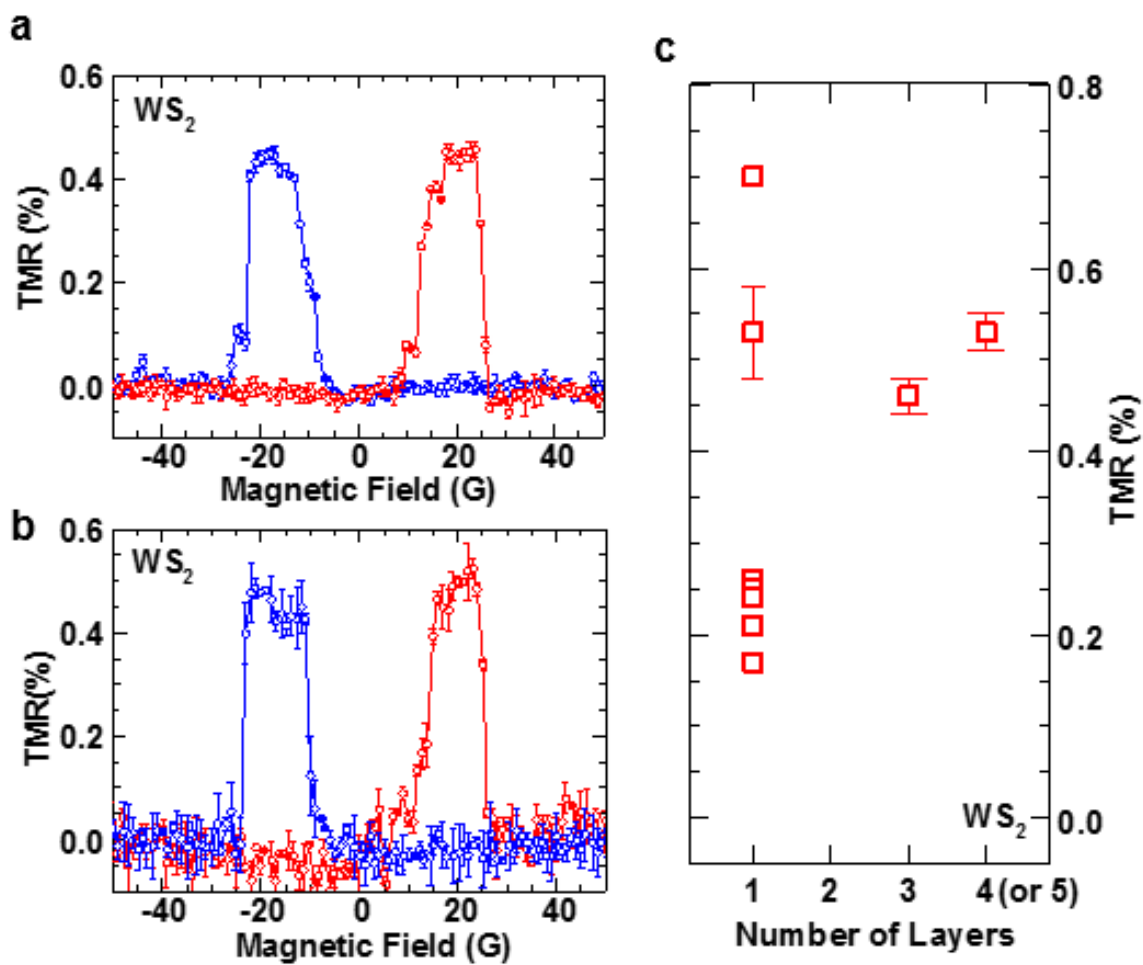


**Figure 4.10.** Multilayer MX<sub>2</sub> spin valves. a) Magnetoresistance of a trilayer WS<sub>2</sub> (Device MC) spin valve shown in a. c) Magnetoresistance of multilayer WS<sub>2</sub> (Device MD). c) Layer dependence of WS<sub>2</sub> spin valves at room temperature

**Table V.** List of Multi-Layered TMDC Spin Valves.

Device Number	Spacer layer	Number of Layers	Annealed	Annealing Temperature (°C)	TMR at Room-temperature	TMR at ~16K
MA	WS <sub>2</sub>	Bilayer	N	N/A	~ -0.28%	
MB	WS <sub>2</sub>	Trilayer	N	N/A	~ -0.42%	
MC	WS <sub>2</sub>	Trilayer	N	N/A	~0.48%	
MD	WS <sub>2</sub>	4-5 Layers	N	N/A	0.58±0.02%	0.88±0.02%

#### **4.3.5 Antiferromagnetic Pinned MX<sub>2</sub> Spin Valves**

So far, we have demonstrated spin valve based on MX<sub>2</sub> as a spacer layer. However, for practical applications such as conventional hard drives or other memory devices, a few other parameters must be addressed. First, it is common for one of the ferromagnetic layers is often exchange-biased with an antiferromagnetic layer for better switching operations. An exchange-biased WS<sub>2</sub> spin valve was fabricated on SiO<sub>2</sub>/Si substrates with Au/Co/WS<sub>2</sub>/Py/PtMn structure shown in Figure 4.11a. The lead contacts were deposited using Au/Ti. The magnetoresistance of the exchange-biased WS<sub>2</sub> spin valve is measured at both room temperature and 16K and plotted in Figure 4.11b (Device T). The horizontal axis represents external magnetic field and the vertical axis represents MR ratio. Asymmetrical shape in magnetoresistance curve was observed, indicating the coercivity of

Py layer was shifted, and TMR ratio measured were 0.21% and 0.38% at room temperature and 16K respectively. Furthermore, we also studied the TMR response with respect to applied bias.  $\text{MX}_2$  spin valves were measured using different magnitude of currents. To avoid device degradation, the junction current is kept within  $10\mu\text{A}$ . Figure 4.12a shows the bias behavior of a  $\text{MoS}_2$  spin valve measured at room temperature. TMR value up to 0.12% was found for  $1\mu\text{A}$  junction current, while at  $10\mu\text{A}$ , the TMR value reduced to 0.11%. The bias dependence response of a few  $\text{MX}_2$  spin valves were plotted in Figure 4.12b, showing weak bias dependence at both room temperature and 16K. The MR ratio of bias dependent properties is summarized in Table VI.

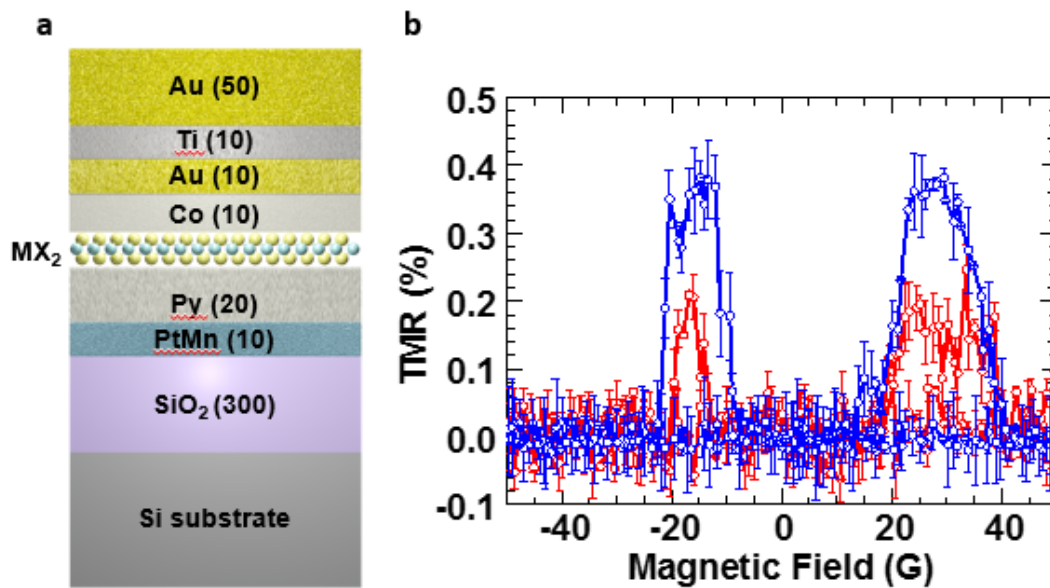


**Figure 4.11.** Exchange biased pinned WS<sub>2</sub> spin valve. a) A cross-sectional view of of WS<sub>2</sub> spin valve with PtMn antiferromagnetic layer pinned to Py layer. b) Magnetoresistance of exchange bias pinned WS<sub>2</sub> (Device T) spin valve.

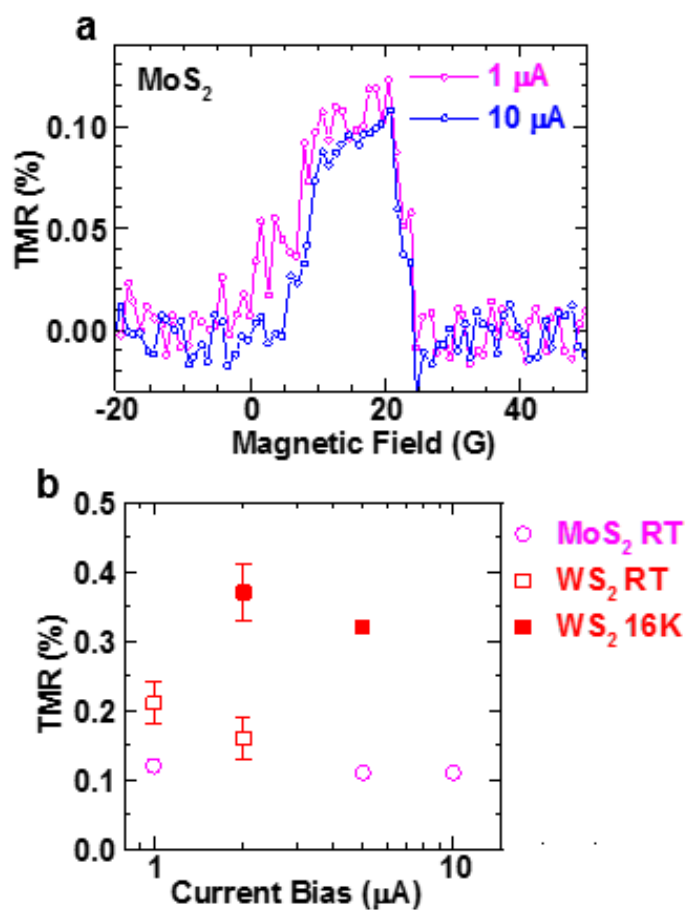


**Figure 4.12.** Bias dependent tunneling magnetoresistance. (a) Room-temperature tunneling magnetoresistance of a MoS<sub>2</sub> spin valve (Device AH2) with bias of 1 mA (red) and 10 mA (blue). (b) Summary tunneling magnetoresistance under different biases for a MoS<sub>2</sub> spin valve (Device AH2) at room temperature (open pink circle) and a WS<sub>2</sub> spin valve (Device T) at room temperature (solid red square) and at 16 K (open red square).

**Table VI.** Bias Dependent Measurement of TMDC Spin Valves.

Device Number	Spacer layer	Number of Layers	Bias Current ( $\mu\text{A}$ )	TMR at Room-temperature	TMR at ~16K
AH2	MoS <sub>2</sub>	Monolayer	1	0.11 $\pm$ 0.03%	
			1	~0.12%	
			5	~0.11%	
			10	~0.11%	
T	WS <sub>2</sub>	Monolayer	1	~0.21%	
			5		~0.34%
			2	0.21 $\pm$ 0.03%	
			2		0.38 $\pm$ 0.04%

#### **4.3.6 Anisotropy of MX<sub>2</sub> Spin Valves**

Due to the shape of the ferromagnetic metal electrodes, the coercivity of Py and Co varies depending on the direction of applied magnetic field. Co and Py electrodes experiences a higher coercivity when the magnetic field is parallel to the ferromagnetic metal bars, and smaller coercivity when the magnetic field is at an angle with the ferromagnetic metals. Figure 4.13a shows the TMR response of a WS<sub>2</sub> spin valve (Device MD) measured at 16K with different magnetic field directions. The blue curve corresponds to the TMR response with Co parallel to magnetic field, where as the pink curve

corresponds to the response with Co perpendicular to magnetic field. In both curves, the TMR was found to be  $\sim 0.8\%$  but with distinct difference in the MR shape. Figure 4.13b shows the TMR response of the same  $\text{WS}_2$  spin valve measured at room temperature. The red, green, orange curves represents the TMR curve with Co at  $0^\circ$ ,  $90^\circ$ , and  $45^\circ$  angle with respect to applied magnetic field. The TMR response with Co parallel to magnetic field is the widest owing to larger coercivity of Co at  $\sim 40$  gauss and smaller coercivity of Py at  $\sim 5$  gauss.

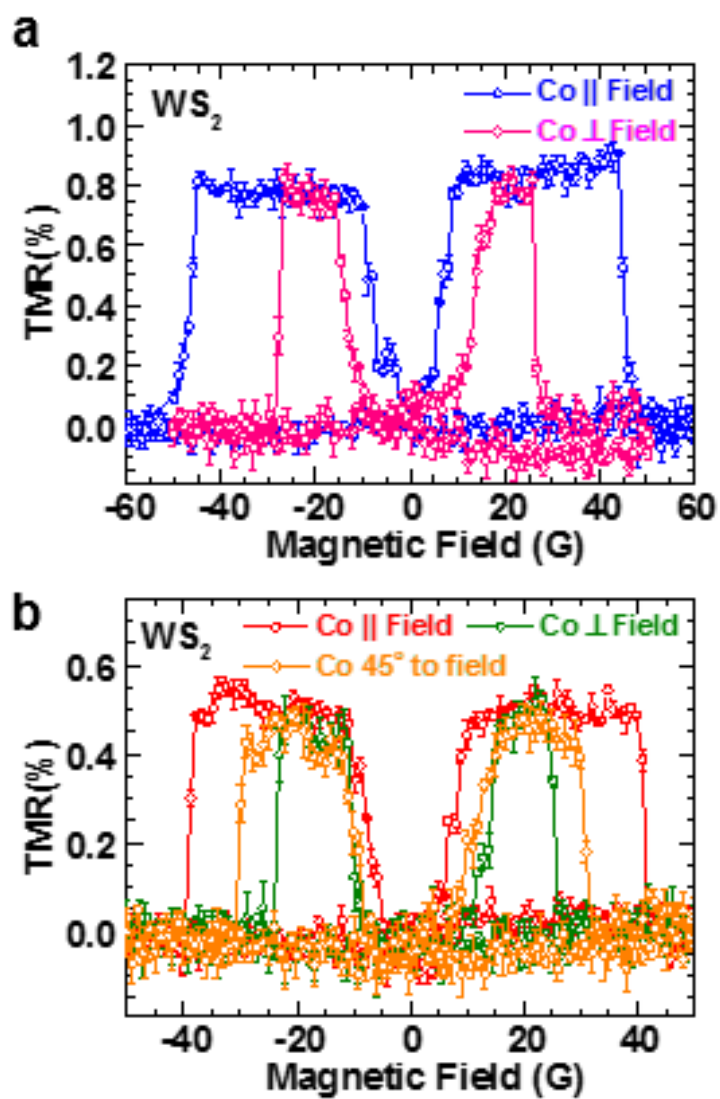


**Figure 4.13.** Anisotropy of WS<sub>2</sub> spin valve (Device MD) at a) 16K. b) room temperature

### **4.3.7 Life-Time of MX<sub>2</sub> Spin Valves**

For MX<sub>2</sub> spin valves to be implemented in modern memory devices, the lifetime of MX<sub>2</sub> spin valves should be reasonably durable. The aging effect of monolayer MX<sub>2</sub> spin valves were studied in two aspects, the number of measurements, which is related to the number of write times and number of days in ambient environment, which determines the stability of MX<sub>2</sub> spin valves. These results are shown in Figure 4.14. Figure 4.14a shows the TMR of MX<sub>2</sub> spin valves in relation to the number of measurements. It took a few hundred (the number depends on the magnetic field scanning step size) of single I-V measurements across the spin valve MX<sub>2</sub> junction to complete one TMR measurement in order to obtain the TMR ratio. Hence in Figure 4.14a the first data point of each spin valve device starts at a few hundred instead of 1. In all MX<sub>2</sub> spin valve studied, we did not observe a significant change in MR ratio with respect to measurement count. MoS<sub>2</sub> junctions remained ~0.4% MR after 10<sup>4</sup> times I-V scans. WS<sub>2</sub> junctions decreased from ~0.7% to ~0.5% after 10<sup>4</sup> measurements. MoSe<sub>2</sub> junctions, on the other hand, decrease from ~0.2% to ~0.18% after 10<sup>4</sup> measurements. Figure 4.14b shows the device performance after days in ambient environment. The MR shows no degradation except for a decrease in WSe<sub>2</sub> junctions. The fact that these devices do not have passivation layer

indicates good stability of monolayer MX<sub>2</sub> crystals and should be considered for future device applications.

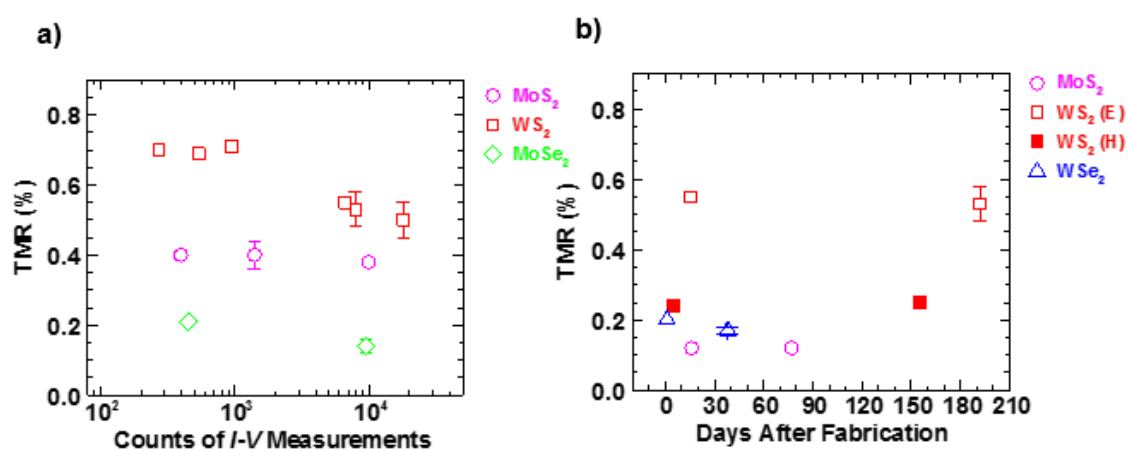


**Figure 4.14.** Aging effect of MX<sub>2</sub> spin valves. (a) Aging effect of MX<sub>2</sub> spin valves by number of single I-V measurements across the MX<sub>2</sub> junction of MoS<sub>2</sub> spin valve (Device B, pink circle), WS<sub>2</sub> spin valve (Device E, red square), and MoSe<sub>2</sub> (Device K, green diamond). (b) Aging effect of MX<sub>2</sub> spin valves by days lapsed. (Device AH2, pink circle) (Device E, red open square) (Device H, red solid square) (Device P, blue triangle)

#### **4.4 Summary**

In conclusion, high quality  $\text{MX}_2$  monolayers were grown using CVD method.  $\text{MX}_2$  spin valves were fabricated using standard lithography tools and wet transfer method. The TMR ratios of  $\text{MX}_2$  were measured up to 1.42% at 16K and 0.7% at room temperature. The results also show good reproducibility. Additionally,  $\text{MX}_2$  spin valves were fabricated to study various properties. It is found that MR ratio in  $\text{MX}_2$  spin valves were heavily affected by junction interface quality, but at the same time can sustain large amount of measurements and stable in ambient conditions. We believe that  $\text{MX}_2$  should perform much better with direct growth on ferromagnetic metals and should be suitable for memory applications.

## Chapter 5

# FLEXIBLE SPIN VALVE BASED ON MONOLAYER TRANSITION-METAL DICHALCOGENIDE

### 5.1 Introduction

Flexible electronics refers to electronic devices that tolerates bending, and stretching, with ultimate goals to create wearable and foldable electronics. Flexible electronics have many potential applications including sensors, transistors, opto-electronics, and memory devices. Traditional thin film semiconductors materials such as GaAs and GaN as well as substrates such as Si and ITO (indium-tin-oxide) have poor mechanical properties and not suitable for flexible electronics. Tremendous amount of work has been dedicated to enable traditional semiconductor materials in modern flexible electronics<sup>161-163</sup>. Although insulating flexible substrates such as polyethylene naphthalate (PEN), polyethylene terephthalate (PET), polyimide (PI), and even paper<sup>164</sup> are readily available, finding suitable materials for flexible conductors and semiconductors are still a major challenge.

Memory applications based on magnetic tunnel junctions (MTJs) has been considered a promising storage element due to its low power consumption, high density, and durability. Nowadays, MgO is the most popular as spacer layer material in MTJs. High quality MgO can be directly grown epitaxially on ferromagnetic substrates by radio frequency (RF)

magnetron sputter or molecular beam epitaxy.<sup>28-29</sup> Additionally, coherent tunneling allows MgO based MTJs to reach a tunneling magnetoresistance (TMR) up to 604% at room temperature<sup>32</sup>. Although there has been success demonstration of flexible MgO MTJ<sup>165-166</sup> recently, unfortunately, the brittle nature of MgO is not suitable for flexible electronics, and thus additional fabrication process will be required such as transfer techniques or specially designed electrodes that would complicate the fabrication process and increase the production cost. Although other flexible spin valves were also being studied such as inorganic MTJ<sup>167-168</sup>, organic material based MTJs<sup>169-170</sup> as well as GMR spin valves<sup>171-174</sup>, the TMR ratios of these MTJs are not comparable to that of MgO MTJs.

Graphene, b-BN, and transition-metal dichalcogenides (TMDCs) are novel 2D materials that have been intensively researched due to their unique electrical and optical properties. One of the motivations for 2D materials research is their unique mechanical properties<sup>66, 175</sup>. Furthermore, the atomic thickness of 2D materials leads to better gate voltage modulation over the field effect transistor (FET) channel. This makes 2D materials a promising candidate for flexible electronics. In fact, all 2D material based flexible transistors have already been demonstrated with mobilities up to several tens of  $\text{cm}^2\text{V}^{-1}\text{s}^{-1}$ , high on-off ratio  $\sim 10^7$ , and up to 88% transparency.<sup>69, 176</sup>

2D materials are strong competitors for flexible spin valves. Theoretical calculations reveal graphene are a near perfect spin filter, which can reach MR up to 100%.<sup>75</sup> In recent years, many graphene spin valves have already been studied and demonstrated<sup>74, 76-83, 177</sup> with currently highest MR up to 12% at 15K.<sup>84</sup> Spin valves based on other 2D materials including h-BN<sup>85, 178</sup>, TMDCs<sup>90, 151, 179</sup>, black phosphorous<sup>87</sup>, and hybrid materials<sup>86, 91, 180</sup> have also been shown. Despite these results, there has been no experimental demonstration of flexible 2D spin valve. In this chapter, high quality large area single crystal MoS<sub>2</sub> and WS<sub>2</sub> were grown using CVD method. Flexible spin valve based on MoS<sub>2</sub> and WS<sub>2</sub> were fabricated and studied at various bending radius.

## **5.2 Experiment**

### Growth of Monolayer MoS<sub>2</sub> and WS<sub>2</sub>

Monolayer MoS<sub>2</sub>, WS<sub>2</sub> single crystals were grown on 300 nm SiO<sub>2</sub>/Si substrates using chemical vapor deposition (CVD). The substrates were cleaned with acetone, isopropyl alcohol (IPA), and deionized (DI) water, then dried with N<sub>2</sub> before loading into the quartz tube. Transition-metal tri-oxides (MoO<sub>3</sub>, WO<sub>3</sub>) and S powders were used as the source materials for TMDC nanosheet synthesis. MoS<sub>2</sub> monolayers growth were carried

out under vacuum of 9 Torr with a growth temperature of 875 °C for 10 minutes. WS<sub>2</sub> monolayers were grown under ambient pressure with a growth temperature of 1075°C for 120 minutes. 50 sccm and 100 sccm Ar gas flow were used for the synthesis of MoS<sub>2</sub> and WS<sub>2</sub> respectively. After growth, the furnace was cooled down naturally and the flow rate of Ar was increased to 500 sccm to prevent further deposition.

### Fabrication

The vertical TMDC spin valves were fabricated using Permalloy (Ni 80% Fe 20%), TMDC monolayer, and Co as bottom electrode, insulating layer, and top electrode, respectively. 20 nm of Py electrodes arrays were deposited on patterned Kapton substrates. The dimensions of Py bottom electrode arrays were designed to increase the transfer process success rate as shown in Figure 5.1a. Figure 5.1b shows as-grown MX<sub>2</sub> monolayers on SiO<sub>2</sub>/Si substrates were transferred onto the Kapton substrate with pre-deposited Py metal electrode arrays. First, the as-grown MX<sub>2</sub> monolayers were spin coated PMMA at 3000 rpm then baked at 180°C to remove the solvents. Then, the spin coated samples were dip into 10% HF solution for 20 minutes to etch away the SiO<sub>2</sub> layer. The PMMA-coated-MX<sub>2</sub>-monolayers were subsequently transferred to the substrates with Py electrodes, followed by a baking at 100°C for 20 minutes to remove water molecules. Finally, the

PMMA was removed with acetone, rinsed by DI water, and dried by N<sub>2</sub> gun. Then, 10 nm of Co and 10 nm Au contacts were deposition on top of the transferred MX<sub>2</sub> monolayers as shown in Figure 5.1c and d. The lead electrodes connecting to top and bottom ferromagnetic electrodes were subsequently fabricated using 10 nm Ti and 50 nm Au as shown in Figure 5.1e and f.

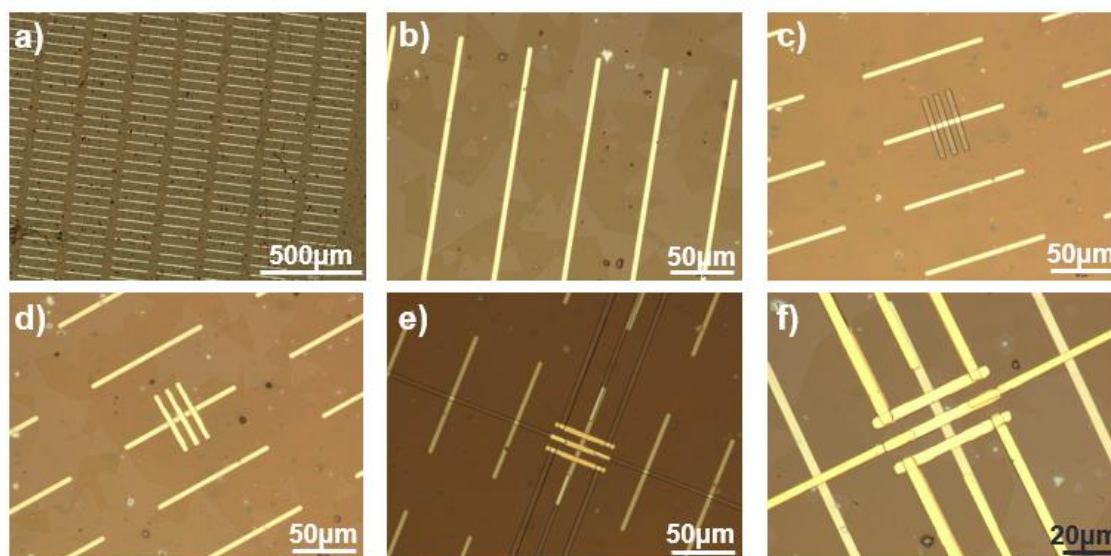


**Figure 5.1.** Fabrication of flexible MX<sub>2</sub> spin valve. a) OM images of patterned Py electrode on Kapton substrate. b) OM images of transferred monolayer MX<sub>2</sub> on top of Py electrodes. c) OM images of photolithography process of patterning top electrode. d) OM images of fabricated Co/Au top electrode. e) OM images of photolithography process of patterning lead contacts. f) OM images of a complete flexible MX<sub>2</sub> device.

## Measurement

Plastic bases of various bending radius were 3D printed. The fabricated MTJ devices were first mounted these bases then mounted to a home-built cryogenic measurement system equipped with Lakeshore EM4 electromagnet, Lakeshore 643 electromagnet power supply, Lakeshore 475 gauss meter as shown in Figure 5.2. The junction resistances versus applied magnetic field at room temperature. Keithley 6221 AC/DC current source meter and 2182A nano-voltmeter were used to supply current and measure the voltage drop across the junctions respectively. The junction IVs were measured several times at a single magnetic field point and IVs were linearly fitted to obtain the resistance value. Four-probe measurement method was employed to exclude the magnetoresistance from the Co and Py electrodes as well as the resistance from the Ti/Au leads.

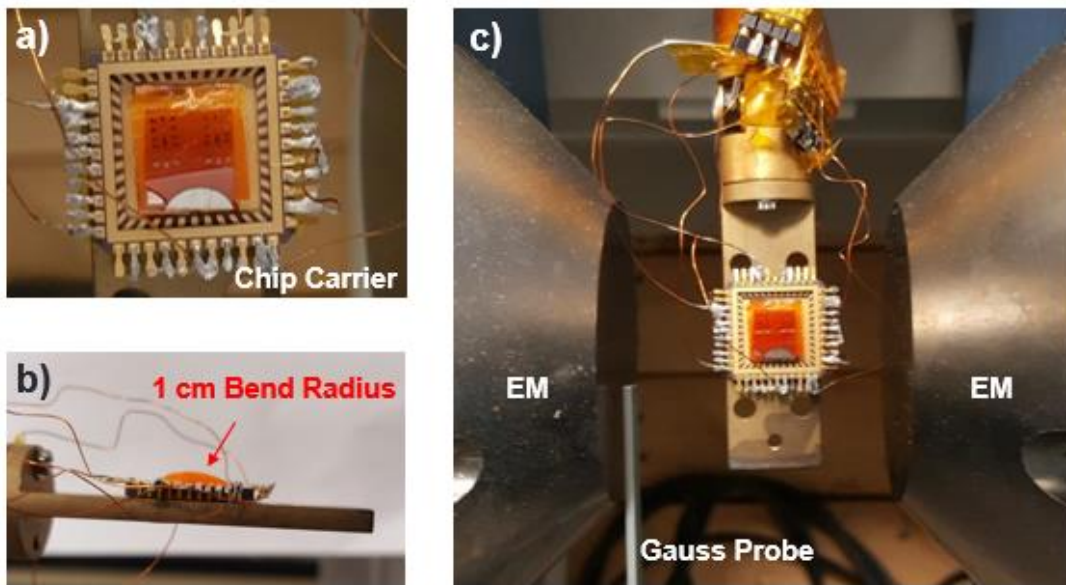


**Figure 5.2.** Measurement of flexible  $\text{MX}_2$  spin valve. a) Enlarged top view of measurement setup. The devices were mounted to 3D printed base then mounted to a chip carrier. Electrical connections were established by wire-bonding device contacts to leads of the chip carrier. b) Side view of measurement setup. Cu wires were soldered to the leads of chip carrier and connected to electrical ports of the measurement system c) Top view of measurement setup.

### **5.3 Results and Discussion**

After growth, as-grown monolayer MX<sub>2</sub> were characterized using the methods described in chapter 3 to confirm their monolayer thickness. The schematic of a MX<sub>2</sub> flexible spin valve is shown in Figure 5.3a, the vertical spin valve consist of Co/MX<sub>2</sub>/Py . An optical microscope image of three fabricated MoS<sub>2</sub> devices is shown in Figure 5.3b. Due to the structure of device and large area of as-grown monolayer MX<sub>2</sub>, typically more than one devices can be fabricated on a single MX<sub>2</sub> domain. The junctions are ~10 cm<sup>2</sup> in area and ~30Ω in resistance. The junction voltage-current (*I-V*) characteristics of fabricated flexible spin valves are linear and similar to non-flexible spin valves fabricated before in Chapter 4. This behavior can be attributed by hybridization of MX<sub>2</sub> and ferromagnetic contacts.<sup>90-91</sup> Using the four-probe measurement technique, MR measurements were performed on the MX<sub>2</sub> spin valves at room temperature. The junction resistance was measured from -50 Gauss to 50 Gauss. The magnetoresistance (MR) curve of flexible MoS<sub>2</sub> spin valve is shown in Figure 5.5 at different bending radius. MR is defined by  $\frac{\Delta R}{R} = \frac{R_{AP}-R_P}{R_P}$ , where R<sub>P</sub> denotes the junction resistance when both top and bottom ferromagnetic electrodes were aligned, and R<sub>AP</sub> represents the junction resistance when the two ferromagnetic contacts were antiparallel.

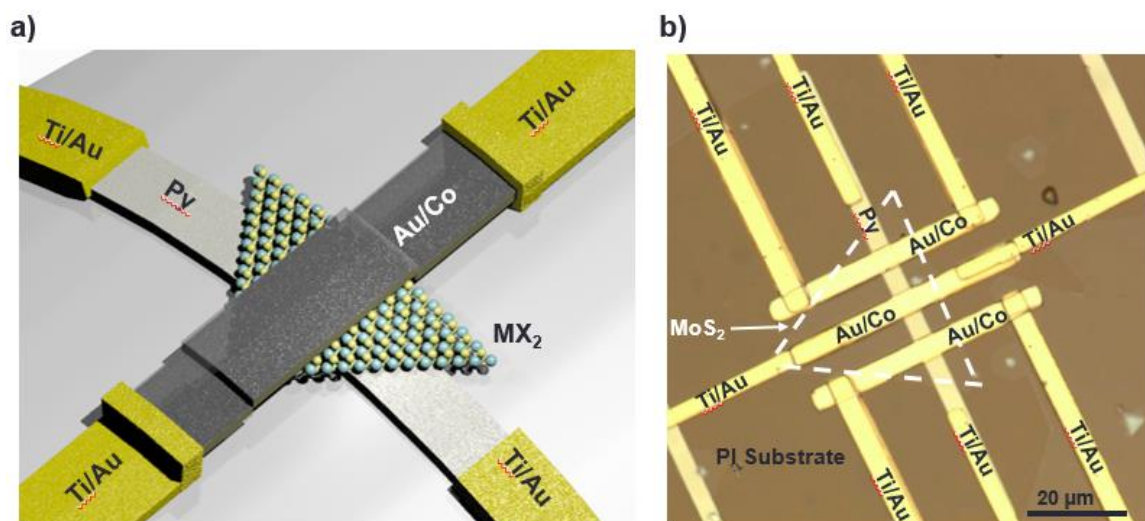


**Figure 5.3.** Device structure of flexible MX<sub>2</sub> spin valve. a) Schematic of a monolayer MX<sub>2</sub> flexible spin valve. b) Optical microscope image of three Co/MoS<sub>2</sub>/Py junctions fabricated on the same MoS<sub>2</sub> flake. Dashed white line is drawn to guide the shape of single crystal MoS<sub>2</sub>.

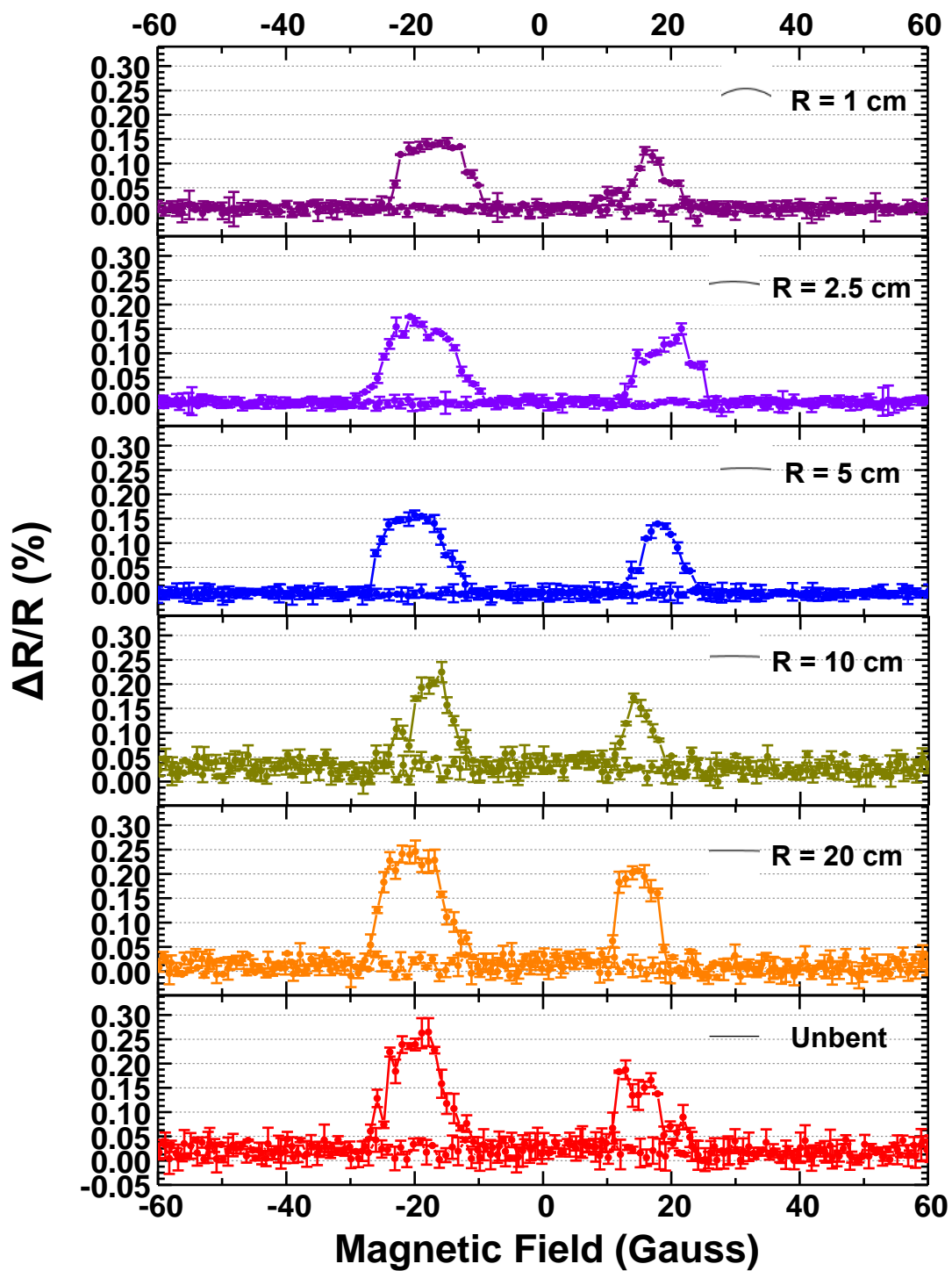
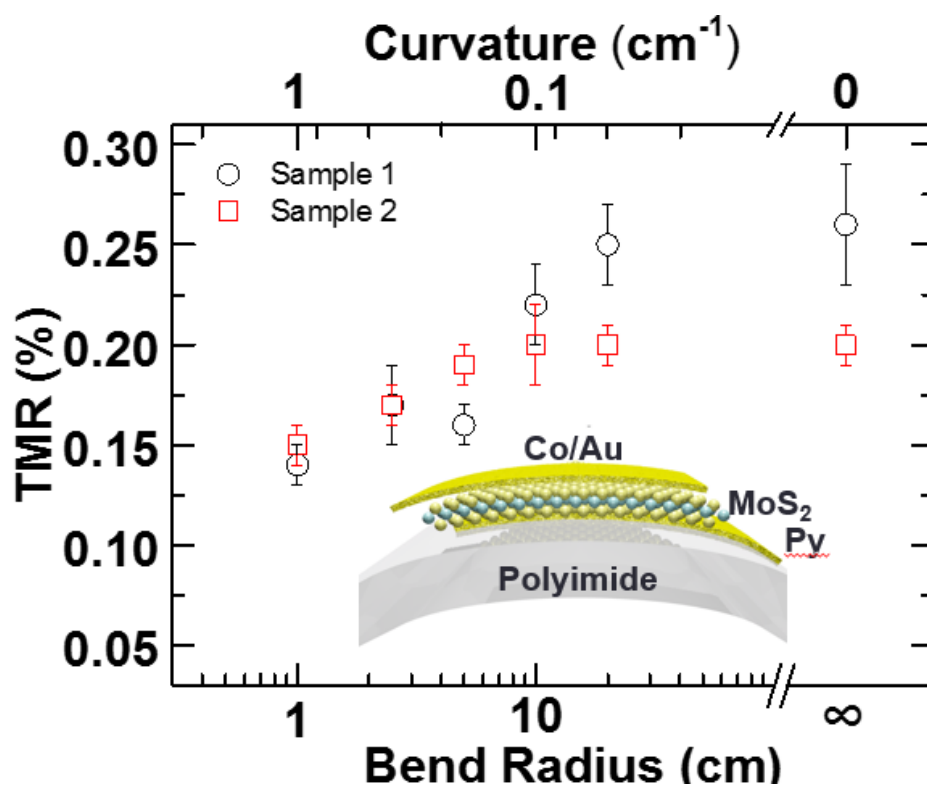


Figure 5.4. Magneto-resistance of flexible  $\text{MoS}_2$  spin valve at different bending radii.

The shape of the MR curves in Figure 5.4 resembles typical spin valve behavior. A “bump” in MR is observed when top and bottom ferromagnetic electrodes are anti-parallel aligned, and the junction has low resistance state when top and bottom ferromagnetic electrode are parallel aligned. Without any bending or external strain, the MoS<sub>2</sub> junction shows MR value of  $0.27 \pm 0.03\%$ . The MR value observed is in agreement with 2D spin valves fabricated with transfer process in literature, which is typically  $< 1\%$  at room temperature<sup>90, 151</sup>. With decreasing bending radius, the MR of flexible MoS<sub>2</sub> decrease slightly from  $0.25 \pm 0.02 \%$  at 20 cm bending radius,  $0.20 \pm 0.02 \%$  at 10 cm bending radius,  $0.15 \pm 0.01 \%$  at 5 cm bending radius,  $0.17 \pm 0.02 \%$  at 2.5 cm bending radius, and  $0.14 \pm 0.01 \%$  at 1 cm bending radius. The gradually decrease in MR could be attributed to junction quality degradation by many  $I$ - $V$  scans, which was a phenomenon observed previously and discussed in Chapter 4. Additionally, in a second flexible MoS<sub>2</sub> spin valve, a similar trend is observed, where with increasing bending, the MR ratio decreases gradually from 0.20% without bending to 0.15% at 1 cm bending radius. Figure 5.5 summarizes MR at various bend radius for MoS<sub>2</sub> spin valves. The top horizontal axis represents bending curvature, where  $C = 1/R$ , and the bottom horizontal axis represents the bending radius. Vertical axis shows the MR ratio of MoS<sub>2</sub> spin valves. The inset of Figure

5.5 shows a cross-sectional schematic of flexible MoS<sub>2</sub> spin valve. Although ~5 - 10% change in MR was observed during bending, MoS<sub>2</sub> spin valves were still operational after many measurements. These results not only displayed the durability of these spin valve devices, but also demonstrated the flexible nature of monolayer MoS<sub>2</sub>.



**Figure 5.5.** Bend radius dependent tunneling magnetoresistance of MoS<sub>2</sub> spin valves.

In previous studies described in Chapter 4, WS<sub>2</sub> spin valve showed the best performance in terms of TMR, possibly due to the crystallinity of WS<sub>2</sub> grown at high temperatures and growth setup. WS<sub>2</sub> flexible spin valves were also fabricated studied at various bend radius. The TMR of WS<sub>2</sub> spin valves were measured at room temperature and obtained from measuring the junction resistance with external magnetic field applied from -60 Gauss to 60 Gauss and vice-versa. Before each MR scan, a magnetic field of 1000 Gauss is used to align the Co and Py electrodes. A symmetric MR response with two distinct bumps were observed, indicating successful spin valve effect. Without bending, WS<sub>2</sub> flexible spin valve exhibits a TMR ratio of  $0.37 \pm 0.01$  %, higher than MoS<sub>2</sub> spin valves mentioned before. This further confirms the higher quality of WS<sub>2</sub> junctions. The decrease of junction resistance from ~60 Gauss to -20 Gauss can be attributed to the joule heating effect during initial measurements. The MR of WS<sub>2</sub> junctions at different bend radius were subsequently measured and shown in Figure 5.6.

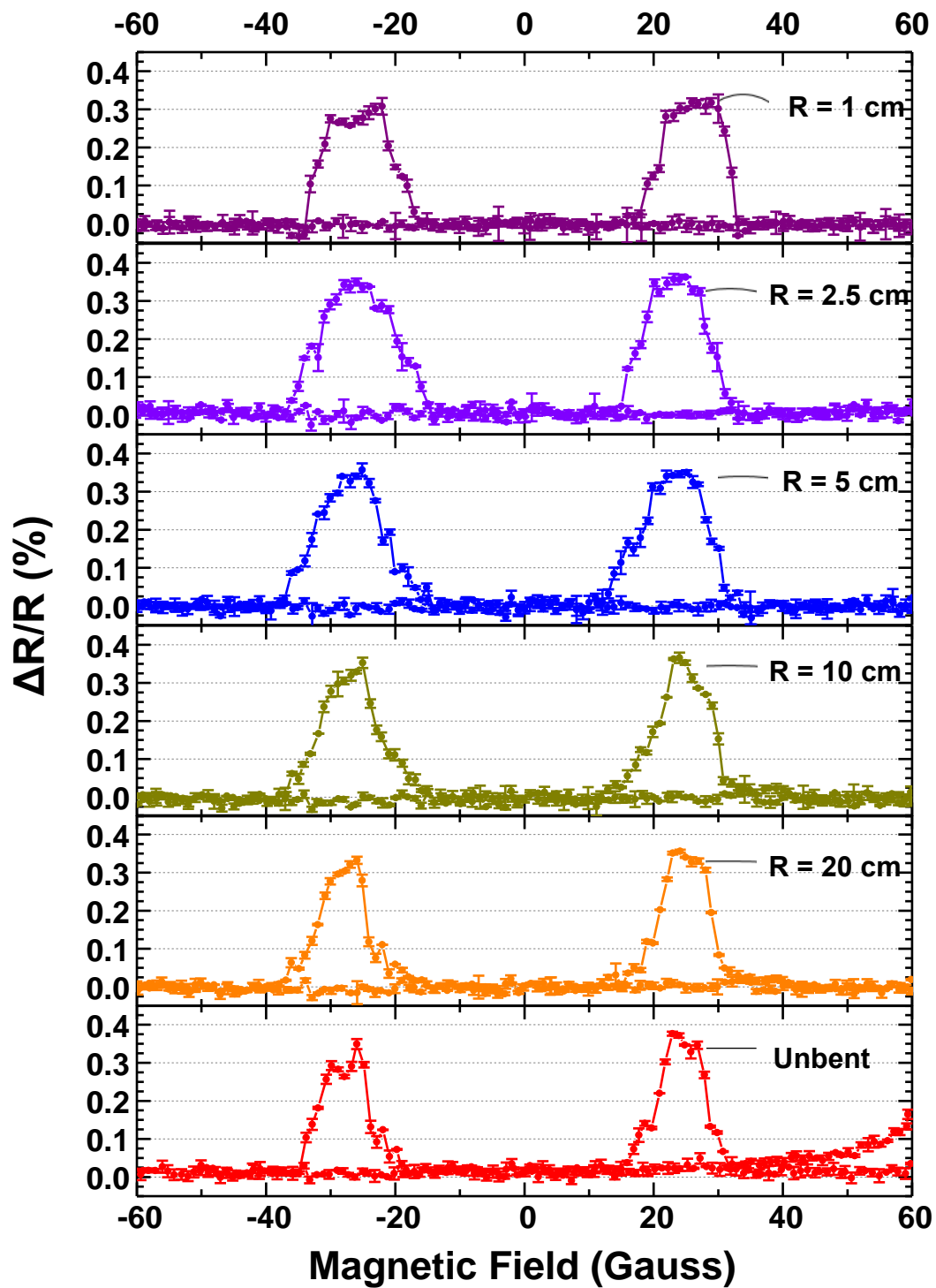
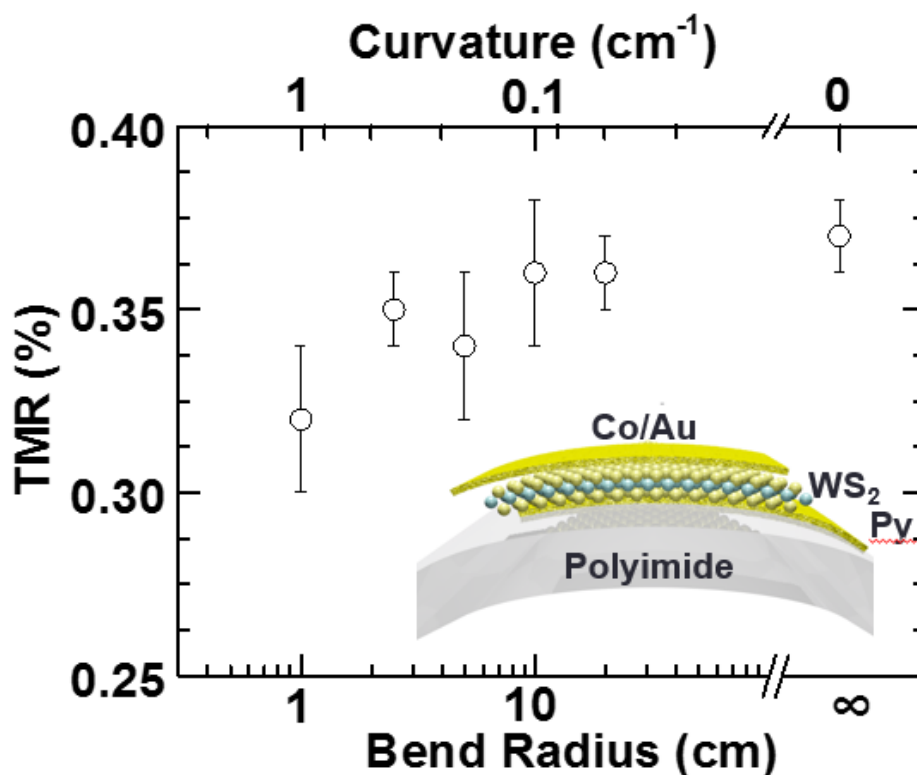


Figure 5.6. Magnetoresistance of WS<sub>2</sub> spin valves under various bending radii.

In WS<sub>2</sub> junctions, the bend radius did not have a significant effect in MR ratio compared to MoS<sub>2</sub> junctions, as the TMR ratios at different bending radii or curvatures are closely within error. The MR of flexible WS<sub>2</sub> junction is  $0.36 \pm 0.01$  %,  $0.36 \pm 0.02$  %,  $0.34 \pm 0.02$  %,  $0.35 \pm 0.01$  %,  $0.32 \pm 0.02$  % at 20 cm, 10 cm, 5 cm, 2.5 cm, and 1 cm bend radius respectively. Additionally, a light widening of the MR “bumps” is observed. This behavior originates from the coercivity change of ferromagnetic electrodes under external strain, which was also observed by Loong *et al* in flexible MgO spin valves<sup>166</sup>. Overall, WS<sub>2</sub> spin valves showed 4% TMR change at increased bending radius as shown in Figure 5.7 and shows superior performance compared to MoS<sub>2</sub> spin valves. Additionally, WS<sub>2</sub> spin valve also withstood several thousand I-V measurements, which further proves the robustness of MX<sub>2</sub> spin valves.



**Figure 5.7.** Bend radius dependent tunneling magnetoresistance of WS<sub>2</sub> spin valve.

#### **5.4 Summary and Perspective**

In summary, large-area single crystalline MoS<sub>2</sub> and WS<sub>2</sub> monolayers were grown using CVD. Flexible spin valves with MoS<sub>2</sub> and WS<sub>2</sub> spacer layers and Co and NiFe as top and bottom ferromagnetic layers were fabricated on polyimide substrates using photolithography and wet transfer method. The TMR ratios of flexible spin valves were measured at room temperature and under various bending radii. TMR ratios for the first

MoS<sub>2</sub> flexible spin valve were  $0.20 \pm 0.01$  % without bending, and  $0.15 \pm 0.01$  % at 1 cm bending radius. In the second MoS<sub>2</sub> flexible spin valve, TMR ratio of  $0.27 \pm 0.03$  % and  $0.14 \pm 0.01$  % were observed at no bending and at 1 cm bend radius, respectively. The room-temperature TMR of WS<sub>2</sub> flexible spin valve were  $0.37 \pm 0.01$  % without bending and  $0.32 \pm 0.02$  % at 1 cm bending radius. The results pave the way for flexible MX<sub>2</sub> spintronic devices. In the next step, recently reported ferromagnetic 2D materials such as Cr<sub>2</sub>Ge<sub>2</sub>Te<sub>6</sub><sup>181</sup>, CrI<sub>3</sub><sup>182-184</sup>, and VSe<sub>2</sub><sup>185</sup>, will be included in the spin valve fabrication as top and bottom ferromagnetic layers in order to form a spin valve composed of only three 2D monolayers. Furthermore, intrinsic MTJs composed of only CrI<sub>3</sub> layers have been demonstrated to show large TMR ratios<sup>186-187</sup>, due to sharp interfaces between the layers without any fabrication processes involved. which reveals the potential of ultra-high density information storage in 2D materials.

## CONCLUSIONS

The goal of this dissertation is to study the characteristics of two-dimensional transition-metal dichalcogenides (TMDC)  $\text{MX}_2$  ( $\text{M}=\text{Mo},\text{W}$ ,  $\text{X}=\text{S},\text{Se}$ ; four types of materials in total) monolayers as the spacer layers in magnetic tunneling junctions (MTJ) spin valves. There are a few major challenges for the scope of this study. First, high-quality large-area single crystal TMDC  $\text{MX}_2$  monolayers must be synthesized in a controlled manner. Mechanical exfoliation method cannot produce large enough monolayer  $\text{MX}_2$  for device fabrication. Chemical vapor deposition (CVD) process can produce high-quality large-scale single-crystalline TMDC  $\text{MX}_2$  monolayers and the as-grown  $\text{MX}_2$  monolayers typically share similar morphology in triangular shape and uniform thickness. Polycrystalline  $\text{MX}_2$  are easily grown; however, they are not suitable for this study. The ratio of TMR is strongly dependent on junction quality. The grain boundaries in polycrystalline  $\text{MX}_2$  leads to the significant reduction of TMR, due to the fact that the ferromagnetic metal- $\text{MX}_2$  interface does not retain their spin polarization. Through the growths of more than 2000 of  $\text{MX}_2$  samples, the growth parameters were optimized such as that large-scale single-crystalline  $\text{MX}_2$  monolayers up to 80  $\mu\text{m}$  was achieved. The largest single crystals grown  $\text{MX}_2$  were  $\sim 190 \mu\text{m}$ ,  $\sim 450 \mu\text{m}$ ,  $\sim 80 \mu\text{m}$ , and  $\sim 180 \mu\text{m}$  for  $\text{MoS}_2$ ,  $\text{WS}_2$ ,  $\text{MoSe}_2$ , and  $\text{WSe}_2$  respectively.

The second major challenge in this study is the spin valve fabrication process of the materials with a single molecular layer thick MX<sub>2</sub>. The fabrication was difficult due to the novelty of this research without established procedures. The optimization of fabrication process requires significant amount of time on fabrication of large quantity of devices. Over 200 MX<sub>2</sub> FET/Hall-bar devices and over 200 MX<sub>2</sub> spin valves were fabricated.

Characterization performed on as-grown MX<sub>2</sub> confirmed their high quality. The Raman spectra of MX<sub>2</sub> showed peak shifts with increasing layer thickness which can be used to identify monolayers. In MoS<sub>2</sub>, the difference between E<sub>2g</sub><sup>1</sup> and A<sub>1g</sub> peaks is ~19 cm<sup>-1</sup> at monolayers and ~27 cm<sup>-1</sup> at bulk thickness. Similarly in WS<sub>2</sub>, the peak difference is 62.05 cm<sup>-1</sup> and 64.43 cm<sup>-1</sup> at monolayer and multi-layer thickness respectively. The sharp PL peaks measured from MoS<sub>2</sub>, WS<sub>2</sub>, MoSe<sub>2</sub>, and WSe<sub>2</sub> shows they are of high crystallinity. Electrical characterizations show the field effect mobilities of monolayer MX<sub>2</sub> are up to  $6.7 \pm 0.2 \text{ cm}^2\text{V}^{-1}\text{s}^{-1}$ ,  $82 \pm 18 \text{ cm}^2\text{V}^{-1}\text{s}^{-1}$ ,  $297 \pm 45 \text{ cm}^2\text{V}^{-1}\text{s}^{-1}$ ,  $12 \pm 3 \text{ cm}^2\text{V}^{-1}\text{s}^{-1}$  for MoS<sub>2</sub>, WS<sub>2</sub>, MoSe<sub>2</sub>, and WSe<sub>2</sub> respectively. Furthermore, Hall Effect measurements, which excludes contact resistances, reveals MoS<sub>2</sub> and WS<sub>2</sub> have mobilities up to  $118 \pm 4 \text{ cm}^2\text{V}^{-1}\text{s}^{-1}$  and  $28 \pm 2 \text{ cm}^2\text{V}^{-1}\text{s}^{-1}$  respectively.

The measurements of TMR in spin valves with MX<sub>2</sub> (M=Mo,W, X=S,Se; four types

of materials in total) monolayers as spacer layers and Co and NiFe as top and bottom ferromagnetic layers were subsequently carried out. Largest TMR observed were 0.6%, 0.72%, 0.3%, and 0.19% at room temperature MoS<sub>2</sub>, WS<sub>2</sub>, MoSe<sub>2</sub>, and WSe<sub>2</sub> respectively. At 16K, due to reduced scattering, the TMR increased to 0.83%, 1.42%, 0.38%, and 0.4% for MoS<sub>2</sub>, WS<sub>2</sub>, MoSe<sub>2</sub>, and WSe<sub>2</sub> respectively. In addition, other properties in MX<sub>2</sub> spin valves were explored, including annealing effect, exchanged-bias effect, thickness dependence, magnetic anisotropy, and “aging effect”.

The flexible nature in monolayer MX<sub>2</sub> was utilized. Flexible MX<sub>2</sub> spin valves with with MS<sub>2</sub> (M=Mo and W; two types of materials in total) monolayer as spacer layer and Co and NiFe as top and bottom ferromagnetic layers were fabricated on polyimide substrates. The spin valves retain their TMR after external strain were applied at 1 cm bending radius. TMR ratios for a MoS<sub>2</sub> flexible spin valves were  $0.20 \pm 0.01$  % without external strain, and  $0.15 \pm 0.01$  % at 1 cm bending radius. In another MoS<sub>2</sub> flexible spin valve, TMR ratio of  $0.27 \pm 0.03$  % and  $0.14 \pm 0.01$  % were observed at no bending and at 1 cm bend radius respectively. Last, WS<sub>2</sub> flexible are studied.  $0.37 \pm 0.01$  % TMR are observed without bending and  $0.32 \pm 0.02$ % TMR are observed after applying external strain at 1 cm bending radius, which correspond to  $\sim 0.05$ % TMR change.

## CITED LITERATURE

1. Datta, S.; Das, B., Electronic analog of the electro-optic modulator. *Applied Physics Letters* **1990**, *56* (7), 665-667.
2. Kittel, C., *Introduction to Solid State Physics*. 8 ed.; John Wiley & Sons, Inc: 2005; p 680.
3. Baibich, M. N.; Broto, J. M.; Fert, A.; Nguyen Van Dau, F.; Petroff, F.; Etienne, P.; Creuzet, G.; Friederich, A.; Chazelas, J., Giant magnetoresistance of (001)Fe/(001)Cr magnetic superlattices. *Physical Review Letters* **1988**, *61* (21), 2472-2475.
4. Binasch, G.; Grünberg, P.; Saurenbach, F.; Zinn, W., Enhanced magnetoresistance in layered magnetic structures with antiferromagnetic interlayer exchange. *Physical Review B* **1989**, *39* (7), 4828-4830.
5. Grünberg, P. A., Nobel Lecture: From spin waves to giant magnetoresistance and beyond. *Reviews of Modern Physics* **2008**, *80* (4), 1531-1540.
6. Fert, A., Nobel Lecture: Origin, development, and future of spintronics. *Reviews of Modern Physics* **2008**, *80* (4), 1517-1530.
7. Day, C., Discoverers of giant magnetoresistance win this year's physics nobel. *Physics Today* **2007**, *60* (12), 12-14.
8. Julliere, M., Tunneling between ferromagnetic films. *Physics letters A* **1975**, *53* (3), 225-226.
9. Maekawa, S.; Gafvert, U., Electron Tunneling Between Ferromagnetic Films. *IEEE Transactions on Magnetics* **1982**, *18* (2), 707-708.
10. Moodera, J. S.; Kinder, L. R.; Wong, T. M.; Meservey, R., Large magnetoresistance at room temperature in ferromagnetic thin film tunnel junctions. *Physical Review Letters* **1995**, *74* (16), 3273-3276.
11. Miyazaki, T.; Tezuka, N., Giant magnetic tunneling effect in Fe/Al<sub>2</sub>O<sub>3</sub>/Fe junction. *Journal of Magnetism and Magnetic Materials* **1995**, *139* (3), L231-L234.

## CITED LITERATURE (continued)

175

12. Parkin, S. S. P.; Roche, K. P.; Samant, M. G.; Rice, P. M.; Beyers, R. B.; Scheuerlein, R. E.; O'Sullivan, E. J.; Brown, S. L.; Bucchigano, J.; Abraham, D. W.; Lu, Y.; Rooks, M.; Trouilloud, P. L.; Wanner, R. A.; Gallagher, W. J., Exchange-biased magnetic tunnel junctions and application to nonvolatile magnetic random access memory (invited). *Journal of Applied Physics* **1999**, *85* (8), 5828-5833.
13. Samant, M. G.; Lüning, J.; Stöhr, J.; Parkin, S. S. P., Thermal stability of IrMn and MnFe exchange-biased magnetic tunnel junctions. *Applied Physics Letters* **2000**, *76* (21), 3097-3099.
14. Yoon, K. S.; Park, J. H.; Choi, J. H.; Yang, J. Y.; Lee, C. H.; Kim, C. O.; Hong, J. P.; Kang, T. W., Performance of Co/Al<sub>2</sub>O<sub>3</sub>/NiFe magnetic tunnel junctions prepared by a two-step rf plasma oxidation method. *Applied Physics Letters* **2001**, *79* (8), 1160-1162.
15. Han, X.-F.; Oogane, M.; Kubota, H.; Ando, Y.; Miyazaki, T., Fabrication of high-magnetoresistance tunnel junctions using Co<sub>75</sub>Fe<sub>25</sub> ferromagnetic electrodes. *Applied Physics Letters* **2000**, *77* (2), 283-285.
16. Bowen, M.; Cros, V.; Petroff, F.; Fert, A.; Martínez Boubeta, C.; Costa-Krämer, J. L.; Anguita, J. V.; Cebollada, A.; Briones, F.; de Teresa, J. M.; Morellón, L.; Ibarra, M. R.; Güell, F.; Peiró, F.; Cornet, A., Large magnetoresistance in Fe/MgO/FeCo(001) epitaxial tunnel junctions on GaAs(001). *Applied Physics Letters* **2001**, *79* (11), 1655-1657.
17. Lu, Y.; Altman, R. A.; Marley, A.; Rishton, S. A.; Trouilloud, P. L.; Xiao, G.; Gallagher, W. J.; Parkin, S. S. P., Shape-anisotropy-controlled magnetoresistive response in magnetic tunnel junctions. *Applied Physics Letters* **1997**, *70* (19), 2610-2612.
18. Sousa, R. C.; Sun, J. J.; Soares, V.; Freitas, P. P.; Kling, A.; da Silva, M. F.; Soares, J. C., Large tunneling magnetoresistance enhancement by thermal anneal. *Applied Physics Letters* **1998**, *73* (22), 3288-3290.
19. Parkin, S. S. P.; Moon, K. S.; Pettit, K. E.; Smith, D. J.; Dunin-Borkowski, R. E.; McCartney, M. R., Magnetic tunnel junctions thermally stable to above 300 °C. *Applied Physics Letters* **1999**, *75* (4), 543-545.

20. Rishton, S. A.; Lu, Y.; Altman, R. A.; Marley, A. C.; Bian, X. P.; Jahnes, C.; Viswanathan, R.; Xiao, G.; Gallagher, W. J.; Parkin, S. S. P., Magnetic Tunnel Junctions fabricated at tenth-micron dimensions by electron beam lithography. *Microelectronic Engineering* **1997**, *35* (1-4), 249-252.
21. Wei, H. X.; Qin, Q. H.; Ma, M.; Sharif, R.; Han, X. F., 80% tunneling magnetoresistance at room temperature for thin Al–O barrier magnetic tunnel junction with CoFeB as free and reference layers. *Journal of Applied Physics* **2007**, *101* (9), 09B501. 1-3
22. Jiang, X.; Panchula, A. F.; Parkin, S. S. P., Magnetic tunnel junctions with ZnSe barriers. *Applied Physics Letters* **2003**, *83* (25), 5244-5246.
23. Gajek, M.; Bibes, M.; Fusil, S.; Bouzehouane, K.; Fontcuberta, J.; Barthelemy, A.; Fert, A., Tunnel junctions with multiferroic barriers. *Nature Materials* **2007**, *6* (4), 296-302.
24. Xiong, Z. H.; Wu, D.; Valy Vardeny, Z.; Shi, J., Giant magnetoresistance in organic spin-valves. *Nature* **2004**, *427* (6977), 821-824.
25. Mathon, J.; Umerski, A., Theory of tunneling magnetoresistance of an epitaxial Fe/MgO/Fe(001) junction. *Physical Review B* **2001**, *63* (22).1-4.
26. Butler, W. H.; Zhang, X. G.; Schulthess, T. C.; MacLaren, J. M., Spin-dependent tunneling conductance of Fe|MgO|Fe sandwiches. *Physical Review B* **2001**, *63* (5). 1-12.
27. Faure-Vincent, J.; Tiusan, C.; Jouguelet, E.; Canet, F.; Sajjeddine, M.; Bellouard, C.; Popova, E.; Hehn, M.; Moutaigne, F.; Schuhl, A., High tunnel magnetoresistance in epitaxial Fe/MgO/Fe tunnel junctions. *Applied Physics Letters* **2003**, *82* (25), 4507-4509.
28. Parkin, S. S.; Kaiser, C.; Panchula, A.; Rice, P. M.; Hughes, B.; Samant, M.; Yang, S. H., Giant tunnelling magnetoresistance at room temperature with MgO (100) tunnel barriers. *Nature Materials* **2004**, *3* (12), 862-867.
29. Yuasa, S.; Nagahama, T.; Fukushima, A.; Suzuki, Y.; Ando, K., Giant room-temperature magnetoresistance in single-crystal Fe/MgO/Fe magnetic tunnel junctions. *Nature Materials* **2004**, *3* (12), 868-871.

30. Yuasa, S.; Fukushima, A.; Kubota, H.; Suzuki, Y.; Ando, K., Giant tunneling magnetoresistance up to 410% at room temperature in fully epitaxial Co / MgO / Co magnetic tunnel junctions with bcc Co(001) electrodes. *Applied Physics Letters* **2006**, *89* (4), 042505. 1-3.
31. Hayakawa, J.; Ikeda, S.; Lee, Y. M.; Matsukura, F.; Ohno, H., Effect of high annealing temperature on giant tunnel magnetoresistance ratio of CoFeB / MgO / CoFeB magnetic tunnel junctions. *Applied Physics Letters* **2006**, *89* (23), 232510. 1-3.
32. Ikeda, S.; Hayakawa, J.; Ashizawa, Y.; Lee, Y. M.; Miura, K.; Hasegawa, H.; Tsunoda, M.; Matsukura, F.; Ohno, H., Tunnel magnetoresistance of 604% at 300K by suppression of Ta diffusion in CoFeB / MgO / CoFeB pseudo-spin-valves annealed at high temperature. *Applied Physics Letters* **2008**, *93* (8), 082508. 1-3.
33. Djayaprawira, D. D.; Tsunekawa, K.; Nagai, M.; Maehara, H.; Yamagata, S.; Watanabe, N.; Yuasa, S.; Suzuki, Y.; Ando, K., 230% room-temperature magnetoresistance in CoFeB / MgO / CoFeB magnetic tunnel junctions. *Applied Physics Letters* **2005**, *86* (9), 092502. 1-3.
34. Yuasa, S.; Katayama, T.; Nagahama, T.; Fukushima, A.; Kubota, H.; Suzuki, Y.; Ando, K., Giant tunneling magnetoresistance in fully epitaxial body-centered-cubic Co / MgO / Fe magnetic tunnel junctions. *Applied Physics Letters* **2005**, *87* (22), 222508. 1-3.
35. Lee, Y. M.; Hayakawa, J.; Ikeda, S.; Matsukura, F.; Ohno, H., Effect of electrode composition on the tunnel magnetoresistance of pseudo-spin-valve magnetic tunnel junction with a MgO tunnel barrier. *Applied Physics Letters* **2007**, *90* (21), 212507. 1-3.
36. Tsunoda, M.; Nishikawa, K.; Ogata, S.; Takahashi, M., 60% magnetoresistance at room temperature in Co-Fe/Al-O/Co-Fe tunnel junctions oxidized with Kr-O<sub>2</sub> plasma. *Applied Physics Letters* **2002**, *80* (17), 3135-3137.
37. Sakuraba, Y.; Hattori, M.; Oogane, M.; Ando, Y.; Kato, H.; Sakuma, A.; Miyazaki, T.; Kubota, H., Giant tunneling magnetoresistance in Co<sub>2</sub>MnSi / Al - O / Co<sub>2</sub>MnSi magnetic tunnel junctions. *Applied Physics Letters* **2006**, *88* (19), 192508. 1-3.

## CITED LITERATURE (continued)

178

38. Novoselov, K. S.; Geim, A. K.; Morozov, S. V.; Jiang, D.; Zhang, Y.; Dubonos, S. V.; Grigorieva, I. V.; Firsov, A. A., Electric field effect in atomically thin carbon films. *Science* **2004**, *306*, 666-669.
39. Geim, A. K., Nobel Lecture: Random walk to graphene. *Reviews of Modern Physics* **2011**, *83* (3), 851-862.
40. Novoselov, K. S., Nobel Lecture: Graphene: Materials in the Flatland. *Reviews of Modern Physics* **2011**, *83* (3), 837-849.
41. Guinea, F.; Katsnelson, M. I.; Geim, A. K., Energy gaps and a zero-field quantum Hall effect in graphene by strain engineering. *Nature Physics* **2009**, *6* (1), 30-33.
42. Pereira, V. M.; Castro Neto, A. H., Strain engineering of graphene's electronic structure. *Physical Review Letters* **2009**, *103* (4), 046801. 1-4.
43. Zhu, W.; Low, T.; Perebeinos, V.; Bol, A. A.; Zhu, Y.; Yan, H.; Tersoff, J.; Avouris, P., Structure and electronic transport in graphene wrinkles. *Nano Letters* **2012**, *12* (7), 3431-3436.
44. Chen, Z.; Lin, Y.-M.; Rooks, M. J.; Avouris, P., Graphene nano-ribbon electronics. *Physica E: Low-dimensional Systems and Nanostructures* **2007**, *40* (2), 228-232.
45. Wang, X.; Ouyang, Y.; Li, X.; Wang, H.; Guo, J.; Dai, H., Room-temperature all-semiconducting sub-10-nm graphene nanoribbon field-effect transistors. *Physical Review Letters* **2008**, *100* (20), 206803. 1-4.
46. Li, X.; Xinran, W.; Li, Z.; Lee, S.; Dai, H., Chemically Derived, Ultrasoft Graphene Nanoribbon Semiconductors. *Science* **2008**, *319*, 1229 - 1232.
47. Kosynkin, D. V.; Higginbotham, A. L.; Sinitskii, A.; Lomeda, J. R.; Dimiev, A.; Price, B. K.; Tour, J. M., Longitudinal unzipping of carbon nanotubes to form graphene nanoribbons. *Nature* **2009**, *458* (7240), 872-876.
48. Wang, H.; Lu, Z.; Kong, D.; Sun, J.; Hymel, T. M.; Cui, Y., Electrochemical Tuning of MoS<sub>2</sub> Nanoparticles on Three-Dimensional Substrate for Efficient Hydrogen Evolution. *ACS Nano* **2014**, *8* (5), 4940 - 4947.

49. Kappera, R.; Voiry, D.; Yalcin, S. E.; Branch, B.; Gupta, G.; Mohite, A. D.; Chhowalla, M., Phase-engineered low-resistance contacts for ultrathin MoS<sub>2</sub> transistors. *Nature Materials* **2014**, *13* (12), 1128-1134.
50. Chhowalla, M.; Shin, H. S.; Eda, G.; Li, L. J.; Loh, K. P.; Zhang, H., The chemistry of two-dimensional layered transition metal dichalcogenide nanosheets. *Nature Chemistry* **2013**, *5* (4), 263-275.
51. Cho, S.; Kim, S.; Kim, J. H.; Zhao, J.; Seok, J.; Keum, D. H.; Baik, J.; Choe, D.-H.; Chang, K. J.; Suenaga, K.; Kim, S. W.; Lee, Y. H.; Yang, H., Phase patterning for ohmic homojunction contact in MoTe<sub>2</sub>. *Science* **2015**, *349* (6248), 625-628.
52. Ma, Y.; Liu, B.; Zhang, A.; Chen, L.; Fathi, M.; Shen, C.; Abbas, A. N.; Ge, M.; Mecklenburg, M.; Zhou, C., Reversible Semiconducting-to-Metallic Phase Transition in Chemical Vapor Deposition Grown Monolayer WSe<sub>2</sub> and Applications for Devices. *ACS Nano* **2015**, *9* (7), 7383 - 7391.
53. Neto, A. H. C.; Novoselov, K., New directions in science and technology: two-dimensional crystals. *Reports on Progress in Physics* **2011**, *74* (8), 082501. 1-9.
54. Lv, R.; Robinson, J. A.; Schaak, R. E.; Sun, D.; Sun, Y.; Mallouk, T. E.; Terrones, M., Transition metal dichalcogenides and beyond: synthesis, properties, and applications of single- and few-layer nanosheets. *Accounts of Chemical Research* **2015**, *48* (1), 56-64.
55. Zhang, W.; Huang, J. K.; Chen, C. H.; Chang, Y. H.; Cheng, Y. J.; Li, L. J., High-gain phototransistors based on a CVD MoS<sub>2</sub> monolayer. *Advanced Materials* **2013**, *25* (25), 3456-3461.
56. Perea-López, N.; Lin, Z.; Pradhan, N. R.; Iñiguez-Rábago, A.; Laura Elías, A.; McCreary, A.; Lou, J.; Ajayan, P. M.; Terrones, H.; Balicas, L.; Terrones, M., CVD-grown monolayered MoS<sub>2</sub> as an effective photosensor operating at low-voltage. *2D Materials* **2014**, *1* (1), 011004.

57. Sundaram, R. S.; Engel, M.; Lombardo, A.; Krupke, R.; Ferrari, A. C.; Avouris, P.; Steiner, M., Electroluminescence in single layer MoS<sub>2</sub>. *Nano Letters* **2013**, *13* (4), 1416-1421.
58. Jo, S.; Ubrig, N.; Berger, H.; Kuzmenko, A. B.; Morpurgo, A. F., Mono- and bilayer WS<sub>2</sub> light-emitting transistors. *Nano Letters* **2014**, *14* (4), 2019-2025.
59. Cheng, R.; Li, D.; Zhou, H.; Wang, C.; Yin, A.; Jiang, S.; Liu, Y.; Chen, Y.; Huang, Y.; Duan, X., Electroluminescence and photocurrent generation from atomically sharp WSe<sub>2</sub>/MoS<sub>2</sub> heterojunction p-n diodes. *Nano Letters* **2014**, *14* (10), 5590-5597.
60. Withers, F.; Del Pozo-Zamudio, O.; Schwarz, S.; Dufferwiel, S.; Walker, P. M.; Godde, T.; Rooney, A. P.; Gholinia, A.; Woods, C. R.; Blake, P.; Haigh, S. J.; Watanabe, K.; Taniguchi, T.; Aleiner, I. L.; Geim, A. K.; Fal'ko, V. I.; Tartakovskii, A. I.; Novoselov, K. S., WSe<sub>2</sub> Light-Emitting Tunneling Transistors with Enhanced Brightness at Room Temperature. *Nano Letters* **2015**, *15* (12), 8223-8228.
61. Jeon, P. J.; Kim, J. S.; Lim, J. Y.; Cho, Y.; Pezeshki, A.; Lee, H. S.; Yu, S.; Min, S. W.; Im, S., Low Power Consumption Complementary Inverters with n-MoS<sub>2</sub> and p-WSe<sub>2</sub> Dichalcogenide Nanosheets on Glass for Logic and Light-Emitting Diode Circuits. *ACS Applied Material & Interfaces* **2015**, *7* (40), 22333-22340.
62. Yang, W.; Shang, J.; Wang, J.; Shen, X.; Cao, B.; Peimyoo, N.; Zou, C.; Chen, Y.; Wang, Y.; Cong, C.; Huang, W.; Yu, T., Electrically Tunable Valley-Light Emitting Diode (vLED) Based on CVD-Grown Monolayer WS<sub>2</sub>. *Nano Letters* **2016**, *16* (3), 1560-1567.
63. Hong, X.; Kim, J.; Shi, S. F.; Zhang, Y.; Jin, C.; Sun, Y.; Tongay, S.; Wu, J.; Zhang, Y.; Wang, F., Ultrafast charge transfer in atomically thin MoS<sub>2</sub>/WS<sub>2</sub> heterostructures. *Nature Nanotechnology* **2014**, *9* (9), 682-686.
64. Groenendijk, D. J.; Buscema, M.; Steele, G. A.; Michaelis de Vasconcellos, S.; Bratschitsch, R.; van der Zant, H. S.; Castellanos-Gomez, A., Photovoltaic and photothermoelectric effect in a double-gated WSe<sub>2</sub> device. *Nano Letters* **2014**, *14* (10), 5846-5852.

## CITED LITERATURE (continued)

181

65. Radisavljevic, B.; Radenovic, A.; Brivio, J.; Giacometti, V.; Kis, A., Single-layer MoS<sub>2</sub> transistors. *Nature Nanotechnology* **2011**, *6* (3), 147-150.
66. Bertolazzi, S.; Brivio, J.; Kis, A., Stretching and Breaking of Ultrathin MoS<sub>2</sub>. *ACS Nano* **2011**, *5* (12), 9703 - 9709.
67. Pu, J.; Yomogida, Y.; Liu, K. K.; Li, L. J.; Iwasa, Y.; Takenobu, T., Highly flexible MoS<sub>2</sub> thin-film transistors with ion gel dielectrics. *Nano Letters* **2012**, *12* (8), 4013-4017.
68. He, Q.; Zeng, Z.; Yin, Z.; Li, H.; Wu, S.; Huang, X.; Zhang, H., Fabrication of flexible MoS<sub>2</sub> thin-film transistor arrays for practical gas-sensing applications. *Small* **2012**, *8* (19), 2994-2999.
69. Das, S.; Gulotty, R.; Sumant, A. V.; Roelofs, A., All two-dimensional, flexible, transparent, and thinnest thin film transistor. *Nano Letters* **2014**, *14* (5), 2861-2866.
70. Roy, T.; Tosun, M.; Kang, J. S.; Sachid, A. B.; Desai, S. B.; Hettick, M.; Hu, C. C.; Javey, A., Field-Effect Transistors Built from All Two-Dimensional Material Components. *ACS Nano* **2014**, *8* (6), 6259 - 6264.
71. Zhu, Z. Y.; Cheng, Y. C.; Schwingenschlögl, U., Giant spin-orbit-induced spin splitting in two-dimensional transition-metal dichalcogenide semiconductors. *Physical Review B* **2011**, *84* (15).
72. Mak, K. F.; He, K.; Shan, J.; Heinz, T. F., Control of valley polarization in monolayer MoS<sub>2</sub> by optical helicity. *Nature Nanotechnology* **2012**, *7* (8), 494-498.
73. Zeng, H.; Dai, J.; Yao, W.; Xiao, D.; Cui, X., Valley polarization in MoS<sub>2</sub> monolayers by optical pumping. *Nature Nanotechnology* **2012**, *7* (8), 490-493.
74. Hill, E. W.; Geim, A. K.; Novoselov, K.; Schedin, F.; Blake, P., Graphene Spin Valve Devices. *IEEE Transactions on Magnetics* **2006**, *42* (10), 2694-2696.
75. Karpan, V. M.; Giovannetti, G.; Khomyakov, P. A.; Talanana, M.; Starikov, A. A.; Zwierzycki, M.; van den Brink, J.; Brocks, G.; Kelly, P. J., Graphite and graphene as perfect spin filters. *Physical Review Letters* **2007**, *99* (17), 176602. 1-4.

76. Mohiuddin, T. M. G.; Hill, E.; Elias, D.; Zhukov, A.; Novoselov, K.; Geim, A., Graphene in Multilayered CPP Spin Valves. *IEEE Transactions on Magnetics* **2008**, *44* (11), 2624-2627.
77. Cobas, E.; Friedman, A. L.; Van't Erve, O. M.; Robinson, J. T.; Jonker, B. T., Graphene as a tunnel barrier: graphene-based magnetic tunnel junctions. *Nano Letters* **2012**, *12* (6), 3000-3004.
78. Iqbal, M. Z.; Iqbal, M. W.; Lee, J. H.; Kim, Y. S.; Chun, S.-H.; Eom, J., Spin valve effect of NiFe/graphene/NiFe junctions. *Nano Research* **2013**, *6* (5), 373-380.
79. Chen, J. J.; Meng, J.; Zhou, Y. B.; Wu, H. C.; Bie, Y. Q.; Liao, Z. M.; Yu, D. P., Layer-by-layer assembly of vertically conducting graphene devices. *Nature Communication* **2013**, *4*, 1921.
80. Meng, J.; Chen, J. J.; Yan, Y.; Yu, D. P.; Liao, Z. M., Vertical graphene spin valve with Ohmic contacts. *Nanoscale* **2013**, *5* (19), 8894-8898.
81. Entani, S.; Naramoto, H.; Sakai, S., Magnetotransport properties of a few-layer graphene-ferromagnetic metal junctions in vertical spin valve devices. *Journal of Applied Physics* **2015**, *117* (17), 17A334. 1-4.
82. Park, J.-H.; Lee, H.-J., Out-of-plane magnetoresistance in ferromagnet/graphene/ferromagnet spin-valve junctions. *Physical Review B* **2014**, *89* (16). 165417. 1-7.
83. Li, W.; Xue, L.; Abruña, H. D.; Ralph, D. C., Magnetic tunnel junctions with single-layer-graphene tunnel barriers. *Physical Review B* **2014**, *89* (18). 184418. 1-5.
84. Cobas, E. D.; van 't Erve, O. M.; Cheng, S. F.; Culbertson, J. C.; Jernigan, G. G.; Bussman, K.; Jonker, B. T., Room-Temperature Spin Filtering in Metallic Ferromagnet-Multilayer Graphene-Ferromagnet Junctions. *ACS Nano* **2016**, *10* (11), 10357-10365.
85. Dankert, A.; Venkata Kamalakar, M.; Wajid, A.; Patel, R. S.; Dash, S. P., Tunnel magnetoresistance with atomically thin two-dimensional hexagonal boron nitride barriers. *Nano Research* **2014**, *8* (4), 1357-1364.

86. Iqbal, M. Z.; Siddique, S.; Hussain, G.; Iqbal, M. W., Room temperature spin valve effect in the NiFe/Gr-hBN/Co magnetic tunnel junction. *Journal of Materials Chemistry C* **2016**, *4* (37), 8711-8715.
87. Xu, L.; Feng, J.; Zhao, K.; Lv, W.; Han, X.; Liu, Z.; Xu, X.; Huang, H.; Zeng, Z., Magnetoresistance Effect in NiFe/BP/NiFe Vertical Spin Valve Devices. *Advances in Condensed Matter Physics* **2017**, *2017*, 1-6.
88. Yang, L.; Majumdar, K.; Liu, H.; Du, Y.; Wu, H.; Hatzistergos, M.; Hung, P. Y.; Tieckelmann, R.; Tsai, W.; Hobbs, C.; Ye, P. D., Chloride molecular doping technique on 2D materials: WS<sub>2</sub> and MoS<sub>2</sub>. *Nano Letters* **2014**, *14* (11), 6275-6280.
89. Ramasubramaniam, A.; Naveh, D., Mn-doped monolayer MoS<sub>2</sub>: An atomically thin dilute magnetic semiconductor. *Physical Review B* **2013**, *87* (19).
90. Wang, W.; Narayan, A.; Tang, L.; Dolui, K.; Liu, Y.; Yuan, X.; Jin, Y.; Wu, Y.; Rungger, I.; Sanvito, S.; Xiu, F., Spin-Valve Effect in NiFe/MoS<sub>2</sub>/NiFe Junctions. *Nano Letters* **2015**, *15* (8), 5261-5267.
91. Dankert, A.; Pashaei, P.; Kamalakar, M. V.; Gaur, A. P. S.; Sahoo, S.; Rungger, I.; Narayan, A.; Dolui, K.; Hoque, M. A.; Patel, R. S.; de Jong, M. P.; Katiyar, R. S.; Sanvito, S.; Dash, S. P., Spin-Polarized Tunneling through Chemical Vapor Deposited Multilayer Molybdenum Disulfide. *ACS Nano* **2017**, *11* (6), 6389-6395.
92. Zhao, K.; Xing, Y.; Han, J.; Feng, J.; Shi, W.; Zhang, B.; Zeng, Z., Magnetic transport property of NiFe/WSe<sub>2</sub>/NiFe spin valve structure. *Journal of Magnetism and Magnetic Materials* **2017**, *432*, 10-13.
93. Coleman, J. N.; Lotya, M.; O'Neill, A.; Bergin, S. D.; King, P. J.; Khan, U.; Young, K.; Gaucher, A.; De, S.; Smith, R. J.; Shvets, I. V.; Arora, S. K.; Stanton, G.; Kim, H.-Y.; Lee, K.; Kim, G. T.; Duesberg, G. S.; Hallam, T.; Boland, J. J.; Wang, J. J.; Donegan, J. F.; Grunlan, J. C.; Moriarty, G.; Shmeliov, A.; Nicholls, R. J.; Perkins, J. M.; Grieverson, E. M.; Theuwissen, K.; McComb, D. W.; Nellist, P. D.; Nicolosi, V., Two-Dimensional Nanosheets Produced by Liquid Exfoliation of Layered Materials. *Science* **2011**, *311*, 568 - 571.

## CITED LITERATURE (continued)

184

94. Eda, G.; Yamaguchi, H.; Voiry, D.; Fujita, T.; Chen, M.; Chhowalla, M., Photoluminescence from chemically exfoliated MoS<sub>2</sub>. *Nano Letters* **2011**, *11* (12), 5111-5116.
95. Castellanos-Gomez, A.; Barkelid, M.; Goossens, A. M.; Calado, V. E.; van der Zant, H. S.; Steele, G. A., Laser-thinning of MoS<sub>2</sub>: on demand generation of a single-layer semiconductor. *Nano Letters* **2012**, *12* (6), 3187-3192.
96. Zhan, Y.; Liu, Z.; Najmaei, S.; Ajayan, P. M.; Lou, J., Large-area vapor-phase growth and characterization of MoS<sub>2</sub> atomic layers on a SiO<sub>2</sub> substrate. *Small* **2012**, *8* (7), 966-971.
97. Wu, S.; Huang, C.; Aivazian, G.; Ross, J. S.; Cobden, D. H.; Xu, X., VaporSolid Growth of High Optical Quality MoS<sub>2</sub> Monolayers with Near-Unity Valley Polarization. *ACS Nano* **2013**, *7* (3), 2768 - 2772.
98. Lee, Y. H.; Zhang, X. Q.; Zhang, W.; Chang, M. T.; Lin, C. T.; Chang, K. D.; Yu, Y. C.; Wang, J. T.; Chang, C. S.; Li, L. J.; Lin, T. W., Synthesis of large-area MoS<sub>2</sub> atomic layers with chemical vapor deposition. *Advanced Materials* **2012**, *24* (17), 2320-2325.
99. Najmaei, S.; Liu, Z.; Zhou, W.; Zou, X.; Shi, G.; Lei, S.; Yakobson, B. I.; Idrobo, J. C.; Ajayan, P. M.; Lou, J., Vapour phase growth and grain boundary structure of molybdenum disulphide atomic layers. *Nature Materials* **2013**, *12* (8), 754-759.
100. Liu, K. K.; Zhang, W.; Lee, Y. H.; Lin, Y. C.; Chang, M. T.; Su, C. Y.; Chang, C. S.; Li, H.; Shi, Y.; Zhang, H.; Lai, C. S.; Li, L. J., Growth of large-area and highly crystalline MoS<sub>2</sub> thin layers on insulating substrates. *Nano Letters* **2012**, *12* (3), 1538-1544.
101. Yu, Y.; Li, C.; Liu, Y.; Su, L.; Zhang, Y.; Cao, L., Controlled scalable synthesis of uniform, high-quality monolayer and few-layer MoS<sub>2</sub> films. *Scientific Reports* **2013**, *3*, 1866.
102. Wang, X.; Feng, H.; Wu, Y.; Jiao, L., Controlled synthesis of highly crystalline MoS<sub>2</sub> flakes by chemical vapor deposition. *J Am Chem Soc* **2013**, *135* (14), 5304-5307.
103. Ling, X.; Lee, Y. H.; Lin, Y.; Fang, W.; Yu, L.; Dresselhaus, M. S.; Kong, J., Role of the seeding promoter in MoS<sub>2</sub> growth by chemical vapor deposition. *Nano Letters* **2014**, *14* (2), 464-472.

104. Cong, C.; Shang, J.; Wu, X.; Cao, B.; Peimyoo, N.; Qiu, C.; Sun, L.; Yu, T., Synthesis and Optical Properties of Large-Area Single-Crystalline 2D Semiconductor WS<sub>2</sub> Monolayer from Chemical Vapor Deposition. *Advanced Optical Materials* **2014**, *2* (2), 131-136.
105. Xia, J.; Huang, X.; Liu, L. Z.; Wang, M.; Wang, L.; Huang, B.; Zhu, D. D.; Li, J. J.; Gu, C. Z.; Meng, X. M., CVD synthesis of large-area, highly crystalline MoSe<sub>2</sub> atomic layers on diverse substrates and application to photodetectors. *Nanoscale* **2014**, *6* (15), 8949-8955.
106. Clark, G.; Wu, S.; Rivera, P.; Finney, J.; Nguyen, P.; Cobden, D. H.; Xu, X., Vapor-transport growth of high optical quality WSe<sub>2</sub> monolayers. *APL Materials* **2014**, *2* (10), 101101. 1-6.
107. Chen, J.; Liu, B.; Liu, Y.; Tang, W.; Nai, C. T.; Li, L.; Zheng, J.; Gao, L.; Zheng, Y.; Shin, H. S.; Jeong, H. Y.; Loh, K. P., Chemical Vapor Deposition of Large-Sized Hexagonal WSe<sub>2</sub> Crystals on Dielectric Substrates. *Advanced Materials* **2015**, *27* (42), 6722-6727.
108. Zhou, H.; Wang, C.; Shaw, J. C.; Cheng, R.; Chen, Y.; Huang, X.; Liu, Y.; Weiss, N. O.; Lin, Z.; Huang, Y.; Duan, X., Large area growth and electrical properties of p-type WSe<sub>2</sub> atomic layers. *Nano Letters* **2015**, *15* (1), 709-713.
109. Eichfeld, S. M.; Hossain, L.; Lin, Y.-C.; Piasecki, A. F.; Kupp, B.; Birdwell, A. G.; Burke, R. A.; Lu, N.; Peng, X.; Li, J.; Azcatl, A.; McDonnell, S.; Wallace, R. M.; Kim, M. J.; Mayer, T. S.; Redwing, J. M.; Robinson, J. A., Highly Scalable, Atomically Thin WSe<sub>2</sub> Grown via Metal–Organic Chemical Vapor Deposition. In *ACS Nano*, American Chemical Society (ACS): 2015; Vol. 9, pp 2080-2087.
110. Wulff, G.; Kristallogr, Z., XXV. Zur Frage der Geschwindigkeit des Wachstums und der Auflösung der Krystallflächen. *Zeitschrift für Kristallographie - Crystalline Materials* **1901**, *34* (1-6), 449 - 530.
111. Xie, Y.; Wang, Z.; Zhan, Y.; Zhang, P.; Wu, R.; Jiang, T.; Wu, S.; Wang, H.; Zhao, Y.; Nan, T.; Ma, X., Controllable growth of monolayer MoS<sub>2</sub> by chemical vapor deposition via close MoO<sub>2</sub> precursor for electrical and optical applications. *Nanotechnology* **2017**, *28* (8), 084001. 1-11.

112. Gong, Y.; Ye, G.; Lei, S.; Shi, G.; He, Y.; Lin, J.; Zhang, X.; Vajtai, R.; Pantelides, S. T.; Zhou, W.; Li, B.; Ajayan, P. M., Synthesis of Millimeter-Scale Transition Metal Dichalcogenides Single Crystals. *Advanced Functional Materials* **2016**, *26* (12), 2009-2015.
113. Kang, K.; Xie, S.; Huang, L.; Han, Y.; Huang, P. Y.; Mak, K. F.; Kim, C. J.; Muller, D.; Park, J., High-mobility three-atom-thick semiconducting films with wafer-scale homogeneity. *Nature* **2015**, *520* (7549), 656-660.
114. Li, X.; Magnuson, C. W.; Venugopal, A.; Tromp, R. M.; Hannon, J. B.; Vogel, E. M.; Colombo, L.; Ruoff, R. S., Large-area graphene single crystals grown by low-pressure chemical vapor deposition of methane on copper. *J Am Chem Soc* **2011**, *133* (9), 2816-2819.
115. Zhang, Y.; Zhang, L.; Kim, P.; Ge, M.; Li, Z.; Zhou, C., Vapor trapping growth of single-crystalline graphene flowers: synthesis, morphology, and electronic properties. *Nano Letters* **2012**, *12* (6), 2810-2816.
116. Özden, A.; Ay, F.; Sevik, C.; Perkgöz, N. K., CVD growth of monolayer MoS<sub>2</sub>: Role of growth zone configuration and precursors ratio. *Japanese Journal of Applied Physics* **2017**, *56* (6S1), 06GG05. 1-8.
117. Molina-Sánchez, A.; Wirtz, L., Phonons in single-layer and few-layer MoS<sub>2</sub> and WS<sub>2</sub>. *Physical Review B* **2011**, *84* (15). 155413. 1-8.
118. Li, H.; Zhang, Q.; Yap, C. C. R.; Tay, B. K.; Edwin, T. H. T.; Olivier, A.; Baillargeat, D., From Bulk to Monolayer MoS<sub>2</sub>: Evolution of Raman Scattering. *Advanced Functional Materials* **2012**, *22* (7), 1385-1390.
119. Windom, B. C.; Sawyer, W. G.; Hahn, D. W., A Raman Spectroscopic Study of MoS<sub>2</sub> and MoO<sub>3</sub>: Applications to Tribological Systems. *Tribology Letters* **2011**, *42* (3), 301-310.
120. Fan, J.-H.; Gao, P.; Zhang, A.-M.; Zhu, B.-R.; Zeng, H.-L.; Cui, X.-D.; He, R.; Zhang, Q.-M., Resonance Raman scattering in bulk 2H-MX<sub>2</sub> (M = Mo, W; X = S, Se) and monolayer MoS<sub>2</sub>. *Journal of Applied Physics* **2014**, *115* (5), 053527. 1-7.

121. Terrones, H.; Del Corro, E.; Feng, S.; Poumirol, J. M.; Rhodes, D.; Smirnov, D.; Pradhan, N. R.; Lin, Z.; Nguyen, M. A.; Elias, A. L.; Mallouk, T. E.; Balicas, L.; Pimenta, M. A.; Terrones, M., New first order Raman-active modes in few layered transition metal dichalcogenides. *Scientific Reports* **2014**, *4*, 4215.
122. Buscema, M.; Steele, G. A.; van der Zant, H. S. J.; Castellanos-Gomez, A., The effect of the substrate on the Raman and photoluminescence emission of single-layer MoS<sub>2</sub>. *Nano Research* **2015**, *7* (4), 561-571.
123. Gong, Y.; Liu, Z.; Lupini, A. R.; Shi, G.; Lin, J.; Najmaei, S.; Lin, Z.; Elias, A. L.; Berkdemir, A.; You, G.; Terrones, H.; Terrones, M.; Vajtai, R.; Pantelides, S. T.; Pennycook, S. J.; Lou, J.; Zhou, W.; Ajayan, P. M., Band gap engineering and layer-by-layer mapping of selenium-doped molybdenum disulfide. *Nano Letters* **2014**, *14* (2), 442-449.
124. Shaw, J. C.; Zhou, H.; Chen, Y.; Weiss, N. O.; Liu, Y.; Huang, Y.; Duan, X., Chemical vapor deposition growth of monolayer MoSe<sub>2</sub> nanosheets. *Nano Research* **2015**, *7* (4), 511-517.
125. Nam, D.; Lee, J. U.; Cheong, H., Excitation energy dependent Raman spectrum of MoSe<sub>2</sub>. *Scientific Reports* **2015**, *5*, 17113.
126. Peimyoo, N.; Shang, J.; Yang, W.; Wang, Y.; Cong, C.; Yu, T., Thermal conductivity determination of suspended mono- and bilayer WS<sub>2</sub> by Raman spectroscopy. *Nano Research* **2014**, *8* (4), 1210-1221.
127. Wang, H.; Kong, D.; Johanes, P.; Cha, J. J.; Zheng, G.; Yan, K.; Liu, N.; Cui, Y., MoSe<sub>2</sub> and WSe<sub>2</sub> nanofilms with vertically aligned molecular layers on curved and rough surfaces. *Nano Letters* **2013**, *13* (7), 3426-3433.
128. Wang, Q. H.; Kalantar-Zadeh, K.; Kis, A.; Coleman, J. N.; Strano, M. S., Electronics and optoelectronics of two-dimensional transition metal dichalcogenides. *Nature Nanotechnology* **2012**, *7* (11), 699-712.
129. Mak, K. F.; Lee, C.; Hone, J.; Shan, J.; Heinz, T. F., Atomically thin MoS<sub>2</sub>: a new direct-gap semiconductor. *Physical Review Letters* **2010**, *105* (13), 136805. 1-4.

130. Tongay, S.; Suh, J.; Ataca, C.; Fan, W.; Luce, A.; Kang, J. S.; Liu, J.; Ko, C.; Raghunathan, R.; Zhou, J.; Ogletree, F.; Li, J.; Grossman, J. C.; Wu, J., Defects activated photoluminescence in two-dimensional semiconductors: interplay between bound, charged, and free excitons. *Scientific Reports* **2013**, *3*, 2657.
131. Li, H.; Zhang, Q.; Duan, X.; Wu, X.; Fan, X.; Zhu, X.; Zhuang, X.; Hu, W.; Zhou, H.; Pan, A.; Duan, X., Lateral Growth of Composition Graded Atomic Layer  $\text{MoS}_{2(1-x)}\text{Se}_{2x}$  Nanosheets. *J Am Chem Soc* **2015**, *137* (16), 5284-5287.
132. Elias, A. L.; Perea-Lopez, N.; Castro-Beltran, A.; Berkdemir, A.; Lv, R.; Feng, S.; D., L. A.; Hayashi, T.; Kim, Y. A.; Endo, M.; Gutierrez, H. R.; Pradhan, N. R.; Balicas, L.; Mallouk, T. E.; Lopez-Urias, F.; Terrones, H.; Terrones, M., Controlled Synthesis and Transfer of Large-Area  $\text{WS}_2$  Sheets: From Single Layer to Few Layers. *ACS Nano* **2013**, *7* (6), 5235 - 5242.
133. Yan, T.; Qiao, X.; Liu, X.; Tan, P.; Zhang, X., Photoluminescence properties and exciton dynamics in monolayer  $\text{WSe}_2$ . *Applied Physics Letters* **2014**, *105* (10), 101901. 1-4.
134. Lemme, M. C.; Echtermeyer, T. J.; Baus, M.; Kurz, H., A Graphene Field-Effect Device. *IEEE Electron Device Letters* **2007**, *28* (4), 282-284.
135. Bolotin, K. I.; Sikes, K. J.; Jiang, Z.; Klima, M.; Fudenberg, G.; Hone, J.; Kim, P.; Stormer, H. L., Ultrahigh electron mobility in suspended graphene. *Solid State Communications* **2008**, *146* (9-10), 351-355.
136. Schwierz, F., Graphene transistors. *Nature Nanotechnology* **2010**, *5* (7), 487-496.
137. Baugher, B. W.; Churchill, H. O.; Yang, Y.; Jarillo-Herrero, P., Intrinsic electronic transport properties of high-quality monolayer and bilayer  $\text{MoS}_2$ . *Nano Letters* **2013**, *13* (9), 4212-4216.
138. Schmidt, H.; Wang, S.; Chu, L.; Toh, M.; Kumar, R.; Zhao, W.; Neto, A. H.; Martin, J.; Adam, S.; Ozyilmaz, B.; Eda, G., Transport properties of monolayer  $\text{MoS}_2$  grown by chemical vapor deposition. *Nano Letters* **2014**, *14* (4), 1909-1913.

139. Kim, S.; Konar, A.; Hwang, W. S.; Lee, J. H.; Lee, J.; Yang, J.; Jung, C.; Kim, H.; Yoo, J. B.; Choi, J. Y.; Jin, Y. W.; Lee, S. Y.; Jena, D.; Choi, W.; Kim, K., High-mobility and low-power thin-film transistors based on multilayer MoS<sub>2</sub> crystals. *Nature Communication* **2012**, *3*, 1011.
140. Sik Hwang, W.; Remskar, M.; Yan, R.; Kosel, T.; Kyung Park, J.; Jin Cho, B.; Haensch, W.; Xing, H.; Seabaugh, A.; Jena, D., Comparative study of chemically synthesized and exfoliated multilayer MoS<sub>2</sub> field-effect transistors. *Applied Physics Letters* **2013**, *102* (4), 043116. 1-3.
141. Das, S.; Chen, H. Y.; Penumatcha, A. V.; Appenzeller, J., High performance multilayer MoS<sub>2</sub> transistors with scandium contacts. *Nano Letters* **2013**, *13* (1), 100-105.
142. English, C. D.; Shine, G.; Dorgan, V. E.; Saraswat, K. C.; Pop, E., Improved Contacts to MoS<sub>2</sub> Transistors by Ultra-High Vacuum Metal Deposition. *Nano Letters* **2016**, *16* (6), 3824-3830.
143. Smyth, C. M.; Addou, R.; McDonnell, S.; Hinkle, C. L.; Wallace, R. M., Contact Metal–MoS<sub>2</sub> Interfacial Reactions and Potential Implications on MoS<sub>2</sub>-Based Device Performance. *The Journal of Physical Chemistry C* **2016**, *120* (27), 14719-14729.
144. McDonnell, S.; Smyth, C.; Hinkle, C. L.; Wallace, R. M., MoS<sub>2</sub>–Titanium Contact Interface Reactions. In *ACS Applied Materials & Interfaces*, American Chemical Society (ACS): 2016; Vol. 8, pp 8289-8294.
145. Najmaei, S.; Yuan, J.; Zhang, J.; Ajayan, P.; Lou, J., Synthesis and defect investigation of two-dimensional molybdenum disulfide atomic layers. *Accounts of Chemical Research* **2015**, *48* (1), 31-40.
146. Liu, D.; Guo, Y.; Fang, L.; Robertson, J., Sulfur vacancies in monolayer MoS<sub>2</sub> and its electrical contacts. *Applied Physics Letters* **2013**, *103* (18), 183113. 1-4.
147. Allain, A.; Kang, J.; Banerjee, K.; Kis, A., Electrical contacts to two-dimensional semiconductors. *Nature Materials* **2015**, *14* (12), 1195-1205.

148. Chuang, H. J.; Chamlagain, B.; Koehler, M.; Perera, M. M.; Yan, J.; Mandrus, D.; Tomanek, D.; Zhou, Z., Low-Resistance 2D/2D Ohmic Contacts: A Universal Approach to High-Performance WSe<sub>2</sub>, MoS<sub>2</sub>, and MoSe<sub>2</sub> Transistors. *Nano Letters* **2016**, *16* (3), 1896-1902.
149. Chen, C.-H.; Wu, C.-L.; Pu, J.; Chiu, M.-H.; Kumar, P.; Takenobu, T.; Li, L.-J., Hole mobility enhancement and p-doping in monolayer WSe<sub>2</sub> by gold decoration. *2D Materials* **2014**, *1* (3), 034001.1-11.
150. Ovchinnikov, D.; Allain, A.; Huang, Y.-S.; Dumcenco, D.; Kis, A., Electrical Transport Properties of Single-Layer WS<sub>2</sub>. *ACS Nano* **2014**, *8* (8), 8174 - 8181.
151. Iqbal, M. Z.; Iqbal, M. W.; Siddique, S.; Khan, M. F.; Ramay, S. M., Room temperature spin valve effect in NiFe/WS<sub>2</sub>/Co junctions. *Scientific Reports* **2016**, *6*, 21038.
152. Lee, Y. H.; Yu, L.; Wang, H.; Fang, W.; Ling, X.; Shi, Y.; Lin, C. T.; Huang, J. K.; Chang, M. T.; Chang, C. S.; Dresselhaus, M.; Palacios, T.; Li, L. J.; Kong, J., Synthesis and transfer of single-layer transition metal disulfides on diverse surfaces. *Nano Letters* **2013**, *13* (4), 1852-1857.
153. Shang, C. H.; Nowak, J.; Jansen, R.; Moodera, J. S., Temperature dependence of magnetoresistance and surface magnetization in ferromagnetic tunnel junctions. *Physical Review B* **1998**, *58* (6), R2917-R2920.
154. Zhang, S.; Levy, P. M.; Marley, A. C.; Parkin, S. S. P., Quenching of Magnetoresistance by Hot Electrons in Magnetic Tunnel Junctions. *Physical Review Letters* **1997**, *79* (19), 3744-3747.
155. Drewello, V.; Schmalhorst, J.; Thomas, A.; Reiss, G., Evidence for strong magnon contribution to the TMR temperature dependence in MgO based tunnel junctions. *Physical Review B* **2008**, *77* (1), 014440. 1-5.
156. Iqbal, M. Z.; Iqbal, M. W.; Siddique, S.; Khan, M. F.; Ramay, S. M., Room temperature spin valve effect in NiFe/WS<sub>2</sub>/Co junctions. *Scientific Reports* **2016**, *6*, 21038.

157. Parkin, S. S. P.; Kaiser, C.; Panchula, A.; Rice, P. M.; Hughes, B.; Samant, M.; Yang, S.-H., Giant tunnelling magnetoresistance at room temperature with MgO (100) tunnel barriers. *Nature Materials* **2004**, *3* (12), 862-867.
158. Asshoff, P. U.; Sambricio, J. L.; Rooney, A. P.; Slizovskiy, S.; Mishchenko, A.; Rakowski, A. M.; Hill, E. W.; Geim, A. K.; Haigh, S. J.; Fal'ko, V. I.; Vera-Marun, I. J.; Grigorieva, I. V., Magnetoresistance of vertical Co-graphene-NiFe junctions controlled by charge transfer and proximity-induced spin splitting in graphene. *2D Materials* **2017**, *4* (3), 031004. 1-10.
159. Wang, W.; Narayan, A.; Tang, L.; Dolui, K.; Liu, Y.; Yuan, X.; Jin, Y.; Wu, Y.; Rungger, I.; Sanvito, S.; Xiu, F., Spin-Valve Effect in NiFe/MoS<sub>2</sub>/NiFe Junctions. *Nano Letters* **2015**, *15* (8), 5261-5267.
160. Yuasa, S.; Nagahama, T.; Fukushima, A.; Suzuki, Y.; Ando, K., Giant room-temperature magnetoresistance in single-crystal Fe/MgO/Fe magnetic tunnel junctions. In *Nature Materials*, 2004; Vol. 3, pp 868-871.
161. Sun, Y.; Rogers, J. A., Inorganic Semiconductors for Flexible Electronics. *Advanced Materials* **2007**, *19* (15), 1897-1916.
162. Yoon, J.; Baca, A. J.; Park, S. I.; Elvikis, P.; Geddes, J. B., 3rd; Li, L.; Kim, R. H.; Xiao, J.; Wang, S.; Kim, T. H.; Motala, M. J.; Ahn, B. Y.; Duoss, E. B.; Lewis, J. A.; Nuzzo, R. G.; Ferreira, P. M.; Huang, Y.; Rockett, A.; Rogers, J. A., Ultrathin silicon solar microcells for semitransparent, mechanically flexible and microconcentrator module designs. *Nature Materials* **2008**, *7* (11), 907-915.
163. Park, S.-I.; Ahn, J.-H.; Feng, X.; Wang, S.; Huang, Y.; Rogers, J. A., Theoretical and Experimental Studies of Bending of Inorganic Electronic Materials on Plastic Substrates. *Advanced Functional Materials* **2008**, *18* (18), 2673-2684.
164. Siegel, A. C.; Phillips, S. T.; Dickey, M. D.; Lu, N.; Suo, Z.; Whitesides, G. M., Foldable Printed Circuit Boards on Paper Substrates. *Advanced Functional Materials* **2010**, *20* (1), 28-35.

165. Chen, J. Y.; Lau, Y. C.; Coey, J. M.; Li, M.; Wang, J. P., High Performance MgO-barrier Magnetic Tunnel Junctions for Flexible and Wearable Spintronic Applications. *Scientific Reports* **2017**, *7*, 42001.
166. Loong, L. M.; Lee, W.; Qiu, X.; Yang, P.; Kawai, H.; Saeys, M.; Ahn, J. H.; Yang, H., Flexible MgO Barrier Magnetic Tunnel Junctions. *Advanced Materials* **2016**, *28* (25), 4983-4990.
167. Barraud, C.; Deranlot, C.; Seneor, P.; Mattana, R.; Dlubak, B.; Fusil, S.; Bouzheouane, K.; Deneuve, D.; Petroff, F.; Fert, A., Magnetoresistance in magnetic tunnel junctions grown on flexible organic substrates. *Applied Physics Letters* **2010**, *96* (7), 072502. 1-3.
168. Bedoya-Pinto, A.; Donolato, M.; Gobbi, M.; Hueso, L. E.; Vavassori, P., Flexible spintronic devices on Kapton. *Applied Physics Letters* **2014**, *104* (6), 062412. 1-5.
169. Li, B.; Kao, C. Y.; Yoo, J. W.; Prigodin, V. N.; Epstein, A. J., Magnetoresistance in an all-organic-based spin valve. *Advanced Materials* **2011**, *23* (30), 3382-3386.
170. Sun, X.; Bedoya-Pinto, A.; Llopis, R.; Casanova, F.; Hueso, L. E., Flexible semi-transparent organic spin valve based on bathocuproine. *Applied Physics Letters* **2014**, *105* (8), 083302. 1-4.
171. Parkin, S. S. P.; Roche, K. P.; Suzuki, T., Giant Magnetoresistance in Antiferromagnetic Co/Cu Multilayers Grown on Kapton. *Japanese Journal of Applied Physics* **1992**, *31*, L1246 - L1249.
172. Chen, Y.-f.; Mei, Y.; Kaltfen, R.; Mönch, J. I.; Schumann, J.; Freudenberger, J.; Klauß, H.-J.; Schmidt, O. G., Towards Flexible Magneto-electronics: Buffer-Enhanced and Mechanically Tunable GMR of Co/Cu Multilayers on Plastic Substrates. *Advanced Materials* **2008**, *20* (17), 3224-3228.
173. Li, H.; Zhan, Q.; Liu, Y.; Liu, L.; Yang, H.; Zuo, Z.; Shang, T.; Wang, B.; Li, R. W., Stretchable Spin Valve with Stable Magnetic Field Sensitivity by Ribbon-Patterned Periodic Wrinkles. *ACS Nano* **2016**, *10* (4), 4403-4409.

## CITED LITERATURE (continued)

193

174. Guo, Q.; Xu, X. G.; Zhang, Q. Q.; Liu, Q.; Wu, Y. J.; Zhou, Z. Q.; Zhu, W. M.; Wu, Y.; Miao, J.; Jiang, Y., Strain-controlled giant magnetoresistance of a spin valve grown on a flexible substrate. *RSC Advances* **2016**, *6* (91), 88090-88095.
175. Lee, C.; Wei, X.; Kysar, J. W.; Hone, J., Measurement of the Elastic Properties and Intrinsic Strength of Monolayer Graphene. *Science* **2008**, *321*, 385 - 388.
176. Lee, G.-H.; Yu, Y.-J.; Cui, X.; Petrone, N.; Chul-Ho, L.; Choi, M. S.; Lee, D.-Y. L.; Yoo, W. J.; Watanabe, K.; Taniguchi, T.; Nuckolls, C.; Kim, P.; Hone, J., Flexible and Transparent MoS<sub>2</sub> Field-Effect Transistors on Hexagonal Boron Nitride-Graphene Heterostructures. *ACS Nano* **2013**, *7* (9), 7931 - 7936.
177. Saha, K. K.; Blom, A.; Thygesen, K. S.; Nikolić, B. K., Magnetoresistance and negative differential resistance in Ni/graphene/Ni vertical heterostructures driven by finite bias voltage: A first-principles study. *Physical Review B* **2012**, *85* (18). 184426.1-6.
178. Piquemal-Banci, M.; Galceran, R.; Caneva, S.; Martin, M. B.; Weatherup, R. S.; Kidambi, P. R.; Bouzehouane, K.; Xavier, S.; Anane, A.; Petroff, F.; Fert, A.; Robertson, J.; Hofmann, S.; Dlubak, B.; Seneor, P., Magnetic tunnel junctions with monolayer hexagonal boron nitride tunnel barriers. *Applied Physics Letters* **2016**, *108* (10), 102404.
179. Wu, H. C.; Coileain, C. O.; Abid, M.; Mauit, O.; Syrlybekov, A.; Khalid, A.; Xu, H.; Gatensby, R.; Jing Wang, J.; Liu, H.; Yang, L.; Duesberg, G. S.; Zhang, H. Z.; Abid, M.; Shvets, I. V., Spin-dependent transport properties of Fe<sub>3</sub>O<sub>4</sub>/MoS<sub>2</sub>/Fe<sub>3</sub>O<sub>4</sub> junctions. *Scientific Reports* **2015**, *5*, 15984.
180. Luo, Y. K.; Xu, J.; Zhu, T.; Wu, G.; McCormick, E. J.; Zhan, W.; Neupane, M. R.; Kawakami, R. K., Opto-Valleytronic Spin Injection in Monolayer MoS<sub>2</sub>/Few-Layer Graphene Hybrid Spin Valves. *Nano Letters* **2017**, *17* (6), 3877-3883.
181. Gong, C.; Li, L.; Li, Z.; Ji, H.; Stern, A.; Xia, Y.; Cao, T.; Bao, W.; Wang, C.; Wang, Y.; Qiu, Z. Q.; Cava, R. J.; Louie, S. G.; Xia, J.; Zhang, X., Discovery of intrinsic ferromagnetism in two-dimensional van der Waals crystals. *Nature* **2017**. 546(7657), 265-269.

182. Huang, B.; Clark, G.; Navarro-Moratalla, E.; Klein, D. R.; Cheng, R.; Seyler, K. L.; Zhong, D.; Schmidgall, E.; McGuire, M. A.; Cobden, D. H.; Yao, W.; Xiao, D.; Jarillo-Herrero, P.; Xu, X., Layer-dependent ferromagnetism in a van der Waals crystal down to the monolayer limit. *Nature* **2017**, *546* (7657), 270-273.
183. Huang, B.; Clark, G.; Klein, D. R.; MacNeill, D.; Navarro-Moratalla, E.; Seyler, K. L.; Wilson, N.; McGuire, M. A.; Cobden, D. H.; Xiao, D.; Yao, W.; Jarillo-Herrero, P.; Xu, X., Electrical control of 2D magnetism in bilayer CrI<sub>3</sub>. *Nature Nanotechnology* **2018**, *13* (7), 544-548.
184. Seyler, K. L.; Zhong, D.; Klein, D. R.; Gao, S.; Zhang, X.; Huang, B.; Navarro-Moratalla, E.; Yang, L.; Cobden, D. H.; McGuire, M. A.; Yao, W.; Xiao, D.; Jarillo-Herrero, P.; Xu, X., Ligand-field helical luminescence in a 2D ferromagnetic insulator. *Nature Physics* **2017**, *14* (3), 277-281.
185. Bonilla, M.; Kolekar, S.; Ma, Y.; Diaz, H. C.; Kalappattil, V.; Das, R.; Eggers, T.; Gutierrez, H. R.; Phan, M. H.; Batzill, M., Strong room-temperature ferromagnetism in VSe<sub>2</sub> monolayers on van der Waals substrates. *Nature Nanotechnology* **2018**, *13* (4), 289-293.
186. Klein, D. R.; MacNeill, D.; Lado, J. L.; Soriano, D.; Navarro-Moratalla, E.; Watanabe, K.; Taniguchi, T.; Manni, S.; Canfield, P.; Fernandez-Rossier, J.; Jarillo-Herrero, P., Probing magnetism in 2D van der Waals crystalline insulators via electron tunneling. *Science* **2018**, *360*, 1218 - 1222.
187. Song, T.; Cai, X.; Tu, M.; Zhang, X.; Huang, B.; Wilson, N.; Seyler, K. L.; Zhu, L.; Taniguchi, T.; Watanabe, K.; McGuire, M. A.; Cobden, D. H.; Xiao, D.; Yao, W.; Xu, X., Giant tunneling magnetoresistance in spin-filter van der Waals heterostructures. *Science* **2018**, *360*, 1214 - 1218.

## VITA

**NAME:** Bo Hsu

**EDUCATION:**

B.S., Photonics, Feng Chia University, Taichung, Taiwan 2009.

Ph.D., Electrical and Computer Engineering, University of Illinois at Chicago, Chicago, Illinois, 2018.

**TEACHING ASSISTANTSHIPS:**

University of Illinois at Chicago

PHY 118 Introduction to Physics II Laboratory

ECE 115 Introduction to Electrical and Computer Engineering

ECE 210 Electrical Circuit Analysis

ECE 225 Circuit Analysis

ECE 310 Discrete and Continuous Signals

ECE 340 Electronics I

ECE 342 Electronics II

ECE 423 Electromagnetic Compatibility

ECE 440 Nanoelectronics

ECE 448 Transistors

ECE 520 Electromagnetics Theory

ECE 541 Microelectronic Fabrication Techniques

**PROFESSIONAL MEMBERSHIP:**

Student member of Material Research Society

Student member of American Physics Society

**PUBLICATIONS:**

1. Z. Tian, B. Xu, B. Hsu, L. Stan, Z. Yang, Y. Mei. (2018) “*Reconfigurable Vanadium Dioxide Nanomembranes and Microtubes with Controllable Phase Transition Temperatures.*” Nano letters 18(5):3017-23. (2017 Impact Factor: 12.08 )

2. A. Das, B. Hsu, A. Shamirian, Z. Yang and P. T. Snee (2017). "*Synthesis of High-Quality AgSbSe<sub>2</sub> and AgBiSe<sub>2</sub> Nanocrystals with Antimony and Bismuth Silylamide Reagents.*" Chemistry of Materials 29(10): 4597-4602. (2017 Impact Factor: 9.89)
3. Z. Chen, Y. Wang, Y. Shi, B. Hsu, Z. Yang and J. Shi (2016). "*Regulating Carrier Dynamics in Single Crystal Halide Perovskite via Interface Engineering and Optical Doping.*" Advanced Electronic Materials 2(10): 1600248. . (2017 Impact Factor: 5.466)
4. W. Zhang, J. Sklenar, B. Hsu, W. Jiang, M. B. Jungfleisch, J. Xiao, F. Y. Fradin, Y. Liu, J. E. Pearson, J. B. Ketterson, Z. Yang and A. Hoffmann (2016). "Research Update: Spin transfer torques in permalloy on monolayer MoS<sub>2</sub>." APL Materials 4(3): 032302. (2017 Impact Factor: 4.127)

#### CONFERENCE PRESENTATIONS

1. B. Hsu and Z. Yang. *Flexible Spin Valve with Monolayer 2D Material (Oral)*. **MRS 2018 Spring Meeting**, Phoenix, Arizona, USA. (April 2 – April 6, 2018)
2. B. Hsu, S. Ghosh, and Z. Yang. *Gated Transistor with a Phase Change Material(Oral)*. **MRS 2018 Spring Meeting**, Phoenix, Arizona, USA. (April 2 – April 6, 2018)
3. B. Hsu, S. Ghosh, G. Gebre, and Z. Yang. *Vanadium Dioxide Nanowire Crossbar (poster)*. **MRS 2017 Spring Meeting**, Phoenix, Arizona, USA. (April 17 – April 21, 2017)
4. B. Hsu and Z. Yang, *Two-dimensional transition metal dichalcogenides based magnetic tunneling junctions (poster)*, **MRS 2016 Fall Meeting**, Boston, Massachusetts, USA (November 28 - December 2, 2016).

5. B. Hsu, S. Ghosh, and Z. Yang, *Contact resistance study of metals on vanadium dioxide materials (poster)*, **MRS 2016 Fall Meeting**, Boston, Massachusetts, USA (November 28 - December 2, 2016).
6. A. F. Hoffmann, W. Zhang, J. Sklenar, M. B. Jungfleisch, W. Jiang, B. Hsu, J. Xiao, J. E. Pearson, F. Y. Fradin, Y. Liu, J. B. Ketterson, Z. Yang, *Driving magnetization dynamics with interfacial spin-orbit torques (oral)*, **Spintronics IX**, San Diego, California, USA (August 28 - September 1, 2016)
7. B. Hsu, and Z. Yang, *Effect of the sample mounting geometry on the grain size of single-crystalline transition-metal dichalcogenide monolayers grown by chemical vapor deposition (poster)*, **APS 2016 March Meeting**, Baltimore, Maryland, USA (March 14-18, 2016)
8. B. Hsu, N. Sultan, and Z. Yang, *Contact resistance of metals on vanadium dioxide materials (oral)*, **MRS 2015 Fall Meeting**, Boston, Massachusetts, USA (November 29 - December 4, 2015).
9. B. Hsu, G. Poulos, and Z. Yang, *Local pressure effect on the grain size of single-crystalline transition-metal dichalcogenide monolayers grown by chemical vapor deposition (poster)*, **MRS 2015 Fall Meeting**, Boston, Massachusetts, USA (November 29-December 4, 2015).
10. B. Hsu, J. Xiao, J. Banks, G. Poulos, and Z. Yang, *Vapor-trapping enhanced chemical vapor deposition large-area growth of high-quality single-crystalline transition-metal dichalcogenide monolayers (oral)*, **MRS 2015 Spring Meeting**, San Francisco, California, USA (April 6-10, 2015).
11. B. Hsu, J. Xiao, G. Poulos, and Z. Yang, *Growth, transfer, structural, optical, and electrical properties of large-size transition-metal dichalcogenide monolayer single-crystals (oral)*, **APS 2015 March Meeting**, San Antonio, Texas, USA (March 2-6, 2015).

12. *B. Hsu, J. Xiao, and Z. Yang, (Invited Talk) Chemical vapor deposition of single-crystalline molybdenum disulfide (oral),* **Energy Materials Nanotechnology Summer Meeting**, Cancun, Mexico (June 9-12, 2014).